THE DEVELOPMENT OF Cu-BASED SHAPE MEMORY ALLOYS MICROALLOYED WITH SILVER

Liverić, Lovro

UNIVERSITY OF RIJEKA
FACULTY OF ENGINEERING

Lovro Liverić

THE DEVELOPMENT OF CU-BASED SHAPE MEMORY ALLOYS MICROALLOYED WITH SILVER

DOCTORAL THESIS

Rijeka, 2023.

UNIVERSITY OF RIJEKA
FACULTY OF ENGINEERING

Lovro Liverić

THE DEVELOPMENT OF CU-BASED SHAPE MEMORY ALLOYS MICROALLOYED WITH SILVER

DOCTORAL THESIS

Supervisor: Prof. D. Sc. Tamara Holjevac Grgurić
Co-supervisor: Assoc. Prof. D. Sc. Sunčana Smokvina Hanza
Co-supervisor: Assoc. Prof. D. Sc. Wojciech Sitek

Rijeka, 2023.

SVEUČILIŠTE U RIJECI
TEHNIČKI FAKULTET

Lovro Liverić

RAZVOJ LEGURA S EFEKTOM PRISJETLJIVOSTI OBLIKA NA BAZI BAKRA MIKROLEGIRANIH SREBROM

DOKTORSKI RAD

Mentor: Prof. dr. sc. Tamara Holjevac Grgurić
Komentor: Izv. prof. dr. sc. Sunčana Smokvina Hanza
Komentor: Izv. prof. dr. sc. Wojciech Sitek

Rijeka, 2023.

Doctoral dissertation Supervisor: Prof. D. Sc. Tamara Holjevac Grgurić, School of Medicine, Catholic University of Croatia, Zagreb, Croatia,
Co-supervisor: Assoc. Prof. D. Sc. Sunčana Smokvina Hanza, University of Rijeka, Faculty of Engineering, Croatia, and,
Co-supervisor: Assoc. Prof. D. Sc. Wojciech Sitek, Silesian University of Technology, Faculty of Mechanical Engineering, Poland.

The doctoral dissertation was defended on _____ at the University of Rijeka, Faculty of Engineering, Croatia, in front of the following Evaluation Committee:

1. Assoc. Prof. D. Sc. Dario Iljkić, University of Rijeka, Faculty of Engineering, Croatia - Committee Chair
2. Assist. Prof. D. Sc. Matej Fonović, University of Rijeka, Faculty of Engineering, Croatia
3. Prof. D. Sc. Emi Govorčin Bajsić, University of Zagreb, Faculty of Chemical Engineering and Technology, Croatia

With profound gratitude, I dedicate this thesis to my inner circle: my mother Maja; my brother Luka; and my sisters, Angela and Nika.

Your presence has been my guiding light throughout this journey.

ACKNOWLEDGMENTS

I wish to offer my profound gratitude to my doctoral dissertation supervisor, Prof. D. Sc. Tamara Holjevac Grgurić. Her faith in me and her unwavering guidance and support have been instrumental throughout my doctoral work. The successful completion of this dissertation is, in large part, due to the invaluable mentorship provided by Prof. D. Sc. Tamara Holjevac Grgurić.

My sincere appreciation goes out to my co-supervisors, Assoc. Prof. Sunčana Smokvina Hanza and Assoc. Prof. D. Sc. Wojciech Sitek. Their direction steered me through the challenges of doctoral research, ensuring I remained on the right course.

I also extend my thanks to the evaluation committee members, Assoc. Prof. D. Sc. Dario Iljkić, Assist. Prof. D. Sc. Matej Fonović, and Prof. D. Sc. Emi Govorčin Bajsić. Their invaluable insights and suggestions significantly enhanced the quality of this dissertation.

I'm deeply thankful to the various research groups across different institutions and countries. Their collective expertise, willingness to share resources, and provision of essential equipment were crucial to my work.

A special thank you to Assist. Prof. D. Sc. Vedrana Špada and her team (Ener Špada, MSc. Josipa Bilić, and MSc. Ivan Pentek) from the Center Metris, Istrian University of Applied Sciences for their collaboration.

I am indebted to my friend, Assist. Prof. D. Sc. Marko Kršulja from Juraj Dobrila University of Pula, Department of Engineering, for his invaluable help with materials essential for my samples.

Thanks also to Assoc. Prof. D. Sc. Vilko Mandić and his team (Dr. Ivana Panžić and MSc. Arijeta Bafti) for their cooperation, and to Prof. D. Sc. Emi Govorčin Bajsić

and her team (MSc. Mario Meheš) for their collaboration at the Faculty of Chemical Engineering and Technology, University of Zagreb.

My co-supervisor and dear friend, Assoc. Prof. D. Sc. Wojciech Sitek, enriched my life immeasurably during my near year-long stay in Gliwice. Through him, I gained profound knowledge, made lasting friendships, and acquired extensive experience in optical and electron microscopy. I must offer a special mention to Dr. Przemysław Snopiński, a close friend who significantly influenced my passion for metallography and crystallography. His steadfast support, both academic and personal, was pivotal during my doctoral journey. My gratitude also goes to Assoc. Prof. D. Sc. Marcin Adamiak, Dr. Mariusz Król, Dr. Wojciech Borek, MSc. Krzysztof Matus, Dr. Oktawian Bialas, Dr. Paweł Nuckowski, and all the incredible people at the Faculty of Engineering at Silesian University of Technology.

I wholeheartedly thank Assoc. Prof. D. Sc. Łukasz Hawełek and his team (MSc. Tymon Warski) for their support and collaboration at the Łukasiewicz Research Network - Institute of Non-Ferrous Metals. Their guidance led me to the research group at the Institute of Metallurgy and Materials Science, Polish Academy of Sciences in Krakow. My gratitude extends to Dr. Anna Wójcik, Dr. Robert Chulist, and Assoc. Prof. D. Sc. Wojciech Maziarz for their valuable time and guidance.

Last but not least, I would like to thank my dear colleagues from the Department of Materials Engineering, my family and friends who have shown me unwavering love, support and understanding throughout this challenging journey.

To everyone mentioned and all who have contributed to my academic journey, either directly or indirectly, I extend my heartfelt gratitude.

Author

ABSTRACT

In the thesis, the influence of silver addition on martensite formation, phase transformation temperatures, and functional properties of Cu-based shape memory alloys is investigated. Microstructural analysis of quaternary Cu-Al-Mn-Ag and ternary Cu-Al-Ag SMA alloys was carried out by optical microscopy (OM), scanning electron microscopy with energy dispersive X-ray spectroscopy (SEM-EDS) and transmission electron microscopy (TEM). Phase identification was further confirmed by X-ray diffraction analysis and high-energy synchrotron (XRD). Martensitic transformation temperatures and fusion enthalpies were observed by modular differential scanning calorimetry (MDSC), while microhardness was determined by Vickers test. The results show that silver additions significantly influenced formations of the martensite structure, even in the as-cast state and especially after heat treatment and quenching in both investigated systems. Cu-9Al-16Mn-2Ag and Cu-9Al-7Mn with 2 and 5% wt. of silver showed the best functional properties, forming two types of martensite structures β_1' (18R) and γ_1' (2H). Optimal compositions of Cu-Al-Ag ternary SMA alloys forming best functional properties were found in alloys with 5 and 7% wt. of silver, with one type of martensitic structure β_1' (18R) identified.

Keywords: *Shape memory alloys, Cu-Al-Ag alloys, Cu-Al-Mn-Ag alloys, Heat treatment, Microstructure, Phase transformations, Martensitic transformation.*

PROŠIRENI SAŽETAK

Legure s efektom prisjetljivosti oblika (SMA) su pametni funkcionalni materijali koji posjeduju dva jedinstvena efekta, efekt prisjetljivosti i pseudoelastičnosti te pokazuju sposobnost povrata definiranog oblika djelovanjem temperature ili mehaničkog naprezanja. Komercijalno najkorištenija, ali istovremeno i najskuplja legura, je nitinol (Ni-Ti). U posljednje vrijeme nitinol se sve više zamjenjuje legurama na bazi bakra, koje imaju odlična funkcionalna i električna svojstava, jednostavniju proizvodnju i nižu cijenu koštanja. Od legura na bazi bakra najviše se koriste Cu-Al-Ni i Cu-Zn-Al SMA legure, koje su istraživane dugi niz godina, no pokazale su ograničenje u primjeni s obzirom na vrlo visoku krtost i lošija mehanička svojstva.

Dodavanjem mangana binarnoj Cu-Al leguri, poboljšava se duktilnost i sposobnost hladne obradivosti materijala jer mangan proširuje područje β-faze u nižim udjelima aluminija. Dizajniranjem sastava ternarnih legura s prisjetljivošću oblika te mikrolegiranjem četvrtom komponentom, moguće je znatno promijeniti svojstva legura te korigirati temperature transformacija i prilagoditi ih specifičnom području primjene.

Rezultati doktorskog istraživanja pokazuju da dodatak srebra značajno utječu na formiranje martenzitne strukture, čak i u lijevanom stanju, a posebno se intenzivni martenzit formira nakon toplinske obrade i kaljenja u oba istraživana sustava. Kod četverokomponentnih sustava, sastavi Cu-9Al-7Mn s 2 i 5% mas. Ag te Cu-9Al-16Mn-2Ag pokazali su najbolja funkcionalna svojstva materijala. U svim istraživanim sustavima javlja se samo jedan tip martenzita, β_1' (18R), izuzev u sustavima s 16% mas. Mn i 2% mas. Ag, gdje su utvrđene dvije različite metastabilne martenzitne strukture, β_1' (18R) i γ_1' (2H). Dodavanjem srebra, temperature početka martenzitne transformacije, M_s, pomiču se prema višim vrijednostima, uz istovremeno proširenje područja formiranja martenzita veće entalpije te niže temperature završetka transformacije, M_f. Toplinska obrada dodatno povisuje temperaturu M_s.

Legure koje u sastavu sadrže 10% mas. Mn i različite udjele srebra, u mikrostrukturnim analizama nisu pokazale prisutnost martenzita, što može ukazivati na vrlo niske temperature početka martenzitne transformacije, znatno niže od sobne temperature. Cu-Al-Mn-Ag legure nakon kaljenja pokazuju nižu mikrotvrdoću, što je tipično za SMA sustave. Legura s 16% mas. Mn pokazuje povećanje mikrotvrdoće nakon toplinske obrade, što može biti posljedica

prisustva krte γ_1' (2H) faze u mikrostrukturi ove legure. Kod ternarnih sustava, najintenzivniji martenzit i najbolja svojstva pokazale su legure s 5 i 7% mas. Ag.

Ključne riječi: *Legure s efektom prisjetljivosti oblika, Cu-Al-Ag legure, Cu-Al-Mn-Ag legure, Toplinska obrada, Mikrostruktura, Fazne transformacije, Martenzitna transformacija.*

CONTENTS:

1. INTRODUCTION

1.1. Research motivation

Shape Memory Alloys (SMA) are smart functional materials with exceptional properties of shape memory effect and pseudoelasticity, which have a broad area of applications including bioengineering, electronics, robotics, space, transportation, etc. [1, 2]. In particular, nitinol (Ni-Ti) alloy, one of the most commercially popular SMA applied, has attracted considerable attention in biomedical applications due to its excellent biocompatibility and mechanical properties [3]. However, rising cost and complex production of nitinol, have drawn researchers' focus to copper-based SMA (Cu-SMA), which offer them better functional properties, in non-medical applications, at lower cost and better processability [4].

SMA alloys can undergo diffusionless thermoelastic martensitic transformation that determines their shape memory properties [5-7]. Recent studies have elucidated the role of alloying elements in influencing the properties of Cu based SMA. The addition of manganese the Cu-Al alloy not only extends the β-phase range, but also increases the stability against diffusional decomposition, makes the alloy more ductile and improves its cold workability [1, 5, 6, 8]. The phase transformations that take place in these alloys during cooling are complex, with various superlattice structures such as Fe_3Al type (DO_3), CsCl type (B2) and Cu_2MnAl type ($L2_1$) [9-14]. Furthermore, the study of microalloying elements has shown how elements can influence, the grain size, mechanical properties and shape memory effect, such elements as Fe, Ti, Cr, Zn, Ni, Si, etc. [9-15].

There are few studies on the influence of silver additions to Cu-Al-Mn alloys. Preliminary studies indicate that silver can improve the functional properties of Cu-Al-Mn alloys as well as phase transformations temperatures [15-17]. Therefore, the present work aims to investigate the influence of silver on the development of martensitic structure, phase transformation temperatures, and functional properties of Cu-Al-X (X=Mn-Ag, Ag) alloys.

This investigation will not only contribute to our fundamental understanding of investigated SMA alloys and their potential modifications, but also provide insights into their applicability in various industries and offer a roadmap for future research and technological innovation. This research aims to better understanding relationship between composition of

microalloying components, microstructure, and final properties of Cu-Al-X (X=Mn-Ag, Ag) SMA alloys. An important aspect of the research is understanding the role of silver and manganese in the formation of the martensitic structure. The research investigates how different contents of silver and manganese can influence SMA alloy's microstructure, properties, phase transition temperatures and hardness. Based on the findings from the study, an attempt will finally be made to determine the best composition and processing conditions for Cu-SMA alloys. The aim is to optimize these alloys to obtain better functional properties and make them more suitable for broad applications.

1.2. Hypotheses and Contributions

The hypothesis involves designing of the composition, microstructure and functional properties of Cu-based shape memory alloys, in particular Cu-Al-X (X=Mn-Ag, Ag). The study will investigate the effect of silver addition on martensite formation and phase transformation temperatures. The processing and heat treatment parameters will be optimized to improve the properties of Cu- SMA alloys.

The research hypotheses are as follows:

1. The addition of silver to Cu-based shape memory alloys impact and influence formation of a martensitic structure and a shape memory effect of the as-cast and heat-treated alloys.
2. A higher silver content in SMA alloys shifts the start martensite temperature, $M_{S,}$ towards higher values.
3. Cu-SMA alloys with improved functional and shape memory properties can be designed by optimizations of manganese and silver composition.

The scientific contributions are as follows:

- Designing and development of innovative Cu-Al-Mn-Ag shape memory alloys.
- New knowledge about the impact of the heat treatment process on the Cu-Al-X (X=Mn-Ag, Ag) SMA alloys microstructure.
- Understanding the impact of silver microalloying on the formation of different metastable martensite structures in the both, the as-cast and quenched states of the investigated systems.
- New knowledge about the influence of manganese and silver composition on phase transformation temperatures.
- New knowledge about the mechanism of martensitic formation.
- New knowledge about the correlation between process parameters, microstructure, phase transformation temperatures and functional properties of Cu-Al-X (X=Mn-Ag, Ag) SMA alloys.

1.3. Research Methodology and Structure of the Doctoral Dissertation

The thesis is systematically structured to provide an insight in the influence of the silver addition to Cu-based SMA alloys.

In the chapter one, the Introduction provides a basic understanding of shape memory materials (SMM) and highlights the motivations for the research and its broader implications.

In the chapter two, the Literature Review systematically describes State-of-the-Art in the area of SMM materials. Basics of the shape memory effect and pseudoelasticity are explained, followed by reviews of the different types of SMM materials. Special emphasis is given to SMA alloys, with crystallographic description of stable and metastable lattice structures, martensitic transformation temperatures, and magnetic properties of SMA materials. Further, the focus shifts to copper-based SMA alloys, examining its ternary systems and the effects of microalloying. At the last part of the chapter, other shape memory materials such as polymers, ceramics, hybrids, gels, and composites are described. It concludes with an insightful

discussion of the commercial application and perspectives of SMA alloys. Thermodynamic modeling and concept of CALPHAD method is given at the end of the chapter.

In the chapter three, the Experimental Part describes used materials and characterization methods from the material selection to the complicated processing techniques of the Cu-based SMA alloys, every detail is meticulously documented. The various characterization methods are then explained, ranging from thermodynamic modelling of investigated system, microstructural analysis by optical microscopy, scanning electron microscopy, X-ray diffraction analysis and transmission electron microscopy. Further, parameters of thermal analysis and microhardness tests are presented. Chapter four, the Results and Discussion. It reveals the results of the experimental analysis of all investigated samples, quaternary Cu-Al-Mn-Ag and ternary Cu-Al-Ag SMA systems. Through a variety of characterization techniques, the microstructures, crystallography, thermal properties and material hardness are comprehensively analyzed and discussed.

The report culminates in chapter five, the Conclusions and Recommendations, which summarizes the essence of the research, highlights the main results, and possible future directions for this field.

2. LITERATURE REVIEW

This chapter begins with explanations of the shape memory effect and pseudoelasticity. These concepts set the background for a state-of-the-art overview of shape memory materials (SMM), with a focus on Cu-based shape memory alloys (SMA). It then examines the crystallography of SMA alloys to reveal the underlying structures responsible for their unique behavior. This is followed by an exploration of the crucial martensitic transformation that determines the behavior of these alloys. In this section, the ternary systems Cu-Al-X (X=Mn, Ag) are studied in detail. This is followed by a study of the microalloying of these ternary systems and finally a section detailing the effects and consequences of Ag addition in the Cu-Al-Mn system.

2.1. Shape memory effect and Pseudoelasticity (SE)

For a thermoelastic martensitic transformation to occur, it's essential for self-accommodated variants to form through twinning, without any plastic deformation caused by dislocation slip. Under mechanical stress, these variants reorient by detwinning, resulting in favored variants. This back-and-forth phase change between austenite and martensite underpins SME and SE [18-21].

- Definition of SME, is a form of thermomechanical behavior in SMA. It refers to the phenomenon of shape recovery in these alloys, which can be achieved through a specific process such as thermal or thermomechanical processing, also known as "training" or programming of the alloy. The most commonly used method for programming is deformation at elevated temperatures above the A_f temperature, followed by cooling to room temperature while the alloy is under constant stress [19, 21].

- Definition of SE, is when the application of a thermomechanical load forms the martensite phase from the austenite phase at a constant temperature. This process is accompanied by significant inelastic deformation, but this deformation disappears after unloading through the martensitic-austenitic transformation (shown on Figure 4.) [22, 23].

In the thermoelastic transformation, four temperatures stand out: M_s marks the onset of austenite's conversion to martensite, while M_f signals the culmination of this process when

austenite has fully transformed into martensite. Conversely, As indicates the beginning of the reverse transformation from martensite back to austenite, with A_f being its conclusion. In the temperature span between these starting and ending points, both phases coexist. There's a noticeable hysteresis between the initial points of direct and reverse transformations ($|M_s\text{-}A_f|$ or $|A_s\text{-}M_f|$), and between the temperature intervals initiating and concluding each transformation ($A_f\text{-}A_s$ or $M_s\text{-}M_f$) [5, 24].

When an SMA microstructure laden with twinned martensite undergoes stress, the variants reorient themselves, leading to partial detwinning and a significant morphological change in the material, persisting post unloading. This deformation stems from the variant's direction shift, maintained after stress removal, as depicted in Figure 1. [5].

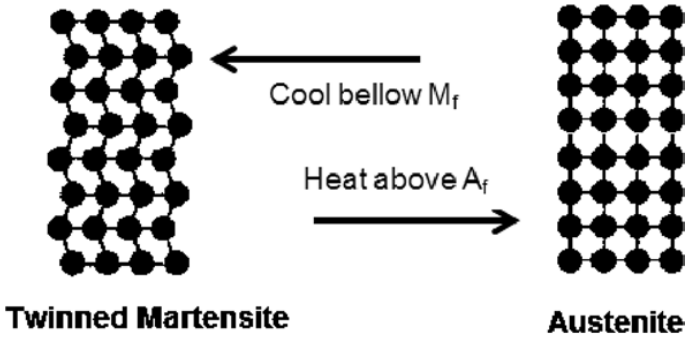

Figure 1. *Direct and reverse transformations along with their concluding transformation temperatures [5]*

Heating the metal beyond A_f facilitates the original shape's retrieval through the conversion of martensite back to austenite. Cooling from the austenitic phase under stress greater than σ_s yields already detwinned martensite, inducing a shape shift accompanying the phase change. Transformation temperatures are significantly influenced by the stress exerted on the material, with increased stresses pushing the transformation temperatures upwards [19, 22, 23, 25]. Figure 2. illustrates the detwinning process, where the minimum stress required to initiate the process is called σ_s, and the stress at which it is completed is called σ_f [5].

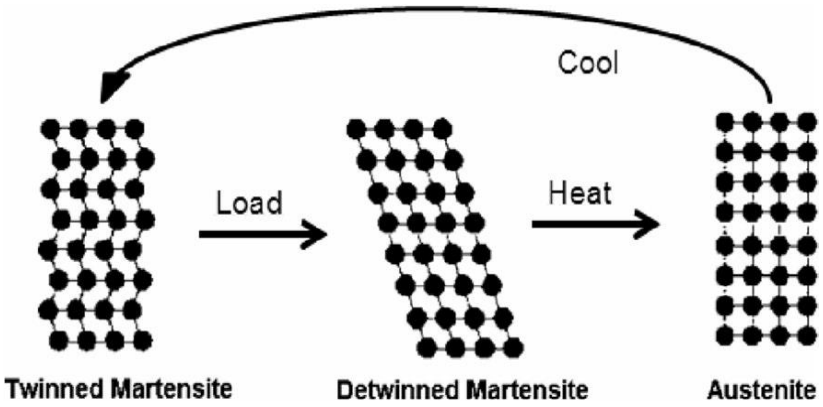

Figure 2. *SME cycle [5]*

In SMAs, SE takes place when stress-induced martensitic transformation transpires within the material's austenitic domain, leading to deformation that's reversible upon removal of external load. To achieve this, one begins with the austenitic phase at temperatures surpassing A_f, applies stress to detwin the martensite, and subsequently lets the martensite revert to the austenitic phase once stress is released. It's noteworthy that applied stress can elevate the transformation temperatures for the martensitic phase. Figure 3. depicts the interrelation between stress, strain, and temperature for SME and SE in SMAs, also highlighting the pivotal stresses needed for plastic deformation through dislocation slip [5, 19, 22, 23, 26]. Furthermore, SMAs can exhibit two distinct forms of SME, often referred to as one-way shape memory effect (OWSME) and two-way shape memory effect (TWSME).

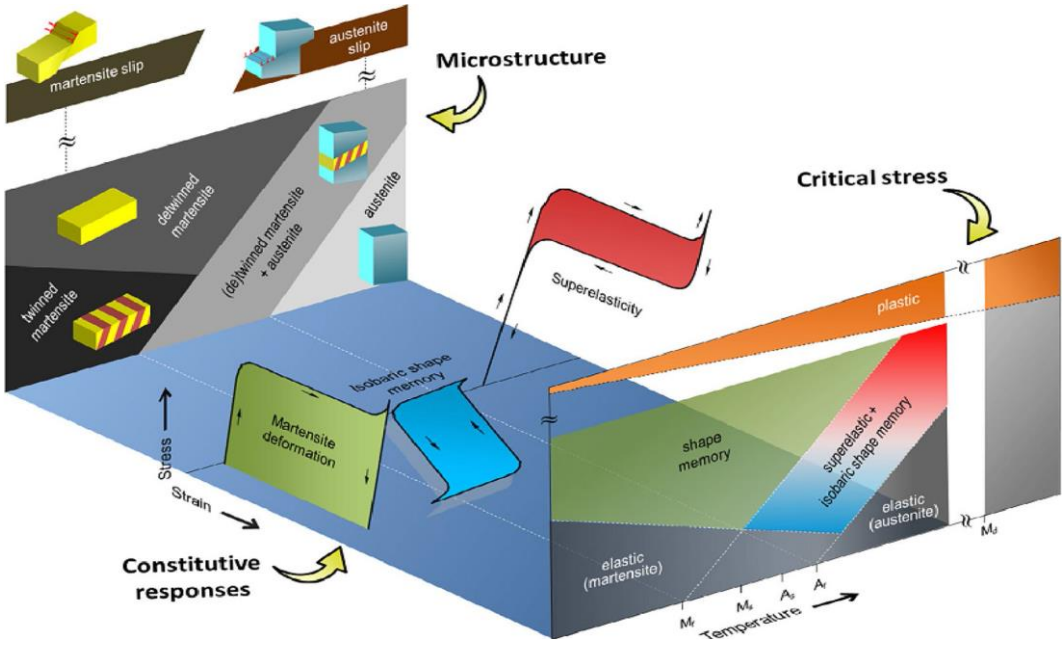

Figure 3. *The relationship between stress, strain, and temperature for SMA in both austenitic and martensitic stages. These interactions are illustrated in the stress-temperature maps [5, 27]*

In Figure 4., the sample's form stays unchanged when cooled from temperatures above A_f to those beneath M_f. Yet, if deformation occurs below M_f, the sample maintains this altered shape until heated. Recovery of its original shape begins at the A_s temperature and concludes at A_f. Once the shape reverts at A_f, cooling the specimen below M_f doesn't alter its form. To reengage the shape memory property, one would have to deform the martensitic sample anew. This particular SME process is known as the OWSME [28].

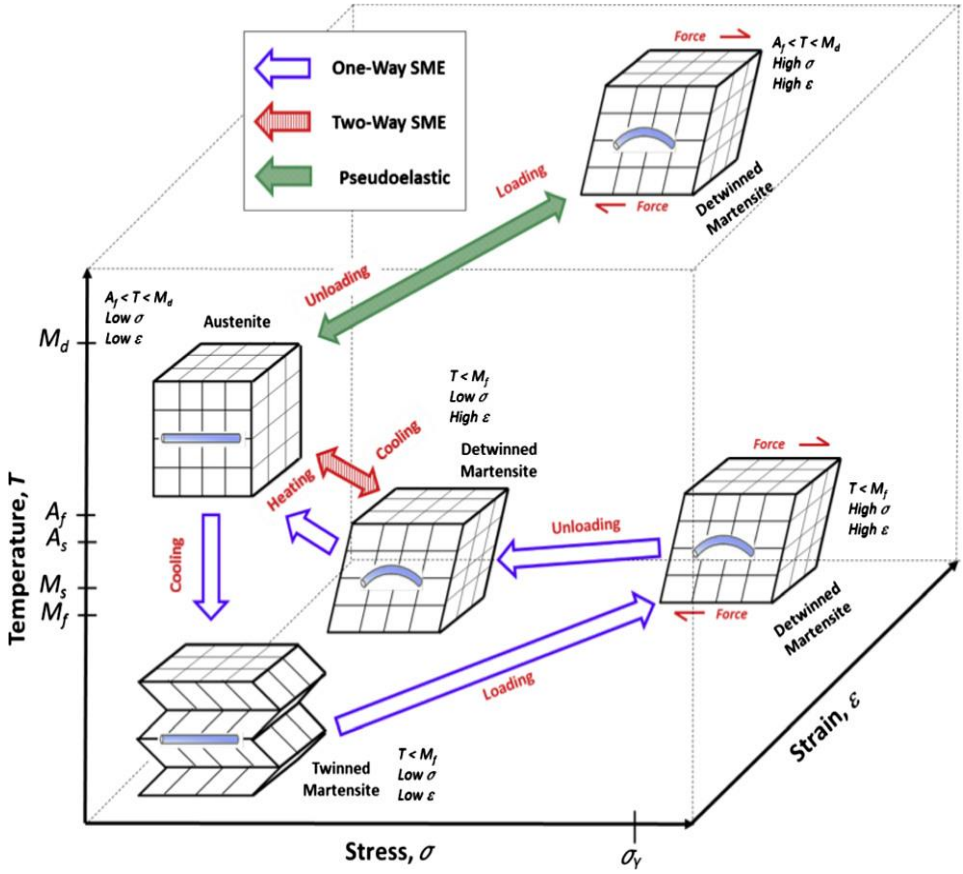

Figure 4. *One-way and Two-way SME [23, 29]*

The SME process described above preserves only the austenitic phase's form. Yet, under specific conditions, it's feasible for the shape of the martensitic phase to also be remembered. This phenomenon is termed TWSME, a trait frequently observed in SMA. Contrasting with the intrinsic nature of OWSME in SMA, TWSME manifests through specialized thermal and mechanical treatments, termed as training procedures, and is illustrated in Figure 4. Under TWSME, the substance spontaneously shifts its shape during both heating and cooling phases. Once trained, the material alternates between two distinct forms reversibly, sans the requirement of stress or load, by merely modulating the temperature across A_f and M_f [28].

The TWSME can be characterized by severe deformation in the martensitic phase. This induces dislocations that fortify the arrangement. These dislocations persist, even in the primary phase, following the martensite's reverse transformation upon heating. Throughout the training, the material acclimates to a favored microstructure conducive to TWSME [28].

2.2. Shape memory materials (SMM)

Stimulus-responsive materials are materials that respond to a specific stimulus and exhibit an observable change in their properties as a result of the stimulus. Examples of stimuli include heat, chemicals, and light. These materials are considered "smart" because of their ability to respond to changes in their environment. One type of stimulus-responsive material is the stimulus-responsive shape memory material (SMM), which has the ability to restore its original shape after being deformed quasi-plastically. The unique properties of SMMs make them an ideal and innovative solution for use in intelligent systems, as they are capable of generating active or reactive movements in response to specific stimuli, which can trigger mechanisms or machines.

Materials that react to heat are termed thermo-responsive, while those sensitive to stress or pressure are dubbed mechano-responsive. Those that respond to electric currents or voltages are labeled electro-responsive, and materials influenced by magnetic fields are identified as magneto-responsive. Materials reacting to alterations in pH, dissolution, or humidity are denoted as chemo-responsive. Lastly, those that change due to light exposure are termed photo-responsive.

The various types of stimulus-responsive materials can be grouped and recognized based on the type of stimulus to which they respond [25]. Figure 5. provides a visual representation of these groups.

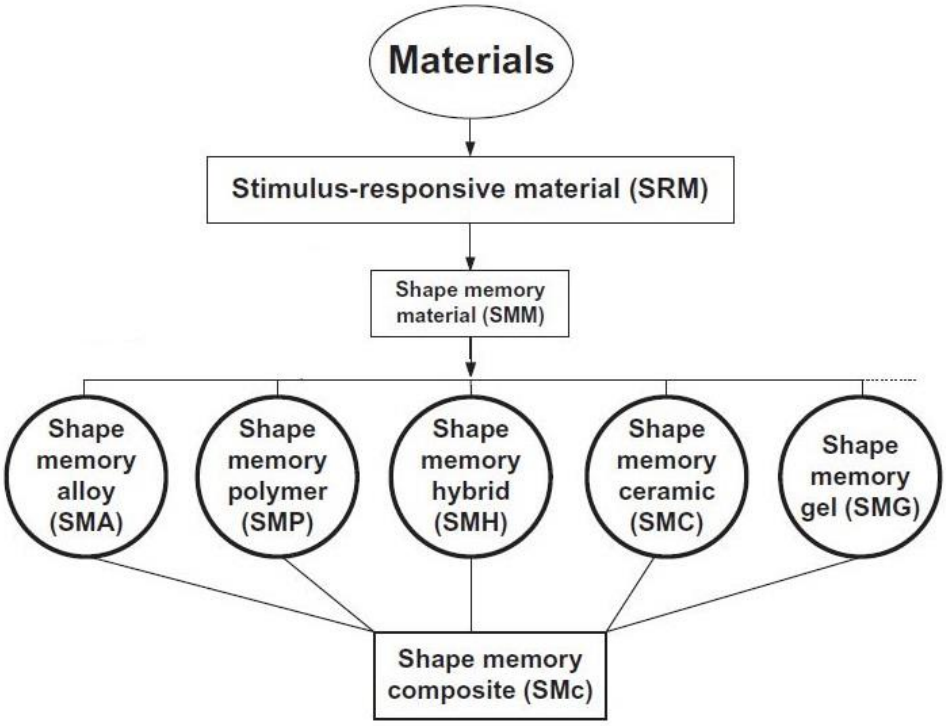

Figure 5. *Different types of SMMs within the material group [25]*

SMMs that are stimulus-responsive can revert to their initial shape following deformation or near-plastic deformation when exposed to a particular stimulus [30]. The most recognized variants of SMM include SMA and SMP. The underlying mechanism of SME in SMA is the reversible martensitic transformation, whereas in SMP, SME arises from a dual segment or domain structure [31, 32]. In addition to the SME, these materials also exhibit SE, where they can undergo large strains under external loading and return to their original shape after unloading [31, 32].

An additional category of SMM is the magnetic shape memory alloys (MSMA), combining ferromagnetic characteristics with SE and SME. Various other SMM types encompass Shape Memory Ceramics (SMC), Shape Memory Hybrids (SMH), Shape Memory Gels (SMG), and Shape Memory Composites (SMc). SMC may exhibit the reversible phase transformation principle of SMA or a multiphase system similar to SMP, while SMH consists of at least two components but without a single SME, having the same mechanism as SMP [18, 30, 33]. SMc are characterized as composite materials containing at least one SMM element, typically either SMA or SMP, incorporated within a foundational matrix [30, 31]. It is worth noting that all SMM exhibit the SME, which will be explained in further detail later [30].

2.3. Shape memory alloys (SMA)

SMAs are distinctive alloys with a unique ability to recall their original shape. When distorted, they can revert to this initial form under a specific stimulus, often temperature-driven. They possess two principal crystalline structures: Martensite and Austenite. In colder environments, they predominantly exist in a thermoelastic martensite state, transitioning to austenite as temperatures rise [30].

Two central properties characterize SMAs: SME and SE. SME describes an SMA's capacity to revert to its initial shape by heating after it has experienced plastic deformation and has been unloaded. This entails a phase transition: from martensite to austenite with heating, and back to martensite during cooling [31]. SE, on the other hand, endows SMAs with the resilience to undergo extensive strains (in the ballpark of 8-10%) under applied load and to spring back to their primary form once unloaded. SE is dominant at higher temperatures, resulting in energy retention, while SME provides both motion and force. Rooted in these characteristics, SMAs bifurcate into Superelastic Shape Memory Alloys (SE-SMA) and Martensitic Shape Memory Alloys (SME-SMA). Based on the reversibility factor of SME, SMAs can also be segmented into one-way and two-way classes. One-way SMAs demonstrate a one-directional shape restoration, requiring heat to revert. Conversely, two-way SMAs feature bidirectional shape recovery, enabling cyclical shifts between their altered and original shapes [30].

Owing to their unique SME and SE traits, SMAs are hailed as revolutionary "smart" materials, distinct from conventional metals or alloys [34]. They are typified as both thermo-responsive and magneto-responsive. The former is heat-activated, while the latter rely on static or alternating magnetic fields to kickstart the SME [25, 31]. The reversible martensitic transformation is the key mechanism behind these properties [25, 32]. Essentially, metallic materials that exhibit this reversible transformation can possess either the SME or SE and belong to the SMA group [25, 32].

There are many different alloys in this group, such as Au-Cd, Au-Cu, In-Tl, Fe-Pd, Fe-Pt and others [35, 36], but very few of these alloys are used industrially. Owing to their multifaceted utility and adaptability, two primary categories of alloys are predominantly employed: Nickel-based alloys, primarily founded on a binary Ni-Ti composition, sometimes

augmented with a tertiary element like Cu, Fe, Pd, or Hf, and copper-centric alloys, encompassing Cu-Al, Cu-Zn, Cu-Sn, Cu-Al-Ni, Cu-Zn-Al, Cu-Al-Mn, and Cu-Al-Be alloys [35, 36].

The intriguing SME was first pinpointed in 1932 by Swedish physicist Arne Oelander [37, 38], manifesting in an Au-Cd alloy. Astonishingly, the alloy, once deformed in cooler temperatures, sprang back to its innate shape when subjected to heat. This observation was mirrored in 1938 by Greninger and Mooradian [37, 39], who found identical properties in Cu-Zn and Cu-Al alloys. Marching into the 1940s, Kurdjumov and Khandros [37, 40] delineated the thermoelastic traits inherent to the martensite phase. Following in their footsteps, Chang and Read [37, 41] too observed SME in Au-Cd alloys.

A landmark moment arrived in 1961 when Muldaver and Feder employed an Au-Ag-Cd alloy in a thermally-driven electrical switch, acquiring the maiden patent for an SMA device [37, 42]. The following year, William J. Buehler, accompanied by his associates at the Naval Ordnance Laboratory, stumbled upon the SME in a Ni-Ti concoction. This alloy was christened 'Nitinol', an abbreviation representing Nickel-Titanium Naval Ordnance Laboratory [37, 43, 44]. This discovery marked a watershed moment in SMA history, heralding the dawn of revolutionary "smart" materials. This spurred a cascade of research endeavors, focusing on unraveling the enigmatic shape memory attributes of Ni-Ti. Pioneering the application of Ni-Ti as an implantable material in 1968 were Johnson and Alicandri [37, 45].

Nitinol's foray into the medical realm was recorded in the 1970s [24, 46]. The subsequent decade witnessed burgeoning enthusiasm for its orthodontic and largely experimental orthopedic uses. Overwhelming evidence of Ni-Ti's biocompatibility catalyzed an exponential growth in its application spectrum. These include biomedical devices and implants such as stents. It is also used in deployable engineering, aerospace, and electrical applications, such as actuators for aircraft wing control and space antenna.

SMA are smart materials that are known for their unique properties: the SME and SE. They are used in a variety of industrial, biomedical, and engineering applications due to their versatility and ability to respond to changes in temperature or magnetic fields.

2.3.1. Magnetic shape memory alloys (MSMA)

MSMA are a subset of SMA that have the additional property of ferromagnetic behavior. This combination of properties has earned MSMA the nickname of "Ferromagnetic Shape Memory Alloys." MSMA are known to have better fatigue resistance compared to traditional SMA. When an MSMA element is subjected to a strong enough magnetic field, a change in its shape and size occurs due to realignment of the twins and a shift in the twin boundaries in the microstructure, a phenomenon referred to as the Magnetic Shape Memory Effect (MSME) [47, 48].

Materials such as Ni-Mn-Ga, Fe-Pt, Co-Ni-Ga, Ni-Mn, Co-Ni-Fe-Ga, Fe-Mn-Se, Co-Mn, Ne-Fe-Ga, Fe-Ni-Co-Ti, Cu-Al-Ne, Ni-Mn-Fe-Ga, Co-Ni, Co2-Mn-Ga, and others have been identified as MSMA, but Ni-Mn-Ga and its derivatives have received the most attention from researchers [47]. It's imperative to emphasize that the Magnetic Shape Memory Effect (MSME) is uniquely manifested within the martensite phase of MSMA when subjected to lower temperatures. This effect noticeably diminishes and eventually vanishes as temperatures ascend, transitioning the material to its austenite phase.

Yet, the promise of MSMA is not without its challenges. A discernible drawback includes the hysteresis observed between the electric input current and the resultant strain. This hysteresis also extends to the relationship between the strain and stress. Complicating matters further is the 'first-cycle effect' and a pronounced sensitivity to temperature variations, both of which can substantially alter MSMA properties. Another notable constraint is the fluctuating relative magnetic permeability, which is contingent on the intensity of the magnetic field [47, 49]. On the brighter side, this intrinsic hysteresis amplifies the vibration damping capacity of MSMA, turning what is typically viewed as a limitation into a potential advantage [47].

2.3.2. Crystallography of SMA alloys

Central to the functioning and behavior of SMAs is their underlying crystallographic structure. The binary states, austenite and martensite, dictate their properties and consequent applications. Austenite, the high-temperature phase, showcases a more ordered, symmetrical

crystal structure in contrast to its counterpart, martensite. Martensite, stable under cooler temperatures, adopts a less symmetrical form. This innate asymmetry sets the stage for the alloy's transformation: transitioning from martensite to the symmetrical austenite enables the material to revert to its pristine shape [37].

While martensite is malleable, making it conducive to deformations especially at cooler temperatures and under significant stress, austenite is notably more rigid and finds stability at elevated temperatures and subdued stresses. The true marvel of SMAs emanates from this transformational shift between these two phases. The metamorphosis is rooted in an intricate rearrangement of atoms within the crystal lattice, a process characterized by the collective and synchronized movement of atoms spanning distances even less than the lattice parameters. Remarkably, the martensitic transformation, instigated either by temperature fluctuations or stress inductions, is near-instantaneous. The process forges ahead devoid of any diffusion, resulting in swift, responsive behavior that sets SMAs apart [37, 50].

Martensitic transformations in shape memory alloys (SMAs) involve a unique mechanism of deformation called twinning. This phenomenon is fundamentally different from the classical mechanisms seen in traditional metals. To grasp the intricate behavior of SMAs, an understanding of the martensitic twinning process is essential.

Twinning within the martensitic phase is an internal deformation process. In essence, it's like an atomic-scale mirror reflection where atoms shift symmetrically across a specific plane, termed the twinning plane. This process allows individual martensite variants to adjust and realign. When an SMA experiences stress, it doesn't immediately deform in the way typical metals do. Instead, it modifies the orientation of its crystal lattice through the shifting of these twin boundaries. This reorientation is reversible, allowing the alloy to revert to its original state when the stress is removed. Yet, if the stress applied goes beyond a certain threshold, the SMA will succumb to the standard, irrecoverable plastic deformation via atomic slip mechanisms. This deformation lacks the characteristic memory effect of SMAs [37].

The innate ability of SMAs to revert to their original shape arises from the disparity in the chemical free energy between the austenite and martensite phases. Consider an SMA subjected to deformation above its A_f (the temperature beyond which austenite remains stable): the transformation from austenite to martensite is purely instigated by the applied stress. This transformation progresses directly from the symmetric austenite phase to the deformed, less symmetric martensite phase. As the stress diminishes upon unloading, the inherent elasticity in

the alloy matrix nudges the deformed martensite plates back to their original alignment, reverting to the parent austenite phase.

Distinct from conventional metals that rely on the sliding movement of atomic planes (causing dislocations) to facilitate deformation, SMAs employ a detwinning mechanism. This process involves a shift in the tilt orientation of the internal twins, and it doesn't generate the movement of dislocations in the crystal structure. The martensite phase, being uniquely structured, can assimilate and integrate these dislocations to a degree. However, it's crucial to remember that the renowned shape recovery of SMAs is attributed to this detwinning mechanism and does not occur post a deformation process driven by the classical slip [37, 51].

The β-phase in copper-based alloys with an electron-to-atom ratio close to 3:2 is generally body centered cubic (b.c.c.). It has been shown that different martensite phases can form in each system and the phases formed at similar electron concentrations have a similar structure. Depending on the system, the phases at higher solute concentrations may be an ordered b.c.c. ($L2_1$) phase, a hexagonal close-packed structure (h.c.p.) phase, or a γ-brass type ($D8_2$) phase. At lower temperatures, an ordered b.c.c. (B2) phase, an ordered b.c.c. ($D0_3$) phase, an h.c.p. (A3) phase, or a two-phase mixture of α (face centered cubic- f.c.c.) and one of the above phases are in equilibrium [52].

Martensitic transformations in copper-based alloys represent a complex interplay of crystallography and metallurgy. The two principal mechanisms of deformation within the martensitic lattice in these alloys, rooted in their shift between various crystal structures, are especially intriguing.

1. From b.c.c. to f.c.c. transition:

- In this mechanism, the martensitic lattice undergoes a transformation from a body-centered cubic (b.c.c.) structure to a face-centered cubic (f.c.c.) structure.

- This shift induces what is referred to as lattice invariant strain, which manifests as slip within the lattice. Slip, in this context, creates stacking faults within the structure. These stacking shifts can either have a random distribution, a periodically ordered arrangement, or even alternate between layers exhibiting distinct crystal structures.

- A noteworthy point is the non-occurrence of a transformation from the b.c.c. structure directly to the *y*-brass type structure. The lattice alterations essential for this

transformation cannot be instigated by the shear and dilatational strains characteristic of martensitic transitions.

2. From b.c.c. to h.c.p. transition:

- This mode of lattice deformation sees the martensite transition from a b.c.c. structure to a hexagonal close-packed (h.c.p.) structure.
- Here, lattice invariant strain is driven predominantly by twinning within the lattice.
- Such transformations often result in large martensitic plates, making them ideal subjects for experimental studies. Moreover, these transitions typically take place below room temperature.

Martensitic phases are typified not just by their structural details, but also by their formation methods, microstructural attributes, and accompanying phase symbols. Delving deeper, martensite can be predominantly categorized into:

- β-type martensite: This type of martensite is defined by its lattice invariant deformation in the form of stacking faults.
- γ-type martensite: Here, the lattice invariant deformation manifests through twinning.

It's also worth noting that the martensitic structure can undergo orthorhombic and monoclinic distortions. Such distortions are triggered by ordering effects within the original, or parent, lattice. This behavior is reminiscent of the distortions seen in Fe-C martensite due to the positioning of carbon atoms within the lattice. The varying superlattice structures of the martensite, stemming from the diverse ordered architectures of the matrix phases in different alloy formulations, are indicated using distinct superscripts [52].

The martensitic transformation in copper-based alloys occurs in a matrix with an ordered b.c.c. structure, known as the β -phase. At high temperatures, the β-phase has a wide range of solid solution, but its stability decreases as the temperature decreases, resulting in a narrowing of the solid solution range. If cooled slowly, the β-phase will typically undergo a eutectoid transformation to form α and γ_2 phases below around 500°C. Below 500°C, an ordering transformation can also occur in which the β-phase transforms to β_1, which can have either a DO_3 type structure or a B2 type structure depending on composition and temperature, as seen in Figure 6. The ordering reaction is fast and is not suppressed by normal quenching,

although rapid cooling can prevent the long-range atomic diffusion of atoms that is required for the β_1 phase to decompose into martensite [52].

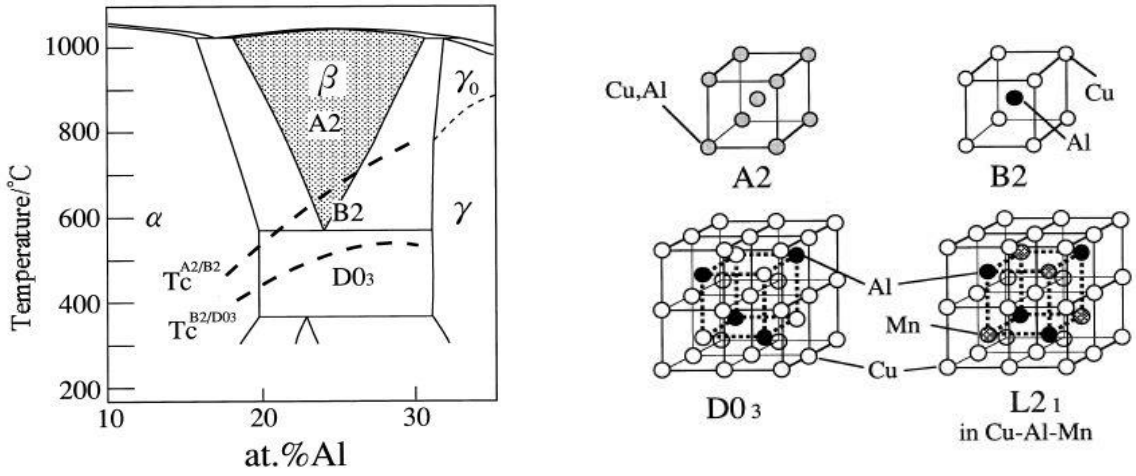

Figure 6. *The Cu–Al system's phase diagram displays the transition temperatures for the A2–B2 and B2–$D0_3$ order–disorder shifts. [53]*

The β-type martensite that is derived from a b.c.c. to f.c.c. transition has either a f.c.c. or an orthorhombic close-packed layer structure. The most common stacking sequences in these structures are 9R and 18R, and many of these close-packed structures have superlattices. The superlattices are believed to form because the martensite phases in the martensitic transformation inherit the atomic ordering of the parent phases. In copper-based alloys, the β-phases usually have either an Fe_3Al type (DO_3) superlattice or a CsCl type (B2) superlattice. The B2 structure is simple, consisting of one cell with a copper atom at the cell corner sites and a solute atom at the cell center site. The DO_3 structure is more complex, consisting of eight cells with copper atoms at all corner sites and at the center sites of four cells, and solute atoms at the other four cell center sites. The β_1' martensite structure is produced from the β_1 structure by shear and shuffling of the atomic planes. The β_1' martensite has either an ordered 9R structure or an ordered 18R structure, depending on whether it was derived from B2 order or DO_3 order, respectively [52, 53].

The vertical section diagrams in Figure 7 represent the Cu–Al–10 at. % Mn section. With the inclusion of Mn, there's an evident expansion in the single-phase domain. The transition temperatures linked with the order-disorder transitions in the b phase area (from A2 to B2 and from B2 to $L2_1$) display a significant drop as the Al content diminishes. From Figure

7., it can be inferred that the level of order in the b parent phase diminishes as Al content reduces [53, 54].

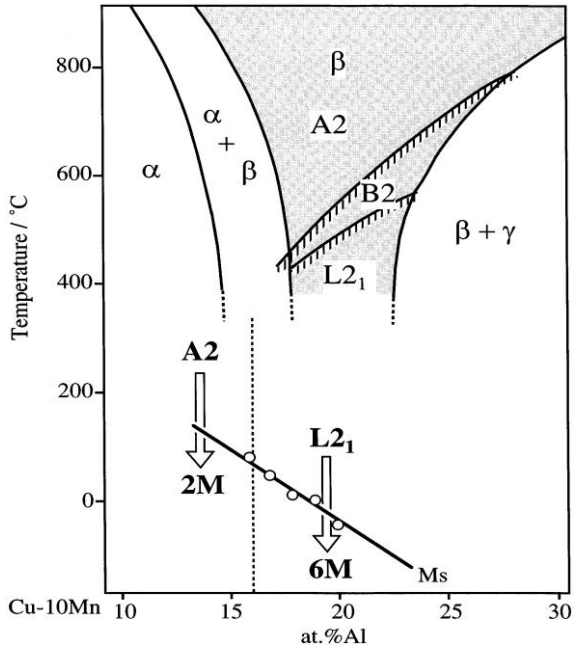

Figure 7. *Vertical section of Cu–Al–10% at. Mn alloy [54]*

In compositions with high Al content (greater than 16% at. Al), the transition to the $L2_1$ structure isn't halted by quenching from the disordered A2 phase. As a result, the $L2_1$ phase undergoes a martensitic change into a 6M structure with a six-layer modulation. On the other hand, with Al compositions under 16% at. quenching can prevent the ordering from A2 to $L2_1$. This leads to a martensitic transition from the A2 to the 2M (disordered f.c.c.) structure at colder temperatures [53, 54].

The Cu-Al binary alloy has two important phases, the α phase, which is a disordered structure rich in Copper, and the β phase, which is a less ordered structure rich in aluminum, seen in Figure 8.

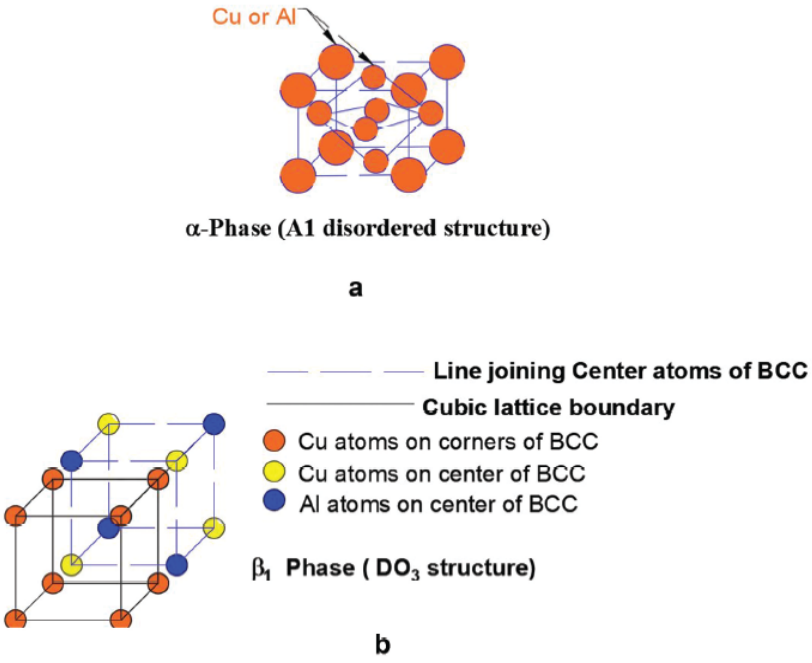

Figure 8. *a) α phase crystal structure., b) β_1 phase crystal structure [56]*

With the addition of Al and cooling below 850°C, the β phase transforms into the β_1 phase with a DO_3 structure [55]. This transformation can take place either through annealing, which leads to slow decomposition into the α phase and γ phase (Cu_9Al_4 intermetallic), or through quenching, which rapidly forms the β_1' and γ_1' ordered phases. The β_1' phase is a monoclinic 18R martensite, while the γ_1' phase is an orthorhombic 2H martensite [56, 57]. The structures of the γ_1' martensite and β_1' phase are shown in Figure 9. a and b.

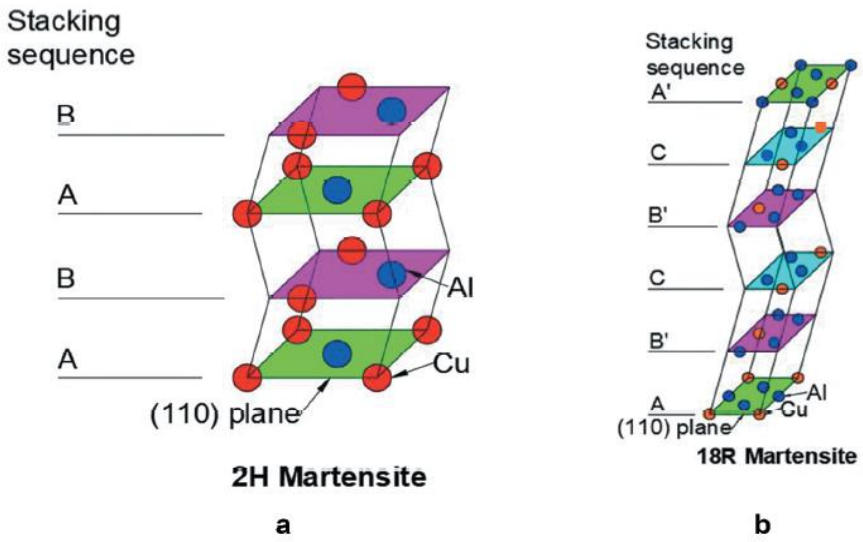

Figure 9. *a) γ_1'(2H) martensite crystal structure. b) β_1'(18R) phase crystal structure [56]*

Periodic structures with long-range stacking order and lower symmetry than the β_1 phase are significant in demonstrating shape memory characteristics [58]. While the γ_1' martensite displays a plate-like martensitic configuration, the β_1' phase manifests a needle-like structure [59]. The β_1' phase is particularly sought-after because of its enhanced potential for twinning during transformations triggered by temperature or stress, as it presents a reduced chance of dislocation entanglements [56, 58]. Conversely, the γ phase intermetallic compound, depicted in Figure 10., augments mechanical strengths but diminishes shape memory capabilities due to its reluctance to shift into lower symmetry configurations. Typically emerging at reduced cooling speeds, the γ phase can be circumvented with the right quenching techniques [55].

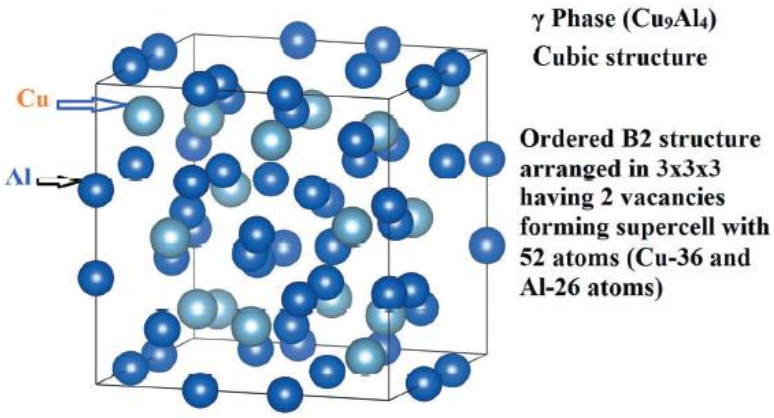

Figure 10. *γ' phase intermetallic compound crystal structure [56]*

2.3.3. Martensitic transformation

Four specific temperatures define the behavior of SMA: the austenite start (A_s) and finish temperatures (A_f), and the martensite start (M_s) and finish temperatures (M_f).

The transformation of martensite, which is a diffusionless transformation within the solid phase, toggles between the austenite phase at higher temperatures and the martensite phase at lower ones. This change in SMA, taking place approximately at room temperature, is both fully reversible and coherent, guaranteeing high reversibility during the process. In SMA, the orientation of the austenite crystal sets the direction for the adjacent martensite crystal. One

grain produces as many as 24 variants of martensite from austenite. These variants are crystallographically the same but differ in orientation and shearing planes. At cooler temperatures, SMA demonstrate SME, enabling them to revert to their original form once the external load is lifted. At high temperatures, SMA exhibit SE, which allows for instant and simultaneous recovery upon releasing the applied load, similar to a rubber band. The SME is a characteristic of the SMM, while the SE is a characteristic of the shape-changing material (SCM) [25, 60, 61].

The relationship among the various martensite variants in SMA can be described using group theory, which takes advantage of their symmetry [14]. The martensite variants tend to arrange themselves into twinned groups to minimize internal stress [62], and self-accommodation occurs in all transformations that are free from external stress.

In thermally induced martensite, there's no significant macroscopic shape alteration, but surface relief is noticeable [63]. This reversible surface feature has been leveraged to identify the actual transformation temperatures of SMA by observing changes in surface roughness or light reflection during thermal cycling. For real-time tracking of the transformation in smaller SMA specimens, this approach proves valuable, especially when traditional techniques like differential scanning calorimetry (DSC) might not be suitable [25].

Several non-traditional methods to analyze the transformation process exist, such as the indentation test, bulging test, photoelectron emission test, and curvature method [25, 64, 65]. Due to its in-situ characterization convenience, the curvature method is frequently used to explore the thermomechanical behavior of SMA thin films placed over an elastic substrate [66-68].

Depending on their thermal-stress background, SMA can transition between three distinct phases: austenite (A), twinned martensite (TM), and detwinned martensite (DM). It's possible for austenite and twinned martensite to coexist during stress-free thermal cycling. Figure 11. depicts the interrelationships of these phases and the six potential transformations between them. These transformations encompass processes like austenite converting to detwinned martensite under load (A → DM) and twinned martensite reverting to austenite upon heating (TM → A). The notations k and l represent different variants of the martensite phase [25, 69, 70].

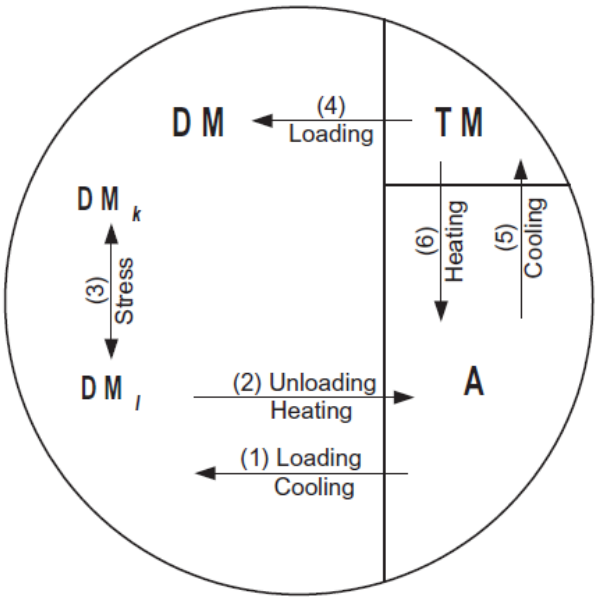

Figure 11. *Three phases and six transformations [25, 69]*

In Figure 12., the diagram depicts the alterations in lattice structures during specific transformations, though transformation (3) isn't included. The transformations A → TM and TM → A are unique in that, while they don't lead to visible macroscopic shape alterations, there is a pronounced surface relief. As a result, an austenite's smooth surface turns rough upon cooling to twinned martensite and smoothens again when reverted. It's essential to recognize that the attributes of an SMA can vary widely based on the phase in polycrystals or orientation in single crystals, stemming from disparities in their crystal structures or orientations [25, 71].

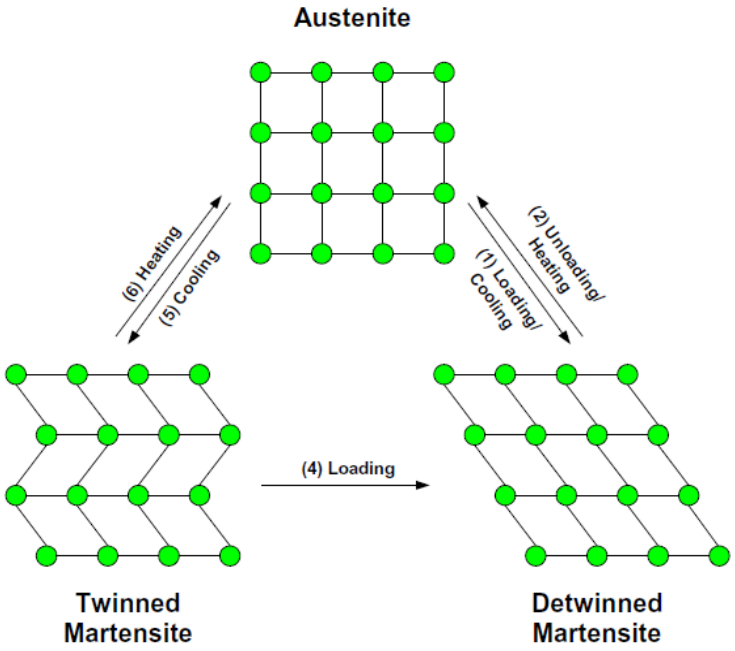

Figure 12. *Change in lattice structure [25, 69]*

Martensite Ni-Ti wire, besides commonly known characteristics like electrical resistivity, Young's modulus, thermal conductivity, and coefficient of thermal expansion, exhibits enhanced plastic and tearing energy when contrasted with austenite Ni-Ti wire. Two core transformation types exist in SMA: those between austenite and martensite, and transitions among various martensite variants. Factors influencing the thermo-mechanical behavior of SMA include not just stress, strain, and temperature, but also the phase. The Clausius-Clapeyron equation suggests that for a uniaxially extended SMA, the starting stress for transformation should correlate linearly with temperature. Yet, in both Ni-Ti and copper-based SMA, the starting stress might escalate to portray a V-shape or maintain consistency below a specific temperature, with this V-shaped relationship with temperature being exclusive to the cooling phase. The transformation leading from austenite to martensite demands the martensite phase's chemical free energy to be inferior to the austenite phases. But, non-chemical free energy components like transformation strain and friction energy also play roles. The transformation becomes feasible only when the energy difference surpasses the requisite non-chemical free energy. Conversely, the shift from martensite back to austenite happens when the energy gap, when considered with inverted signs, reaches an ample magnitude [25, 72].

The crystal transformations related to the SME are depicted in Figure 13. When the material is above the A_f, the parent phase is presented in Figure 13.a. Below the M_f, Figure 13.b displays self-accommodated martensite, which results in minimal macroscopic strain [37]. Without external forces, the crystal configurations transition between Figure 13.a during heating and Figure 13.b during cooling. Under stress, the positions of the martensite interfaces adjust, producing a mix of variants that align with the direction of the applied strain, as shown in Figure 13.c. Detwinning, the condensation of multiple twin variants into a single preferred martensite variant due to stress, takes place if the stress is sufficiently strong. When heated above A_f, the transformation reverts, restoring the original shape as seen in Figure 13.a. However, if the deformation isn't exclusively driven by twin boundary movement or if the transformation isn't crystallographically reversible, the full SME isn't achieved [37, 73-76].

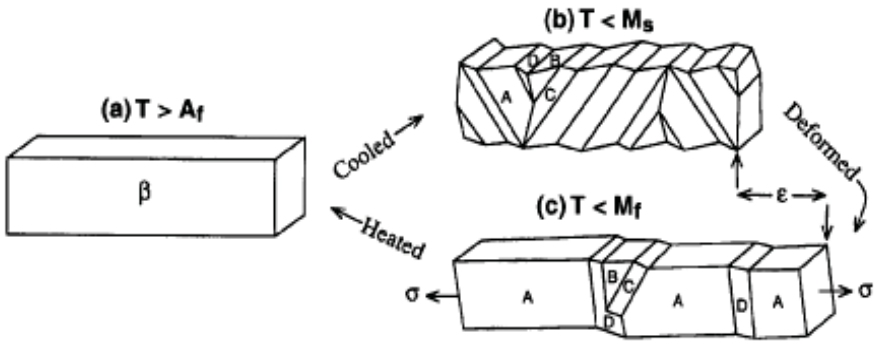

Figure 13. *SME Mechanism; (a) initial parent phase in a crystal, (b) self-accommodated transformation to martensite, (c) under stress, variant A prevails [37, 74]*

In SMAs, there's a distinct difference in physical properties between the austenite and martensite phases. As the transformation between these phases advances, these properties change. Temperature plays a pivotal role in this transformation, and four key temperatures (M_s, M_f, A_s, and A_f) dictate the transition from martensite to austenite and back again. To pinpoint these temperatures, one needs to observe how physical properties vary with temperature. However, this phase transformation exhibits a hysteresis, indicating that the transition temperatures aren't consistent during heating and cooling [37].

Typically, the hysteresis between the forward and backward transformations in SMAs is modest, ranging from 10 to 50 °C. This hysteresis loop originates from the free energy behaviors during the transformations and can be linked to the friction occurring when twin-

related martensite boundaries move. The hysteresis seen in the temperature-phase relationship is also influenced by the composition and treatment history of the alloy. For an accurate portrayal of SMA performance, the impact of stress on transformation temperatures needs consideration. When stress is applied, it pushes these temperatures higher, effectively moving the entire hysteresis curve. Figure 14. illustrates this temperature hysteresis in SMAs during the transformations between martensite and austenite [37, 77-79].

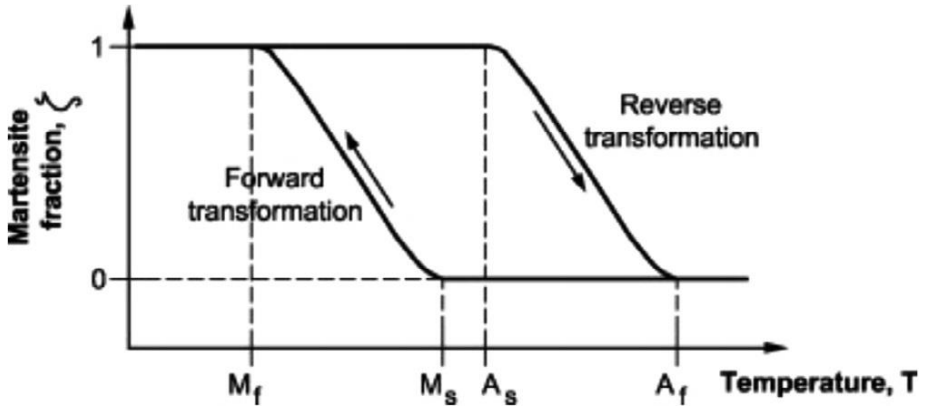

Figure 14. *Thermal hysteresis during phase transformation between martensite and austenite in SMA [80]*

In SMAs, the interplay between stress, strain, and temperature is intricate and does not follow a linear relationship, complicating the understanding of their mechanical behavior. Using the Young's modulus as an indicator of material stiffness isn't always applicable for SMAs because it's influenced by both temperature and strain. This modulus is contingent on the proportion of martensite and austenite phases within the material, which in turn varies with temperature and stress. As a result, pinpointing an exact modulus for SMAs becomes particularly challenging, especially in the temperature range between M_s and A_s [81]. To grasp the mechanical traits of SMAs, a comprehensive examination of their interrelationship between stress, strain, and temperature is vital [37]. The mechanical behavior of a Ni-Ti alloy, based on temperature variations, is depicted in Figure 15.

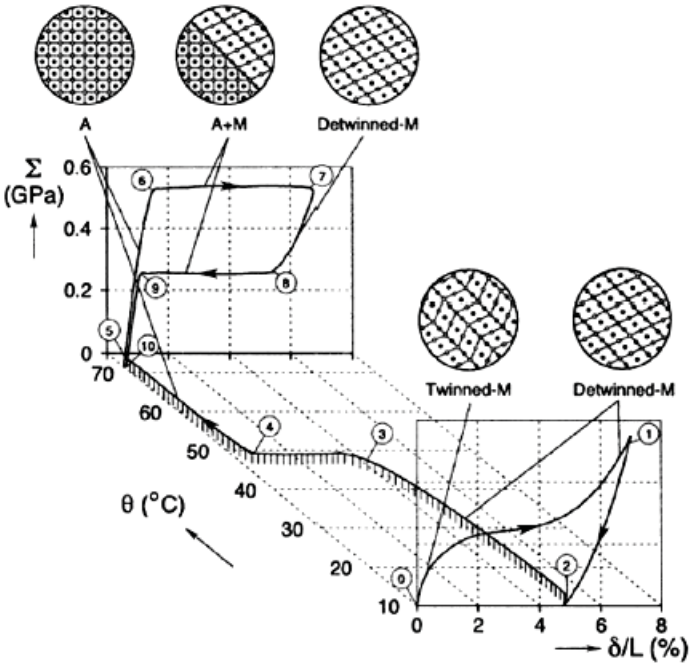

Figure 15. *Stress (∑) - strain (δ/L) - temperature (θ) relationship in Ni-Ti SMA alloy characteristic curve: shape memory effect 0 → 4; pseudoelastic response 5 → 10 [37, 82]*

In Figure 15., the material initially undergoes a load/unload cycle controlled by displacement at a lower temperature, resulting in a plastic strain of 5%. Beginning in its twinned martensite phase, the material detwins when loaded. Keeping the load slightly positive, the sample's temperature is raised, leading to the observation of the shape memory effect as strain recovers while transitioning to the austenite phase. When the temperature is maintained at a higher level, another displacement-controlled load/unload cycle is applied to the sample. During stretching, there's an increase in strain, which is then reversed upon unloading [37, 82]. SMAs are materials with unique mechanical properties, but they are difficult to describe due to the complex interdependent relationship between stress, strain, and temperature. The relationship between these properties is dependent on the phase fraction of martensite and austenite, which is in turn dependent on temperature and stress. To understand the behavior of SMAs, it is necessary to analyze their stress-strain-temperature relationship, and to understand how the mechanical properties change during the phase transformation from martensite to austenite. In Figure 16., the stress-strain response of a shape memory alloy is illustrated schematically.

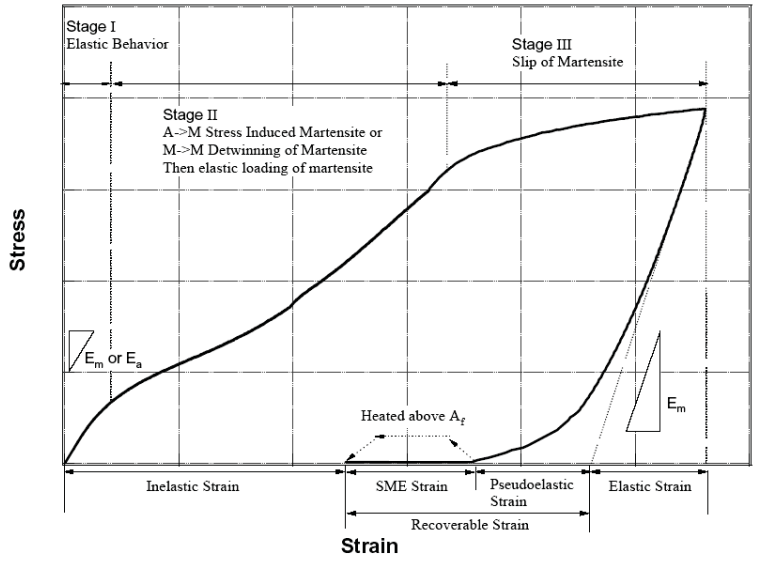

Figure 16. *Stress-strain behavior of SMA [37]*

In the graph, the plateau signifies the thermal hysteresis, arising from the frictional stress associated with twin boundaries governing both the martensite and austenite phases. The relative yield strength of martensite to austenite plays a pivotal role in assessing the resistance against both reversible and irreversible deformations. This is because martensite deforms through the movement of twin boundaries, while austenite deforms through dislocation generation and movement. The yield strength ratio determines the ratio of resistance to these two deformation mechanisms. It is therefore important for this ratio to be as high as possible in order to recover the greatest amount of deformation in shape memory alloys [37].

In other words, the stress-strain response of SMA is complex and depends on multiple factors, including the temperature, the relative proportions of martensite and austenite, and the yield strength ratio between the two phases. The plateau in the stress-strain response represents the thermal hysteresis that is a result of the frictional stress of the twin boundaries, which control the transformation between martensite and austenite. The yield strength ratio between the two phases is crucial in controlling the resistance to reversible and irreversible deformations and, as a result, the ability of the material to recover its original shape after deformation.

Figure 16. showcases the stress-strain behavior of a shape memory alloy, delineating the various stages of deformation and their influencing factors. The deformation mechanisms can be categorized into three distinct scenarios: In the scenario where the material is predominantly austenitic: Stage I involves the elastic deformation of the austenite. Stage II sees

the formation of stress-induced martensite, while Stage III is characterized by slip deformation. When the material is primarily in its martensitic phase: Stage I is marked by the elastic deformation of the martensite. During Stage II, detwinning of martensite leads to the dominance of certain variants over others. Stage III encompasses the slip deformation of martensite. In situations where the material initiates with a blend of austenite and martensite: Deformation incorporates elements from both the first and second scenarios. During unloading, the martensitic phase experiences elastic unloading across all mechanisms. SE strain succeeds the elastic strain (transformation from martensite back to austenite) in the first and third scenarios [37, 83]. Further elucidation on the stress-strain dynamics of shape memory alloys is given in Figure 17.

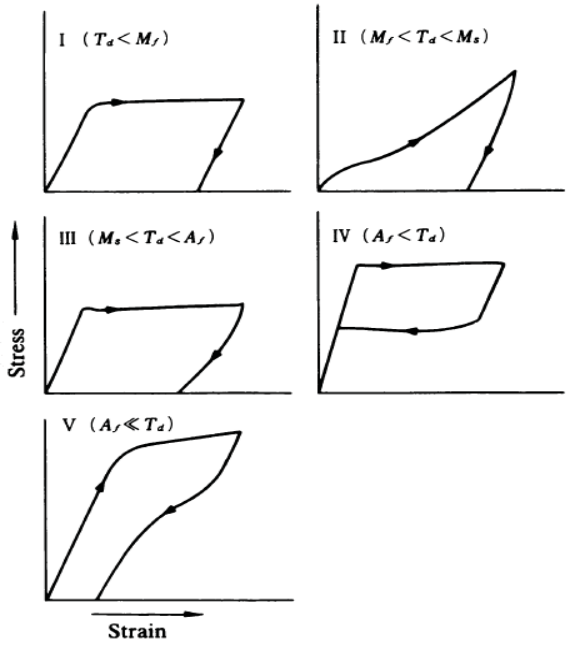

Figure 17. *Stress-strain curves for a SMA at different temperatures [37, 84]*

In the purely martensitic phase, the yield stress necessary to trigger martensite detwinning and generate significant strains is relatively low. Yet, the reversible strain is confined by the commencement of plastic slip within this phase. When the alloy's temperature is intermediate (M_f<T<A_f), its behavior becomes intricate, contingent on its state. The austenitic phase demands a considerably greater stress for yielding compared to the martensitic one. As temperatures approach A_f, the reason for yielding becomes the creation of stress-induced martensite (SIM). As the temperature exceeds A_f, the stress needed to prompt SIM intensifies until reaching a decisive temperature. Beyond this point, instead of SIM, plastic slip gets

activated [37, 84]. The stress-strain behavior of shape memory alloys hinges on the material's initial condition, the ambient temperature, and the exerted stress. The alloy can revert to its original configuration post-deformation by being heated past A_f, although the restorable strain diminishes as plastic deformation amplifies.

The training of SMA alloys is a process used to enhance and optimize this shape memory effect. The training of SMA alloys involves subjecting them to a series of thermal and mechanical cycles. The process typically begins with a process called "thermal cycling", in which the material is heated to a temperature above its transformation temperature, or the temperature at which the SME occurs. This causes the material to transform from the high-temperature, austenitic phase to the low-temperature, martensitic phase [23, 85].

Once the material has been transformed to the martensitic phase, it is then deformed or "trained" into a desired shape. The deformation can be accomplished using a variety of methods, including bending, twisting, or compressing the material. The deformation causes the martensitic phase to form a new, stable microstructure, which is retained even after the material is cooled below its transformation temperature. The trained SMA alloy can then be heated back above its transformation temperature, causing it to transform back into the austenitic phase and recover its original shape. The amount of shape recovery depends on the amount of deformation applied during the training process, as well as the conditions of the thermal and mechanical cycles. The training of SMA alloys can be optimized to achieve specific properties, such as higher shape recovery, faster recovery time, or increased durability. The training process can also be repeated multiple times to further enhance and refine the SME. Overall, the training of SMA alloys is a critical step in the fabrication and optimization of SMA for a wide range of applications, including actuators, sensors, and medical devices [85-87].

2.4. Copper-based SMA

Cu-based SMA are a promising alternative for high-temperature applications due to their lower cost compared to commercially available SMA. Using conventional liquid metallurgy and powder metallurgy techniques typical for traditional Cu-based alloys, these offer reasonably good shape memory characteristics that outperform Fe-based systems and are economical to manufacture [29, 57, 88]. Yet, polycrystalline Cu-based SMAs are prone to intergranular fracturing, a brittleness caused by the heightened elastic anisotropy that leads to stress build-up at grain boundaries and triple junctions. Many researchers have delved into diverse processing methods and compositional alterations, like introducing alloying elements for the purpose of grain refinement or the creation of precipitates, to enhance these mechanical attributes [5, 22, 23, 25, 27, 89]. Despite these efforts, the advancement in mechanical properties for polycrystalline Cu-based SMAs hasn't met the anticipated levels required for their integration into engineering systems [5, 90-92].

Due to their distinctive properties like SME and SE, SMAs have garnered significant interest, positioning them as apt choices for numerous applications. Among these, Cu-based SMA have emerged as a promising alternative due to their lower cost compared to other commercially available SMA. Cu-based SMA in their polycrystalline form can be vulnerable to brittle intergranular fractures due to the pronounced elastic anisotropy that results in stress concentrations at grain boundaries and triple junctions. While the remarkable shape memory characteristics are found in Cu-based SMA single-crystals, they're limited in oligocrystalline alloys, constraining their processing and potential applications. To enhance their ductility and manage grain size, research has looked into incorporating alloying elements like Mn, Ti, Zr, and Si in Cu-based SMA, indicating potential for broader applications in the future [25, 5, 22, 23, 27, 89].

Copper-based SMAs, primarily composed of Cu-Al-Ni, Cu-Zn-Al, and Cu-Al-Mn, are among the most frequently utilized [37, 93]. The dominant alloys in this category are Cu-Zn and Cu-Al, where a third element is typically introduced to modify transformation temperatures or the microstructure. To tackle the challenges preventing them from rivaling Ni-Ti SMAs in various applications, in-depth studies into Cu-based SMA categories have been undertaken. By doing so, it is hoped that the limitations associated with Cu-based SMAs, such as their

brittleness and aging, can be overcome, and their potential as an alternative to Ni-Ti alloys can be realized [23, 29, 57].

Cu-Zn-based SMAs are popularly recognized for their martensitic transformation, transitioning from an ordered parent phase that's body-centered cubic to a blend of monoclinic β' and orthorhombic γ' martensitic phases. However, their shape memory effect is capped at a recoverable strain of roughly 5%, constraining their applications. To enhance the M_s temperature and stabilize the parent phase, elements such as Ga, Al, Si, and Sn are incorporated. Among these, Cu-Zn-Al ternary blends stand out for their superior attributes, including heightened ductility and a robust resistance against grain boundary fractures [37, 93-95].

Cu-Al compositions with 14% wt. Al content boast an M_s temperature marginally above ambient conditions. But, alloys with Al concentrations surpassing 14% wt. are prone to the emergence of a non-transformative second phase, γ_2. Introducing Ni as an added component curtails γ_2 precipitation, although excessive Ni concentrations can induce brittleness in the alloy. Cu-Al-Ni blends, especially with an Al concentration near 14% wt. complemented by 4.5% wt. of Ni, are noted for their remarkable shape memory performance, thermal stability, minimal hysteresis, and economic viability [37, 94, 96].

Even though Cu-Zn-Al and Cu-Al-Ni SMAs often exhibit brittleness, primarily due to their expansive grain size, infusing minor amounts of metals like boron, cesium, or cobalt can mitigate this concern without jeopardizing their shape memory properties. However, ensuring these additions do not adversely affect the shape memory traits is crucial. The structural integrity of Cu-based SMAs hinges predominantly on their ability to withstand grain boundary fractures, a vulnerability that manifests readily. Factors like minimal grain size, reduced orientation dependency of transformation strain, and plastic deformation facilitation may be essential to curb this issue [37, 97].

The microstructure of Cu-based SMAs, which includes elements like grain size, phase stability, and their dispersion, significantly dictates their mechanical traits. Factors such as thermomechanical processing history shape these microstructural characteristics. Core functionalities of these alloys, such as transformation temperatures, recovery stress, damping ability, and hysteresis, are closely intertwined with the thermomechanical condition and microstructure/composition of the material. Cu–Al–Ni SMAs, for instance, can showcase transformation temperatures spanning from −200 to 200 °C and a thermal hysteresis between 20 to 40 °C. Their specific damping capacity, indicating the energy fraction dissipated relative

to the supplied energy, fluctuates between 10 and 20%. Despite inherent constraints of Cu-based SMAs, continuous endeavors aim to bolster their attributes, rendering them a worthy counterpart to other mainstream SMAs [5, 23, 25, 98-100].

Owing to their elevated transformation temperatures, Cu-based SMAs are eyed as promising candidates for high temperature shape memory alloy (HTSMA) purposes, outdoing other Cu-centered systems [98, 101]. One illustrative utility of Cu-Al SMAs is in the domain of HTSMAs, which are operational beyond 373 K. Certain Cu-Al-Ni single-crystals, for example, manifest a recoverable strain nearing 17%, retaining the shape memory effect past 473 K. However, potential structural ordering and equilibrium phase emergence stand as challenges for Cu-Al alloys in high-temp settings, possibly instigating shifts in transformation temperatures upon repeated thermal cycling [102]. There's ongoing research to devise novel Cu-based SMA compositions that sidestep these obstacles. Noteworthy blends delivering commendable SE and SME above 373 K encompass Cu-Al-Ni, Cu-Al-Nb, Cu-Al-Ni-Mn, Cu-Al-Ni-V, and Cu-Al-Ni-Mn-Nb [5, 98, 101-105].

2.4.1. Cu-Al-X (X=Mn, Ag) ternary systems

Cu-Al-Mn SMA were discovered in the late 1990s based on phase diagram studies and have excellent cold workability, particularly with relatively high manganese (Mn) compositions [53, 106]. Among SMA, the Cu–Al–Mn system has been gaining attention in recent years due to advancements in metal alloy manufacturing processes that enable the production of these SMA with controlled texture and grain size.

In a study by Kainuma et al. [53], it was deduced that alloys containing less than 14% at. of aluminum (Al) are characterized by two distinct parent phases: β (A2, disordered) and β_1 ($L2_1$, ordered, b.c.c. structure). For alloys with 16 and 17% at. Al, they primarily present the latter phase, which leads to superior shape memory attributes [107].

In the multifaceted Cu–Al–Mn systems, the martensitic phase at lower temperatures can manifest in three varieties: With a low Al concentration, α_1' (3R) emerges; β_1' (18R) appears within a medium range, and at elevated Al levels, γ_1' (2H) becomes dominant. Notably, the Cu–17Al–11Mn blend showcases the most robust SE characteristics among Cu-based SMAs, even surpassing the recoverable strain found in Ni-Ti [107-109].

Polycrystalline Cu-Al-Mn SMAs, differing from Ni-Ti SMAs, have a pronounced crystallographic anisotropy in transformation strain. This can lead to grain orientation mismatches at grain boundaries, inducing dislocations easily [110, 111]. The ensuing accumulation of such dislocations reduces SE and results in intergranular fractures. One remedy for this issue is texture control, which ensures uniform grain orientation through cold work followed by heat treatment [100, 111-113]. This consistent grain orientation enhances the shape memory behavior of Cu–Al–Mn SMAs, removing obstacles for martensitic transformation and elevating transformation temperatures concurrently [29].

In recent developments, 2013 witnessed a groundbreaking method to produce Cu–Al–Mn alloy samples with remarkably vast grain sizes, spanning several centimeters. This was achieved solely through cyclic heat treatment between a β (b.c.c.) single-phase and a $\beta + \alpha$ (f.c.c.) two-phase domain. Progressing further, the fabrication of single crystal rods measuring up to 0.7 m was realized [114]. When the relative mean grain size is augmented relative to the sample's cross-sectional area, the SE performance of Cu–Al–Mn alloy substantially improves [113]. Such outstanding SE properties have been illustrated in sizable samples [114, 115], paving the way for their potential usage in large-scale architectural and civil engineering applications [25, 114, 115].

Omori and colleagues [116] undertook an assessment of the transformation-induced shape memory attributes of pliable polycrystalline Cu–Al–Mn alloys, utilizing a bending pre-deformation approach. They managed to reach a peak value of #TW = 3.2% after enduring approximately 12.5% pre-deformation strain [100, 116]. To further advance the ductility and SME traits of Cu–Al–Mn alloys, Omori et al. [115] alongside Liu et al. [117, 118], employed microstructure control to produce bamboo-like-grained and columnar-grained alloys respectively. Owing to the prominent grain orientation and size, the mechanical characteristics of these polycrystalline alloys can rival those of single crystals [119].

Nonetheless, there remain challenges with Cu–Al–Mn SMAs. The crucial stress required for inducing martensitic transformation and the fatigue strength of Cu–Al–Mn SMA are relatively minimal, constraining their real-world applications. Grain refinement, aging, and alloying present viable solutions to enhance their attributes and expand their functional properties [120-122].

Investigations into the Cu-rich domain of the Cu–Mn–Al system have been exhaustive for temperatures surpassing 450 °C. Through the introduction of Mn, the high-temperature β

phase field of the Cu–Al system gets broadened [10]. The stability range for the β phase grows with rising temperature, encompassing the composition of the notable Heusler alloy Cu_2MnAl when the temperature exceeds 650 °C [53, 123]. At a temperature of 400 °C, the dominant phases within these alloys are γ, Cu_3Mn_2Al, and βMn [123]. For temperatures below 326 °C, a spinodal decomposition might arise between a nonmagnetic (DO_3) Cu_3Al-rich phase and a ferromagnetic-ordered ($L2_1$) Cu_2AlMn-rich phase [123]. Depending on the concentrations of Al and Mn, the pivotal temperature for martensitic transformation can vary, ranging from approximately -73 °C to about 100 °C [10, 124].

Past studies suggest that Cu–Al–Mn SMAs possessing an Al content less than 18% at. exhibit commendable cold workability, impressive ductility, and adequate SME and SE characteristics. Due to the A2 phase region's transition to a reduced Al range, the precipitation of the γ_1 (Cu_9Al_4) phase, which might lead to reduced thermal working stability and increased intergranular fractures, is prevented [125, 126]. With diminishing Al levels, shape recovery also gets a boost, as the parent phase (or the austenitic phase) has a muted order degree that is conducive for martensitic transformation. The parent phase for the malleable Cu–Al–Mn SMAs lies within the Cu–Al binary domain, which gets substantially widened by adding 8% at. Mn and 17% at. Al, leading to a synergy of grain size and texture management [29]. In terms of SE strain, Cu–Al–Mn alloys match the levels seen in Ni-Ti alloys and display other functional attributes like TWSME and superior damping capabilities [29]. These alloys also spark interest at a foundational level since they offer insights into the interplay between magnetic, elastic, and configurational properties [12].

To sum it up, the Cu–Al–Mn SMA system is emerging as a promising candidate, boasting attributes like elevated SE (exceeding 10%) [118], a significant isothermal entropy shift (1.4 J $mol^{-1}K^{-1}$), an expansive operational temperature span (surpassing -173 °C) [127], coupled with its manufacturing simplicity and cost-effectiveness when contrasted with Ni-Ti-based SMAs [128].

In these alloys, martensitic stabilization can be curtailed via up-quenching treatment, which decreases the vacancy concentration. However, to effectively counteract martensitic stabilization, as the recovery heating rate diminishes, there's a continuous need to lengthen the up-quenching time. It's not financially sustainable to endlessly prolong the up-quenching duration to counteract martensitic stabilization that's reliant on the heating rate [129]. The

constraints posed by heating rate-dependent martensitic stabilization have hampered the widespread utilization of malleable Cu-Al-Mn alloys [130].

Tadaki's research [23] has illustrated that aging while in the martensitic state, a process termed martensitic stabilization, hinders the backward transformation of martensite in Cu-based SMAs. As evidenced by Leu and Hu's research [131], the SME of the $Cu_{-25.6}Zn_{-3.94}Al$ (% wt.) alloy diminished by roughly 60% post aging in the martensitic phase at ambient temperatures for 104 seconds. A plethora of research has underscored that the occurrence of martensitic stabilization in Cu-based SMAs is predominantly due to the dynamics of filled vacancies [129]. Suggestions by Aydogdu and team [132] posit that there's a tight link between martensitic stabilization and variations in order level, which are spurred by an excess of vacancies during the aging of martensite. Insights from Ahlers and Pelegrina [133] indicate that atom redistribution due to vacancy mobility, encompassing both short and extended-range reordering's, is the catalyst for martensitic stabilization. Research conducted by Ren and Otsuka [134] emphasizes that the trend of short-range ordering of vacancies that matches the symmetry is the origin of martensitic stabilization. Proposals from Kustov and colleagues [135, 136] infer that the engagement of quenched-in vacancies by moving interfaces plays a pivotal role in inducing martensitic stabilization. As such, the tactic of up-quenching treatment has been employed to reduce vacancy concentrations and stifle martensitic stabilization.

Drawing from findings by Leu and Hu [129], up-quenched specimens of the $Cu_{-27.4}Zn_{-3.72}Al$ (% wt.) alloy consistently showcased a more robust SME in contrast to as-quenched samples post aging at room temperatures, whether the duration was less than 10 minutes or extended to 5400 minutes. A study spearheaded by Lam et al. [137] delineated that in the $Cu_{-10.23}Al_{-4.80}Ni_{-1.74}Mn_{-0.55}Ti$ (% wt.) alloy, the heat uptake triggered by the reverse martensitic shift stood at a mere 3.8 J g^{-1} for as-quenched specimens but saw an uptick to 7.5 J g^{-1} after a 120 minute up-quenching session at 100 °C.

Over the span of several decades, myriad studies have been undertaken to uncover the root cause of martensitic stabilization. The consensus that has emerged suggests that the phenomenon of martensitic stabilization is intimately tied to vacancy behaviors. These behaviors include kinetic stabilization, where moving interfaces are pinned by vacancies [135, 136], static stabilization, which involves a shift in either long-range or short-range order due to the redistribution of vacancies [132, 133], and the symmetry-conforming short-range order, a process where there's an atomic reshuffling within the same martensite sublattice propelled

by vacancy movements [51]. As a result, methods such as up/step-quenching treatments were introduced to lower the concentration of vacancies and thus mitigate the onset of martensitic stabilization [130, 138].

However, findings from Yang and colleagues [139] revealed that the duration of up-quenching needed to counter martensitic stabilization is heavily influenced by the recovery heating rate. To be precise, in a $Cu–_{17.0}Al–_{10.5}Mn$ alloy (specified as % at. henceforth) that was quenched to room temperature post a solution treatment at 850 °C, a mere 15 minutes of up-quenching sufficed to counter martensitic stabilization, but only when the recovery heating rate surpassed 20 K min^{-1}. If this rate plummeted to 1 K min^{-1}, the up-quenching period necessary to ward off martensitic stabilization ballooned to a minimum of 180 minutes.

Given the application settings of SMAs, recovery heating rates can be incredibly sluggish. Yet, it's not economically viable to endlessly stretch the up-quenching duration to counteract martensitic stabilization. Therefore, instead of attempting to eliminate saturated vacancies via up-quenching treatments, it would be more strategic to mull over ways to curtail their formation from the get-go [129].

Gottstein's research [140] highlighted that the number of vacancies at equilibrium correlates with temperature. In the process of quenching the $Cu–_{17}Al–_{10.5}Mn$ alloy from its solution temperature down to room temperature (RT), the quenching duration was too brief, preventing vacancies from effectively migrating and then getting annihilated. This meant that most vacancies that existed at the solution temperature persisted in the quenched alloy, leading to the phenomenon of saturated vacancies. One way to minimize these saturated vacancies at the root is by reducing the equilibrium concentration of vacancies present at the solution temperature. However, it's essential to ensure that SMAs are constrained during the solution treatment to prevent any unwanted shape alterations. The manner in which constraints are applied can modify both the internal stress field within SMA samples and the quenching's cooling rate.

Further insights by Cao and Wang pointed out that as internal stress rose, there was a corresponding increase in the change in vibrational entropy per vacancy [141]. Sueoka's studies provided theoretical evidence that as internal stress grew, the formation enthalpy for vacancies diminished, a finding that was subsequently validated experimentally by Nakamura's work [142, 143]. Gottstein's studies affirm that both vibrational entropy and the formation enthalpy of vacancies play significant roles in determining vacancy concentration [140].

Moreover, Ishibashi and colleagues discovered that samples quenched in water had a notably higher vacancy concentration compared to those cooled in a furnace. This indicates the pivotal role the quenching's cooling rate plays in determining vacancy concentration [144]. Yet, there is a dearth of research probing into how constraining samples during solution treatment impacts vacancy concentration and, in turn, martensitic stabilization.

In the malleable Cu-Al-Mn alloys, the Al and Mn atoms positioned themselves as next-nearest neighbors within the $L2_1$ structure [141]. Further research by Nakata and colleagues demonstrated that in the $L2_1$ structure, there's potential for the Ni and Al atoms to bond as nearest neighbors [142]. Delving deeper, Tan and his team found that the interaction strength between Ni and Al atoms, gauged at -90.3 kJ mol^{-1}, was superior to that between Mn and Al atoms, which was measured at -76.8 kJ mol^{-1} [144].

Yang embarked on a mission to amplify atomic bonding strength, aiming to limit the activity of vacancies by infusing Ni into the ternary Cu-Al-Mn alloy mix [129]. The effort bore fruit, leading to an enhancement in the shape memory effect (SME) when Ni, up to a concentration of 2% at., was added to the ternary Cu-Al-Mn alloys. Upon heating, the SME of the ternary Cu-Al-Mn alloy stood at 85%, but it saw an uplift to 92% with the introduction of 2% at. Ni. As a consequence of this addition, vacancy behaviors were constrained, leading to the suppression of heating rate-dependent martensitic stabilization in the Cu-Al-Mn-Ni alloy, where Ni constituted 2% at.

Damping capabilities are a significant aspect of Cu-Al-Mn SMAs, with numerous studies delving into their optimization [145]. Lu highlighted how the damping efficiency of the martensite phase in Cu-Al-Mn SMA gets influenced by the inclusion of Ce, showcasing an initial increase followed by a decline as the Ce content rises [146]. By employing a pillar structure, Li was able to heighten polymerization, thereby enhancing the damping properties of spherical porous Cu-Al-Mn SMA [147]. Mielczarek discovered that the austenite phase damping in as-cast Cu-Al-Mn SMA, dependent on amplitude, grew with heightened cold rolling levels, even though the damping in the biphasic region diminished [148]. Post-weld laser processing, as per Oliveira, amplified the energy absorption capabilities of Cu-Al-Mn SMA by a factor of 1.7 during mechanical cycles [149]. Koeda determined that the damping efficiency of the ductile Cu-Al-Mn SMA positively correlated with the relative grain size [150]. Conversely, Sutou identified an elevation in the damping capabilities of Cu-Al-Mn-based SMA due to the emergence of {112} <110> texture, achieving a considerable damping coefficient

tan Φ of 0.09 from the martensite phase textured sheet alloy with a grain size ratio of 1.34 [151]. However, Yang posited a contrasting observation, noting that Cu-Al-Mn SMA's damping capabilities increased as the average grain size decreased [152].

Mallik observed that a 300 ℃ aging treatment refined the Cu-Al-Mn alloy's transformation temperature, though its damping efficiency was curtailed due to precipitate formation. Upon aging at 500 °C, the alloy witnessed no martensitic transformation, attributing this to an Al-rich precipitate phase, thereby adversely affecting the alloy's damping traits [153]. Jiao's insights pointed to the damping capacity of Cu-Al-Mn SMA rising and subsequently dropping with the escalation of solution treatment temperature, peaking at 825 ℃ [154]. Wang examined a novel porous Cu-Al-Mn SMA's microstructure and damping behavior post an aging treatment, discerning an increase in both the martensite phase's damping properties and the internal friction peak of reverse phase transformation upon 350 °C treatment [155]. Lastly, Li's study showcased that specific aging treatments at temperatures of 300 ℃, 350 ℃, and 400 ℃ considerably amplified Cu-Al-Mn SMA's damping efficiency. This capacity in columnar-grained Cu-Al-Mn SMA is associated with the bainite phase content during aging. Moreover, the synergy between the martensite interface and bainite phase mirrors the pinning and depinning mechanism, suggesting that achieving a particular bainite phase content leads to increased energy dissipation, hence enhancing the alloy's damping capacity [145].

Overall, these advances in alloying and composites hold promise for the development of new and improved Cu-Al-Mn SMA with enhanced mechanical and damping properties for various applications, including civil engineering and architecture.

The Cu-Al-Ag ternary system is an extension of the broader group of Cu-Al-based shape memory alloys (SMAs). Historically, this system has garnered extensive research attention. The binary Cu–Al system inherently possesses a lofty transformation temperature. However, introducing Ag can modify the martensitic transformation's nature, precipitating thermoelastic transformation and the shape memory effect [47, 156, 157]. Characteristically, Cu-Al-Ag alloys undergo martensitic transformation at temperatures exceeding 200 °C, associated with an enthalpy change within the range of 10-12 J g^{-1}. An elevation in Ag concentration introduces α_2- and γ phases, which diminish the enthalpy achieved during the transformation but don't influence the transformation temperatures [158, 159].

The increasing content of Ag correlates with alterations in the M_s temperature. A heightened Ag concentration can augment our comprehension of the phase stability dynamics when the sample undergoes thermal cycling between M_f and A_f temperatures [160].

Ag's inclusion in the alloy also prompts discernible changes at the microstructural level, especially concerning the morphology and distribution of the martensitic transformation. Moreover, the alloy witnesses the emergence of Ag-enriched precipitates, particularly in the $AlAg_3$ and Ag_3Al phases. Such microstructural adaptations lead to considerable elevations in transformation temperatures. When cooled slowly, the presence of Ag impedes the decomposition of the β- and β_1-phases, culminating in the genesis of the martensitic phase. Yet, when subjected to swift cooling, a novel thermal event materializes, and the reverse martensitic transformation is observed to gravitate towards reduced temperatures [10, 158-161].

To date, there is little information on the influence Ag in the Cu–Al–Ag system SMA on martensitic transformation, phase formation and microstructure morphology. Reduced grain size, transformation temperature shifts and enhanced functional properties could be achieved by microalloying with other elements, mostly with B, Ti, Zn, Ni, Si etc. [162]. Addition of silver to binary and ternary Cu-based SMA alloys is less often investigated, but previous results showed improvement of corrosion resistance, increasing of transformation temperature and enhanced microhardness [10]. Further, silver addition to ternary Cu-Al-Mn alloy increase ferromagnetic $L2_1$ phase fraction and magnetic properties [163]. Ternary Cu-Al-Ag alloys are specific among Cu-based SMA alloys due to high temperatures of martensitic transformation [164], mostly from 200 – 600 °C, in dependence of aluminum and silver composition, which enables application in specific areas.

2.4.2. Microalloying of ternary systems

Alloying in Cu–Al–Mn SMAs has been studied extensively in order to improve not only the mechanical properties but also the shape memory effect (SME), critical stress for inducing martensitic transformation, and fatigue strength, to further benefit its practical applications. The addition of quaternary elements such as Ti, Co, Zr, B, Mg, Ni, Ag, Fe, or Cr into the main phase has been explored in many previous studies [110, 112, 125, 152, 162-164].

It is known that the disordered β-phase in Cu–Al–Mn SMAs is stable at high temperatures and transforms into the β(A2) → β_2(B2) → β_1($L2_1$) ordered phase during quenching. Above 16% at. Al, Cu-Al-Mn alloys exhibit a shape memory effect (SME) based on β_1 ($L2_1$) to monoclinic β1 martensitic transformation [53, 153, 165].

Adding 1.7% at. Mg or 1.4% at. Fe elements to ternary Cu-Al-Mn alloys has been shown to enhance ΔS from 0.68 J $mol^{-1}K^{-1}$ to 1.42 J $mol^{-1}K^{-1}$ and 1.15 J $mol^{-1}K^{-1}$, respectively, suggesting that adding alloying elements may be a way to improve ΔS of Cu-Al-based SMAs. However, previous investigations have also found that Cu–Al–Mn-based SMA can exhibit b.c.c. phase separation or liquid separation phenomena resulting from the additions of Fe, Cr, and V [120, 165, 166].

The study of shape memory alloys, particularly within the Cu–Al–Mn system, has shown that quaternary additions can lead to complex microstructural and property alterations. Here's a synthesis of the given information:

Mallik and Sampath [153] delved into the effects of eight distinct quaternary elements on the Cu–Al–Mn alloy system. Their investigation covered various attributes like transformation temperatures, shape memory effects, and superelasticity. On a parallel note, Sutou and his team [151] discovered that by introducing B, Ni, or Si, they could diminish grain size, which they recognized as crucial for improving damping and mechanical attributes of the alloy. In particular, the integration of Ni into the Cu–Al–Mn SMA system has been hailed for fostering a fine-grain microstructure, thereby enabling superplasticity within a specific temperature band [29]. However, the micro-additions of other quaternary elements to this alloy can augment its shape memory characteristics, but this may come at the cost of reduced transition temperatures. This has led to a consensus that for desired higher transition temperatures, the ternary system might be more appropriate [29].

In the Cu–Al–Mn–Fe alloy system [120], introducing Fe plays a pivotal role in promoting bcc phase separation into Cu-rich and Fe-rich phases, a prerequisite for the stabilization of the stress-induced 2H (γ_1') martensite. The presence of minuscule Fe-rich precipitates serves as a barrier to the movement of the habit plane during the reverse transformation. Drawing from this observation, it's posited that the stabilization of stress-induced martensite could similarly manifest in other Cu–Al–Mn-based systems which showcase b.c.c. phase separation.

Furthermore, in the realm of the Cu–Cr binary, there exists a metastable liquid two-phase separation, with pure Cr embodying a b.c.c. (A2) structural configuration [120]. Examination of the Al–Cr and Mn–Cr binary systems indicates that the b.c.c. A2 (Cr) phase shares a broad compositional spectrum with both Al and Mn. Consequently, it's hypothesized that in the Cu–Al–Mn–Cr system, liquid two-phase separation between Cu-rich and Cr-rich phases, along with the stabilization of stress-induced martensite, may transpire, mirroring the behavior seen in the Cu–Al–Mn–Fe system. Lastly, the Cu–V binary showcases a metastable liquid two-phase separation, but the specifics of its solid solution are yet to be fully understood.

Overall, these studies highlight the potential benefits of alloying in Cu–Al–Mn SMA for further improving their mechanical and functional properties. However, it is important to carefully consider the effects of different quaternary elements on the microstructure and phase stability of the alloy to avoid unwanted phase separation or changes in transformation temperatures. Future research could focus on exploring new quaternary additions and optimizing their concentrations to achieve desired improvements in mechanical and functional properties of Cu–Al–Mn SMA.

The effects of various elements as microalloying additions on the functional attributes of Cu-Al-Mn alloys have been examined. Nickel's microalloying outcomes indicated a reduction in grain size and an enhancement of the shape memory effect. However, there's also a decrease in the alloy's ductility and a downward shift in martensitic transformation values [128, 139, 151, 166]. Notably, nickel, as well as microalloying elements like Sn, Zn, and Au, are fully soluble in the β-phase, resulting in a unified system. This differs from microalloying the Cu-Al-Mn alloy with elements like Cr, Fe, Ti, V, Si, and Co, which show reduced solubility in the matrix and a predilection for precipitation [130, 151].

Furthermore, augmenting the Cu-Al-Mn SMA alloy with elements like Au, Co, and Zn doesn't bolster the material's ductility or its inclination for cold deformation. In contrast, introducing Sn into the ternary blend notably diminishes its ductility [153]. Among the elements not wholly soluble in the β-phase, Fe exhibits the most pronounced microalloying impact on Cu-Al-Mn alloys' features. Depending on its concentration, it can elevate the martensitic transformation temperature. Research indicates that incorporating Ti, Co, Cr, and Si generally results in inferior mechanical attributes for Cu-Al-Mn SMA alloys [10, 12]. However, magnesium's microalloying has a negligible impact on the ternary alloy's properties and doesn't alter the martensitic transformation temperatures [166].

On the subject of the influence of silver on the properties of Cu-Al-Mn alloys, not so many papers have been published SMA. Silva [10] points out that the hardness, corrosion resistance and ageing properties are improved by the addition of silver to Cu-Al alloys. Silva [10] studied the alloy with composition Cu-11Al-10Mn-3Ag and found that silver increases the magnetic properties of the material, while Santos [12] reported an increase in the microhardness of the ternary alloy by adding 3 at. % Ag, which is due to the formation of bainite. The presence of Ag allows the formation of martensitic phases in slowly cooled samples [167].

In studies conducted by Motta [9] and Silva [168], it was highlighted that the isothermal bainitic precipitation's activation energy in the $Cu_{69.3}\,Al_{18.8}\,Mn_{10.3}\,Ag_{1.6}$ alloy diminishes due to the incorporation of Ag atoms in the bainitic phase's crystal lattice. Silva [169], in a subsequent study, also revealed that introducing Ag into a Cu-Al-Mn alloy elevates the temperature at which bainitic precipitation occurs and initiates competing reactions. Similarly, Salgado [170] noted that by adding alloying elements like Ag, Ga, and Gd to a $Cu_{74.5}\,Al_{15.0}\,Mn_{10.5}$ alloy, the dynamics of bainitic precipitation are altered. Specifically, the inclusion of Ag heightens the E_y for bainitic precipitation, but upon the formation of Ag precipitates, they expedite the bainite phase's development.

These studies focus mainly on high-temperature transformations, and the influence of silver on transformation temperature has been poorly studied. Manasijević [171] studied the influence of silver in alloys of Cu-9Al-1Mn-4Ag and Cu-9Al-5Mn-4Ag and found that in an alloy with a higher manganese content (5% wt.), complete martensite was formed in the as-cast state, while in alloys with 1 wt.% the manganese structure showed the appearance of α-phase precipitates in the partially formed martensite.

The effect of silver on the phase transformation of Cu-Al-Mn SMA alloys has also been studied. Krishna [56] found that with the increase of Al content from 8-12% in Cu-XAl-5Mn-2Ag alloy and constant Cu/Mn and Cu/Ag content, coarse martensite plates (γ_1' type martensite) are formed, α-phase decreases and needle β_1'-martensite increases, which increases the shape memory effect from 81 to 90%. In addition, Krishna [56] pointed out that the martensite transformation temperatures reduce with increasing Al content, the peak intensity of R phase (secondary peak) and the exothermic peak increase. The results of a few studies on the effect of silver on Cu-Al binary alloys have also shown that silver increases the temperature of martensitic and austenitic transformation in ternary systems [172]. Recent research on Cu-

Al-Mn alloys has focused on determining the elastocaloric effect (eC) of alloys, as the SMA alloys are increasingly considered as environmentally friendly materials in applications where SE properties and repetitive stress and strain cycles can be used for heat transfer [173].

Altering Cu-Al-Mn SMA alloys with microalloying elements can significantly influence their properties. Nickel, for instance, has been demonstrated to reduce grain size and enhance SME, but it compromises the alloy's ductility and shifts the martensitic transformation downwards. Among elements that don't fully dissolve in the β-phase, Fe exerts the most pronounced microalloying effect on Cu-Al-Mn alloys. Conversely, elements like Ti, Co, Cr, and Si primarily degrade the mechanical characteristics. Silver's impact on Cu-Al-Mn alloys, though less explored, seems to augment the alloys magnetic attributes, microhardness, and precipitation kinetics. It also increases the temperature of martensitic and austenitic transformation in ternary systems. Further research is needed to fully understand the influence of silver and other microalloying elements on the properties of Cu-Al-Mn SMA alloys.

2.4.3. Ag addition in Cu-Al-Mn system

Research into the influence of silver on Cu-Al-Mn alloys is still in its early stages. In a study by Silva [10], the implications of silver addition on the magnetic characteristics of a Cu-11%wt. Al- 10%wt. Mn- 3%wt. Ag alloy were explored. The findings suggest that Ag-rich precipitates boost the relative proportion of Cu_2MnAl, leading to alterations in the alloy's magnetic properties after annealing. The reduced magnetic saturation was linked to a shift in the Cu_2AlMn phase fraction, which diminished when quenched in silver's presence. While manganese's addition impacted the alloy's phase stability range and microhardness, making the eutectoid reaction unnoticeable in annealed Cu-11% wt. Al samples, silver's presence didn't change the phase transformation sequence or microhardness in annealed Cu-11% wt. Al alloys. However, it did amplify the magnetic moment of the latter by roughly 2.7 times, slowing the eutectoid and peritectoid reactions in the former.

Santos [12] found out the silver the impact of bainite precipitation on microhardness in the Cu-based SMA alloys. Additionally, the manganese present reduced the solubility of silver in the alloy, favoring the emergence of Ag nanoprecipitates in as-quenched specimens. The

precipitation of a fraction of Ag retained in the matrix post-quenching only transpired following the emergence of τ_3-Cu_3AlMn_2, βMn, β_2 (B2), and α phases.

The prevailing studies on the influence of Ag in Cu-Al-Mn alloys indicate that Ag's inclusion can lead to shifts in the alloy's microstructure and phase stability domain. This can subsequently result in changes to its magnetic attributes and microhardness characteristics. Nevertheless, a comprehensive understanding of how Ag impacts the functional traits of Cu-Al-Mn alloys necessitates further in-depth investigation.

2.5. Other shape memory materials

After examining Cu-based SMA, the literature review is extended to other SMMs. In this section, a wider net is cast to cover a variety of other shape memory materials. Of, SMP, and SMH. The focus then shifts to SMC and SMG. SMc are mentioned to conclude this section.

2.5.1. Shape memory polymers (SMP)

From a technical standpoint, the properties of polymers are easier to adjust than those of metals and alloys [174]. Additionally, the cost of materials and processes for polymers is typically lower. Furthermore, SMP are lighter, have a higher recoverable strain than SMA, and can be stimulated to recover their shape by a variety of stimuli, including UV and infrared light, moisture, solvents, pH changes, and heat [175]. Many SMP are also biocompatible and biodegradable [176]. The adaptability in tweaking SMP allows for tailoring it to suit specific application needs. The underlying mechanism for the SME in SMP revolves around a two-segment or dual-domain structure. In this system, one segment retains its hard or elastic nature consistently, while the second segment's rigidity varies—being either malleable or stiff—based on external stimuli. Taking thermo responsive SMP as a case in point, the shift from the hard and rigid high-temperature austenite phase to the pliable and supple low-temperature martensite phase occurs progressively. This shift engages the liberation of stored elastic energy within the elastic domain. This operational principle stands in contrast to that of SMA.

Predominantly, SMPs are sensitive to temperature, showcasing either one-way or two-way SME capabilities. Earlier two-way SMPs were restricted to memorizing just a pair of shapes: a temporary one and its original form. Yet, innovative fabrication techniques have now enabled the creation of SMPs capable of recalling three or even more configurations by integrating SMPs possessing varied shape transition characteristics [177]. The unchanging form of SMP is set by its fixation segment, while the transient shape is steered by its switching segment [30]. When pitted against SMAs, SMPs present several advantages such as amplified deformability, biocompatibility, reduced weight, affordability, straightforward manufacturing, and modifiable rigidity [178]. Enhancing SMPs by incorporating elements like continuous fibers has led to marked improvements in their mechanical attributes. This has propelled a growing interest in SMPs and their associated composites in the recent past [30].

2.5.2. Shape memory hybrids (SMH)

The development of new SMM has been greatly enhanced by the concept of SMH [25, 30]. An SMH is composed of at least two components: an elastic component and a transition component. In the hybrid, the elastic segment consistently exhibits high elasticity, retaining elastic energy post-programming. Conversely, the transition segment has the capability to become pliable when its temperature surpasses the transition threshold. After cooling, it retains its reshaped form and solidifies. When the transition segment is reheated, the elastic segment discharges the stored elastic energy, enabling the hybrid to revert to its original shape [179, 180].

The mechanical properties and shape memory characteristics of the SMH can be predetermined by carefully selecting the components and the process for mixing them without significant chemical interaction. For example, the use of highly elastic silicone as the elastic component has led to the creation of rubbery SMH at both high and low temperatures [181]. However, in this case, the transition component was a hot melt adhesive with melting and crystallization temperatures of 70 °C and 55 °C, respectively, making the programming temperature for fixing the preliminary shape too high (at 37 °C) and the programming time window too short for fitting applications [180].

2.5.3. Shape memory ceramics (SMC)

SMC have a wide range of applications, such as high temperature actuators and ultra-high energy dissipation [18]. They offer several advantages over SMA, including better thermal stability, higher operating temperature, higher strength, and improved resistance to oxidation and corrosion [18]. While SMA, like NiTi, NiTi-TiPd, NiTiZr, and CuAlNi, have their own advantages, they can degrade at high temperatures due to factors such as creep, microstructure development, and oxidation [18].

Among the existing SMCs, zirconia-based ceramics stand out as the favored choice due to their capacity for mechanical-thermal actuation via a reversible martensitic phase transformation, similar to SMA [18, 47]. Other ceramics like multiferroic perovskites, such as bismuth ferrite ($BiFeO_3$), demonstrate shape memory characteristics through a similar reversible martensitic phase transformation, transitioning from rhombohedral to tetragonal in $BiFeO_3$ [18, 47]. However, their primary application hinges on their ferroelectric or piezoelectric properties, being activated by external thermal and electric fields [179]. Notably, fused silica glass, possessing an amorphous structure, undergoes strain recovery from volume changes induced by thermal treatment, distinguishing it from the martensitic phase transformation observed in SMA [18, 25, 30].

2.5.4. Shape memeory gels (SMG)

SMG are a new branch of soft and moist materials in materials science that have gained attention due to their unique properties such as high-water absorbency, softness, transparency, and low friction. These properties make SMG an interesting material for industrial applications, particularly in the medical field [182]. SMG are known for their ability to recover their original shape, a property referred to as shape recovery. At room temperature, SMG are mechanically tough and transparent, but upon heating to a specific temperature, they become soft and pliable, allowing them to be formed into any shape. When rapidly cooled, the deformed shape is retained, but when heated again to the specific temperature, the gel softens and resumes its original shape before solidifying once more upon cooling [183]. The potential applications of

SMG are varied, such as a bandage for broken bones, an optical lens, or a smart button in input devices [182, 183].

2.5.5. Shape memory composites (SMc)

SMc, which consist of at least one type of SMM, either SMA or SMP, as one of the components, can be easily handled by designers with a solid background and experience in the field if the properties of SMA/SMP are well understood [18, 25, 30, 179, 184]. The synthesis and development of SMP to meet the requirements of specific applications often require trial and error and a deep understanding of the material [184].

2.6. Commercial application of SMA alloys

Commercial utilization of SMA is classified based on distinct properties such as free recovery, constrained recovery, actuators, and SE. In terms of free recovery, SMAs demonstrate the capacity to deform during their martensitic state and revert to their initial shape upon heating above the transformation threshold, reclaiming the deformation strain. This thermoelasticity characteristic finds applications in devices like space antennas, eyeglass frames, blood clot filters, self-expanding stents, and devices for atrial septal defect occlusion [29, 185].

Constrained recovery, while still leveraging the thermoelastic feature, revolves around partial shape restoration. Here, the shape memory component doesn't achieve full recovery but is confined to a specific configuration, leading to stress accumulation. This stress production becomes the focal attribute in these materials' applications. Essentially, the shape memory component's recovery is intentionally obstructed to attain a targeted outcome. Such properties find relevance in aerospace, marine, and orthopedic sectors, particularly in fasteners and couplings [29, 186]. The category of actuators encompasses the deployment of SMA as integral elements within broader systems. Here, the shape memory component perceives and reacts according to a given situation, aligned with system demands. This mechanism entails both activation and the release of mechanical action, in tandem with its thermoelastic nature. Such

attributes are harnessed in devices like fire alarms, fire safety valves, deep fat fryers, and temperature-sensitive fuses [29, 187].

Lastly, SE represents the most commercially explored shape memory attribute. This property entails the SMAs' capability to endure significant elastic strains at designated temperatures. The fundamental principle here is the energy retention during stress application and the subsequent consistent stress release. Commercial applications capitalizing on SE include eyeglass frames, brassiere underwires, medical instruments, mobile phone antennas, and devices for orthodontic adjustments [29, 188].

Trends in research on SMA applications from 2005 to 2015 were mainly focus on the magnetocaloric and mechanocaloric effects [25, 189] that are related to energy conversion. The findings indicate that these areas of research occupy a significant percentage of the papers on SMAs during this time period, which is likely due to the growing demand for solutions to energy problems. However, conventional SMA are inadequate for practical applications that require extremely large cycle properties of transformation, particularly regarding the elastocaloric effect. Novel SMA that meet the demands of challenging field applications could be developed by employing alloy-design techniques, building on recent findings such as those involving Ti-Ni-Cu thin films [25, 190, 191]. SMAs have been widely studied as components in micro electro mechanical systems (MEMS), and the size effect on their properties has been reported by many investigators. For example, Gómez-Cortés et al. [191] found that the SE property of a micro pillar changes significantly when its diameter is smaller than 1.0 μm, and the critical stress follows a power law of diameter. Additionally, a single-crystalline micro pillar made of ZrO_2-based ceramic exhibits perfect SE [25, 192].

Other relevant issues in the field of SMA, such as strain glass, precise self-accommodation theory, and abnormally low Yang modulus in Fe- (noble metal) systems. In addition, an interesting application of an Fe-Mn-Si-based ferrous SMA as a damper material for an antiseismic system in buildings is noted, despite the fact that neither the SME nor the SE is used in the application. Overall, trends and recent developments in the field of shape memory alloys where focus on their potential for energy conversion and MEMS [25, 193-196].

Beyond the commonly recognized applications, the allure of Cu-SMA is amplifying due to their promise for operation at elevated temperatures compared to other SMA types. The phase transition energies inherent to these alloys make them ideal candidates for roles in energy and thermal capture materials, encompassing elastocaloric alloys. Beginning in 2015, a

significant utilization of Cu-SMA emerged in the domain of solid-state refrigeration through the elastocaloric effect (eC), leveraging the latent heat derived from the SE phase transition. When there's a primary phase shift from a structure with high symmetry (austenite) to one with lower symmetry (martensite), there's an entropy variation which entails either heat release or absorption. This culminates in a temperature shift that potentially facilitates cooling close to 10 K for Cu-centric alloys. The coefficient of performance (COP), which gauges the energy absorbed ΔH against the energy expended in the elastocaloric cycle, serves as an eC metric in SMA. In certain alloy instances, the eC efficacy aligns with the Carnot cycle for analogous thermal activities [5, 197, 198]. A visualization of the elastocaloric process, depicted in Figure 18., unveils its four phases: the mechanical stress application on the alloy to initiate direct martensitic conversion, the ensuing heat discharge during the transformation, the adiabatic release for facilitating the inverse transition and heat intake, and the final adiabatic shift to chill the setup.

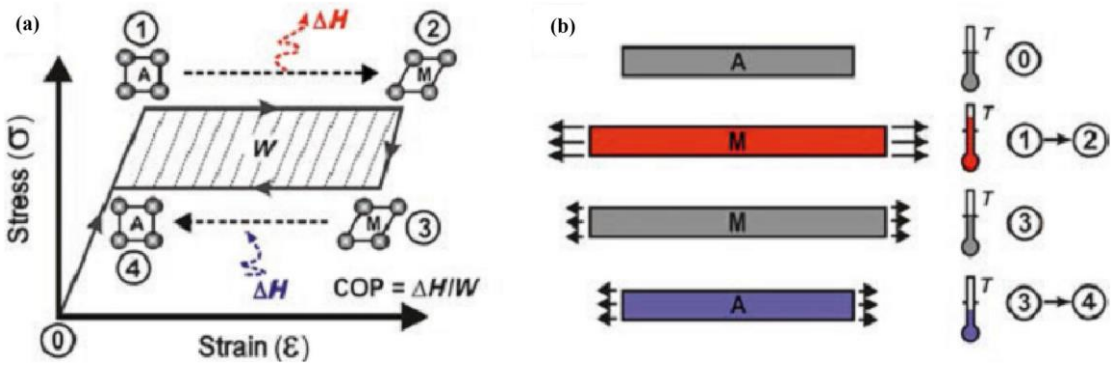

Figure 18. *The elastocaloric SMA cycle described as follows:(a) The cycle consists of four stages during the loading and unloading of a superelastic material. Specifically, between steps 1 and 2, the latent heat of transformation is emitted, whereas between steps 3 and 4, this heat is absorbed. (b) This is visualized in terms of the thermal impact across the elastocaloric stages. [5, 199]*

Many prototypes have been developed to optimize efficiency with the cooling capacity of eC superelastic SMA, while other research groups focus on developing and studying new elastocaloric alloys to improve the latent heat of the martensitic transformation. The theoretical temperature change is determined by the entropy change, and a higher entropy change indicates a better cooling capacity, but in practice, hysteresis and plastic deformation during the

thermoelastic martensite transformation impair the full reversibility of the phase transformation [5, 197, 200–208].

The pioneering eC discovery was noted in a Cu–Zn–Al single crystal, as reported by a study [171]. Several other studies have confirmed promising eCs in the Cu–Al–Zn alloy system [202, 207]. However, there are still unresolved issues, such as grasping the thermoelastic transformation in Cu-based SMAs, deciphering the energies inherent in this transformation, understanding microstructural effects, determining the impact of plastic deformation, and bridging the gap between theoretical and observed temperature shifts during an elastocaloric cycle. For elastocaloric applications, scientists are employing computational strategies to refine alloy compositions. In-depth discussions on the thermodynamics associated with eCs can be referenced in specific literature [5, 103-105, 201, 209, 210].

The interest in Cu-based SMA has been driven by the emergence of new processing methods, compositions, and technological applications. Additive manufacturing, severe plastic deformation, and functionally graded materials are potential areas for future investigation in the fabrication of Cu-based SMA. Additionally, the development of novel compositions can be approached through alloying, advances in manufacturing processes, and machine learning methods. For energy applications, Cu-based SMA have shown potential for use in elastocaloric cooling, but the challenge remains to optimize their composition and microstructure to maximize transformation energies without compromising functionality. Despite the progress made in this area, the functional damage after thermal or stress cycles remains a limiting factor for their application.

2.7. Thermodynamic modeling of multiphase metal systems (CALPHAD method)

In order to accurately describe and characterize the behavior of SMA materials, it is necessary to develop a relevant phenomenological, theoretical model. This approach has been studied since the 1980s and the chosen model depends on the intended purpose of the model. For engineering design purposes, a macroscopic model rooted in mesomechanics is most appropriate. In order to implement the model into finite element code, constitutive relations of the SMA model are specified in an incremental form. Research in materials science reveals that the distinctive behavior of SMA materials is due to thermoelastic martensitic transformation, and that hysteresis loops suggest phase transitions don't typically achieve

complete thermodynamic equilibrium states. This implies that a framework grounded in continuum, nonequilibrium thermodynamics is apt for constructing a macroscopic SMA behavior model. In the traditional approach of equilibrium, continuum thermodynamics, the principle of local state defines the thermodynamic state of a local volume, known as a representative volume element (RVE), in relation to external conditions like stress and temperature. This RVE is perceived as a unified thermodynamic entity, its continuum characteristics and state progression arising from mean properties and states of its microelements. The RVE's scale is contingent upon the modeling's focus, with metallic materials often having a size of a few tenths of a millimeter [211].

In order to extend classical thermodynamics to nonequilibrium processes, a theory called thermodynamics with internal state variables (ISV) has been developed. ISV theory enables a unique definition of the thermodynamic state of a representative volume element (RVE) undergoing irreversible processes, such as constrained thermodynamic equilibrium states. ISV are introduced to capture macroscopic effects connected with micro- and mesostructural evolution of RVE arrangement without the need to follow complex mesoscopic details. The values of internal state parameters, also called hidden parameters, can only be changed indirectly through variations in external state parameters such as stress or temperature [211].

In the ISV framework, the Helmholtz free energy or the Gibbs free enthalpy function is characterized by an expanded set of both external and ISV pertinent to specific physical contexts. From the nonequilibrium thermodynamics formalism with ISV, the derived constitutive relationships fall into two categories: state equations stemming from the chosen thermodynamic potential form, and kinetics associations that outline ISV evolution. These kinetics associations connect ISV fluxes to related thermodynamic drivers and are articulated as interlinked, rate-based, ordinary differential equations. To ensure compliance with the second law of thermodynamics during dissipative events, the ISV evolution equations must adhere to certain criteria. Leveraging the ISV theory provides significant benefits compared to other modeling techniques. Even though direct control over ISV is not possible, they usually carry a distinct physical meaning, and their quantifiable values are ascertainable from experimental data analysis. This facilitates tracking the ISV evolution trajectory, supporting the validation of hypothesized kinetics ties in ISV progression. Modern computational capabilities, paired with advancements in the finite element method, position ISV theory as an

optimal choice for addressing nonlinear boundary challenges through incremental digital approaches [211].

Given the intricate nature of SMA materials, this phenomenological modeling discussion confines itself to the temperature and stress domains where SMA displays SE characteristics. Nevertheless, components are introduced and deliberated upon that might pave the way for broadening the model's predictive scope to cooler temperatures, encompassing both SE and SME descriptions [50-211].

Understanding the states of materials in relation to temperature, pressure, and component concentrations necessitates the use of phase diagrams. These diagrams are pivotal in materials science for tasks such as alloy creation, processing, development, and comprehensive understanding. Two-component materials typically utilize binary phase diagrams, whereas ternary systems call for a third dimension to fully represent them. Representing ternary systems often involves using projections or sectional views. Visual representation becomes more complex for systems having more than three components due to a combination of limited experimental data and the intricacies of multiple dimensions. However, with advances in computational technology and modeling, computer simulations for phase equilibria in multicomponent systems are now feasible [212].

Over a hundred years ago, J.W. Gibbs established the mathematical framework connecting thermodynamics and phase equilibria. J.J. van Laar developed imaginary binary systems and introduced concentration-dependent factors to characterize solution phases, terms later dubbed regular solutions by Hildebrand. J.L. Meijering pioneered the calculation of miscibility voids in ternary and quaternary solutions and utilized this approach for thermodynamic scrutiny of the Cr-Cu-Ni system. In their exploration of the Fe-Ni system's martensitic transformation, Kaufman and Cohen utilized thermodynamic computations and expanded their research to include the calculation of phase diagrams, integrating pressure variability. Through their consolidated insights on the phase diagram computations and the provision of computer program directories for binary and ternary phase diagram calculations, Kaufman and Bernstein laid the groundwork for the CALPHAD method [212]. In examining a multicomponent system, as illustrated in Figure 19., it typically starts by formulating thermodynamic characterizations of the integral binary systems.

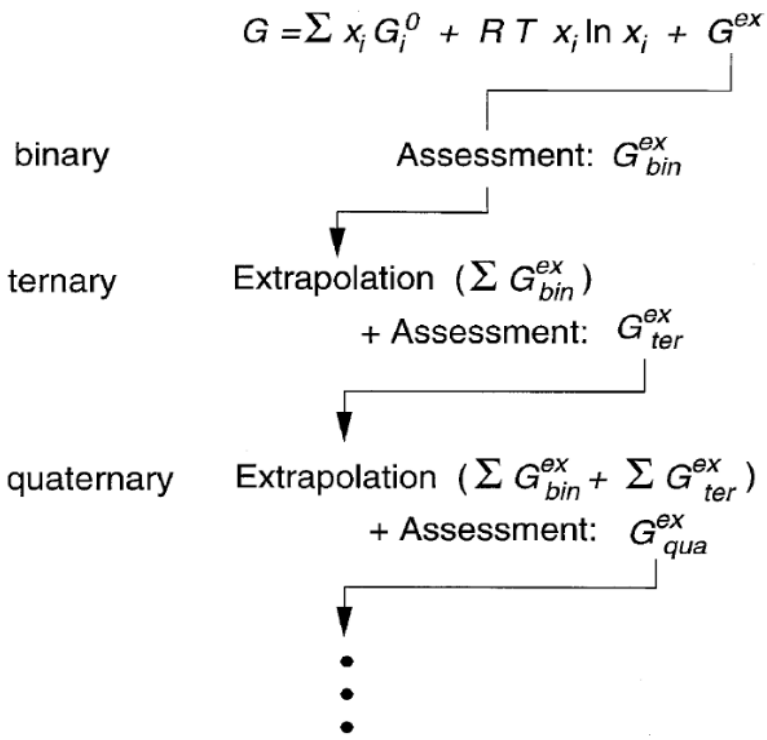

Figure 19. *To project into systems with a higher number of components, the surplus Gibbs energies of the foundational subsystems are evaluated employing the CALPHAD approach. [212]*

Subsequent steps involve the application of thermodynamic extrapolation techniques to extend the thermodynamic functions from binary systems to ternary and even more complex systems. Critical experiments are designed based on these extrapolated results, and a comparison is made between the experimental outcomes and the extrapolation. To enhance the thermodynamic description of more complex systems, interaction functions are introduced when needed, optimizing their coefficients using experimental data. This iterative process continues until all the component systems within an n-component framework are examined. However, it's often observed that most systems require minimal to no corrections for accurate predictions of systems with four or more components, since genuine quaternary phases in metallic systems are infrequent. As a result, a thorough examination of the majority of the ternary subsystems often suffices for describing an n-component system [212].

The computational technique known as the CALPHAD method, aimed at predicting phase diagrams, has witnessed consistent expansion since its establishment in the 1970s. Kikuchi introduced an approach to manage order/disorder phenomena, later termed the cluster variation method, which is now frequently combined with first-principles computations.

Despite the significant computational demands of these calculations, there have been substantial advancements in algorithms and computational capabilities in recent times. While the predicted phase diagrams are generally correct in topology, they sometimes lack the precision needed for hands-on applications [212].

The complexity of multicomponent systems poses a challenge for representing phase-diagram information, but various methods have been developed to overcome this issue. Approximations like expressing compositions of elements as equivalents can simplify the representation, but they are limited to specific composition regimes. The term “alloy design” after the phase computation (PHACOMP method) uses the electron hole number theory to predict detrimental phases in superalloys, but it requires special corrections for other alloy families.

The CALPHAD approach, which operates on the principle of minimizing a system's free energy, is versatile, expandable, and rooted in theoretical foundations. Experimentally deriving phase diagrams can be both expensive and time-intensive. However, phase diagram calculations can streamline the process to identify equilibrium conditions. Data from numerical phase diagrams aids various other modeling pursuits, including nitriding/carburizing, diffusion pairing, precipitate dissolution, and solidification. Beyond just determining the existing phases and their compositions, phase-equilibrium calculations can also yield numerical data on enthalpy, temperature, and the concentration-driven shifts of phase boundaries. This supports the integration of microscopic and macroscopic models. Over the years, the emphasis has shifted from merely calculating phase diagrams to computational thermodynamics, recognizing that phase diagrams represent only a fraction of the insights gleaned from such computations [212].

The objective of the CALPHAD collective is to curate consistent thermodynamic data for systems ranging from binary to quaternary. Advanced computing capabilities have enabled the incorporation of more intricate models for complex systems. The latest phase diagram evaluations align impressively with experimental findings and serve as foundations for modeling and extending into systems of higher complexity. However, earlier evaluations might not always gel with recent ones due to evolving model descriptions. Even so, there has been notable advancement in recent times, leading to a surge in available databases tailored for multi-component systems [212].

3. EXPERIMENTAL PART

This chapter provides detailed descriptions of the materials and methods used for the investigations.

3.1. Materials

Ternary Cu-Al-Ag and quaternary Cu-Al-Mn-Ag alloys were prepared from pure metals with high purity: copper (Cu) 99.9%, aluminum (Al) 99.5%, manganese (Mn) 99.8%, and silver with 99.99%. Metals were supplied by MaTecK Material-Technologie & Kristalle, Jülich, Germany. Design compositions of investigated alloys are shown in Table 1. and 2.

Table 1. *Compositions of Cu-Al-Mn-Ag SMA alloys*

Sample NO.	**Chemical composition, (wt%, Cu Bal.)**
1	Cu-9Al-7Mn-2Ag
2	Cu-9Al-7Mn-5Ag
3	Cu-9Al-7Mn-7Ag
4	Cu-9Al-16Mn-2Ag
5	Cu-9Al-16Mn-5Ag
6	Cu-9Al-16Mn-7Ag
7	Cu-9Al-10Mn-2Ag
8	Cu-9Al-10Mn-5Ag
9	Cu-9Al-10Mn-7Ag
10	Cu-9Al-10Mn-8Ag

Table 2. *Compositions of Cu-Al-Ag SMA alloys*

Sample NO.	**Chemical composition, (wt%, Cu Bal.)**
1	Cu-10Al-1Ag
2	Cu-10Al-2Ag
3	Cu-10Al-5Ag
4	Cu-10Al-7Ag
5	Cu-10Al-20Ag

3.2. Processing of Cu-based SMA alloys

The processing of the designed Cu-Al-Mn-Ag and Cu-Al-Ag SMA alloys were produced by melting and casting in electric arc furnace under argon atmosphere, followed by two 15-minute vacuum cycles. To achieve better homogenization, the alloys were remelted four times before being cast in cylindrical molds with a diameter of 8 mm and a length of 12 mm (Fig. 20.).

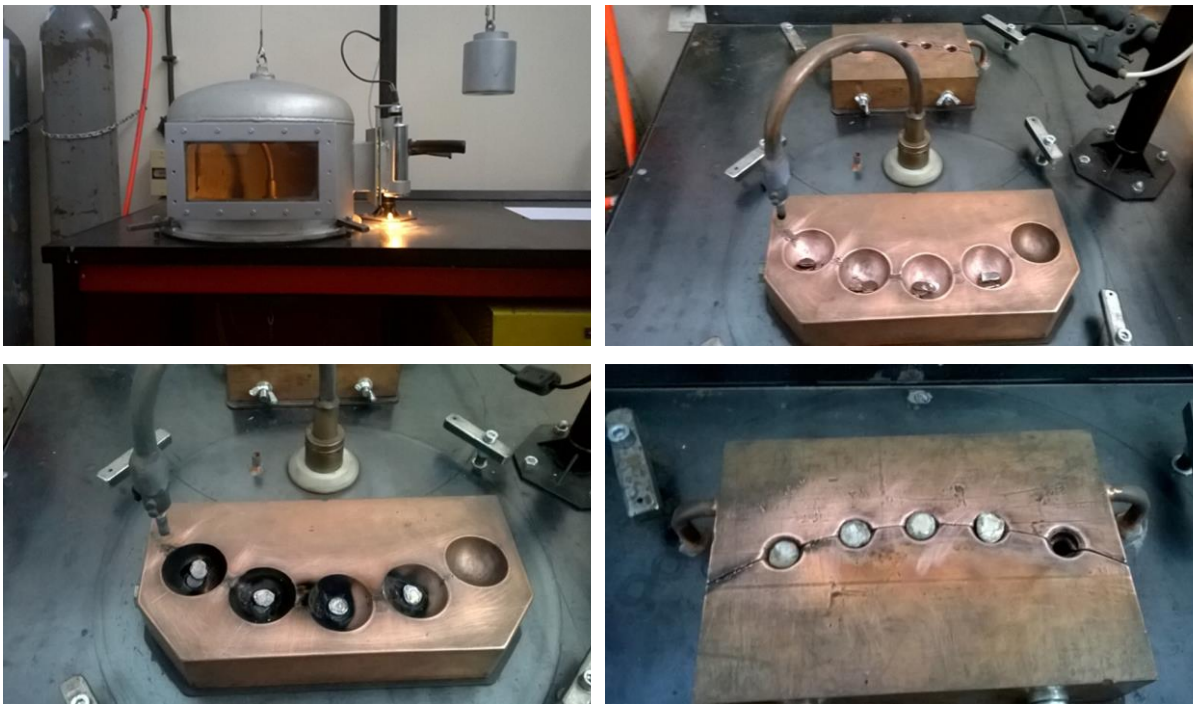

Figure 20. *Processing of ingots in the electric arc furnace*

Heat treatment of as-casted Cu-SMA alloys was conducted in OVER chamber furnaces at 900 °C for 30 minutes, and quenched in water (Fig. 21.).

Figure 21. *OVER furnaces for heat treatment of SMA alloys*

3.3. Metallographic preparation

Samples for metallographic preparation were hot mounted by Struers Citopress 20 machine in hard polymer mass. Prepared samples where then ground with 320#, 600#, 800#, and 1200# SiC abrasives papers, followed by polishing steps with 1µm and 0,25µm diamond pastes at Struers Tegramin-30 machine (Fig. 22.). To visualize the microstructure, the prepared samples were etched with 2.5 g $FeCl_3$/48 ml CH_3OH/10 ml H_2O solution.

Figure 22. *Struers Citopress 20 and Tegramin-30 machine for metallographic preparation*

3.4. Thermodynamic modelling

Thermodynamic calculation of the ternary systems Cu-Al-Mn was performed using the Thermo-Calc (TCW) software, applying the CALPHAD method, based on calculations of the minimum of Gibbs free energy for each component and each phase in the system.

Commercial databases SSOL 6 is used for thermodynamic calculations in defined parameters of composition, pressure, temperature and phase. Calculations were done with database for Cu-Al-Mn ternary system, based on binary subsystems Cu-Al, Cu-Mn, and Al-Mn system and optimized parameters for ternary alloy in Cu-rich region, according to Miettinen [213].

3.5. Characterization methods

3.5.1. Optical microscopy (OM)

Microstructure investigation of the alloys were studied using an Axio Vert A1 OM with the AxioCam ERc 5s microscope module, seen at Figure 23. The microstructure was analyzed using brightfield (BF) and polarized (POL) light at various magnifications, including 50x, 100x, 200x, 500x, and 1000x for all samples in this thesis.

Figure 23. *Axio Vert A1 optical microscope*

3.5.2. Scanning electron microscopy (SEM-EDS)

Scanning electron microscope FEG quanta 250 FEI SEM, fitted with an OXFORD EDS, seen in Figure 24., was used for microstructure investigation of ternary and quaternary samples. Samples were subjected to a beam energy of 20 kV under high and ultra-low vacuum pressures. Micrographs were captured at various magnifications, including 200x, 1500x, 2500x, 5000x, and 10000x, using both the Everhart-Thornley Detector (ETD) and the Large Field Detector (LFD), while, chemical composition was determined by energy dispersion X-ray spectroscopy detector.

Figure 24. *FEG quanta 250 FEI SEM*

3.5.3. Electron backscatter diffraction analysis (EBSD)

EBSD studies were performed utilizing a ZEISS Supra 25 SEM, as illustrated in Figure 25. The SEM operated under an acceleration voltage of 15 kV, maintained a working distance of 17 mm, employed a tilt angle of 70°, and had step sizes varying from 0.4 to 0.06 μm. For EBSD analysis, sample preparation followed established metallographic procedures, which encompassed mechanical grinding with SiC papers, refining with diamond pastes, and culminated in a 1-hour polishing phase using 0.04 μm colloidal silica.

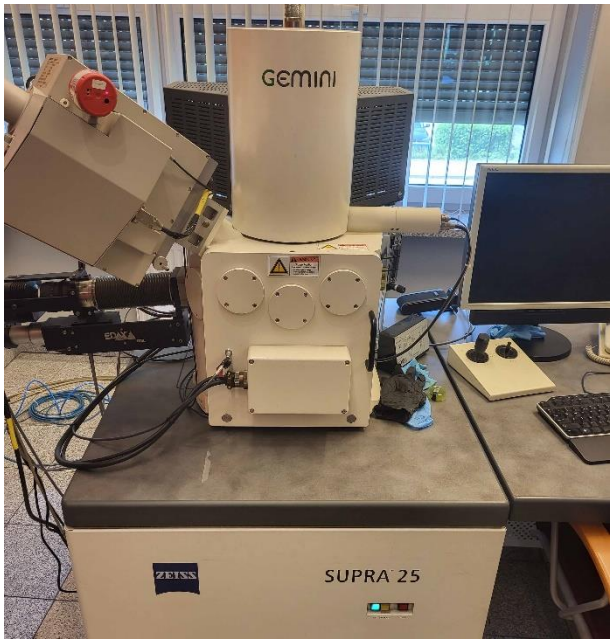

Figure 25. *Supra 25 FE-SEM equipped with EBSD detector*

3.5.4. X-ray diffraction analyses (XRD)

Phase detection was performed on a Rigaku MiniFlex 600 Advance diffractometer using CuKα radiation (Fig. 26.). The samples were placed in a suitable carrier and subjected to analysis with an accelerating voltage of 40 kV and a current of 25 mA in the range of 15-80 °2θ with a step of 0.02 °2θ and dwell times of 0.6 seconds. The sample preparation process took 2 minutes in air.

Figure 26. *Rigaku MiniFlex 600 diffractometer*

High-energy XRD assessments of the crystal structure and overall texture of samples, were conducted at DESY in Hamburg, Germany, utilizing the P07B beamline (87.1 keV, λ= 0.0142342 nm), seen in Figure 27. The diffraction patterns for phase analysis were captured in a continuous mode with a 2D Mar345 Image Plate detector. To ensure a texture-neutral measurement, samples underwent a 180° rotation about the ω-axis during the X-ray process. To meet the Bragg condition for all offshoot reflections, a continuous rotation around the ω sample axis by $\omega < \pm 10°$ was performed. A beam size of 1×1 mm^2 was used. The 2D patterns acquired were then integrated through the Fit2D Version 18 (beta) software and showcased in a graph depicting relative intensity against the 2Theta angle [216].

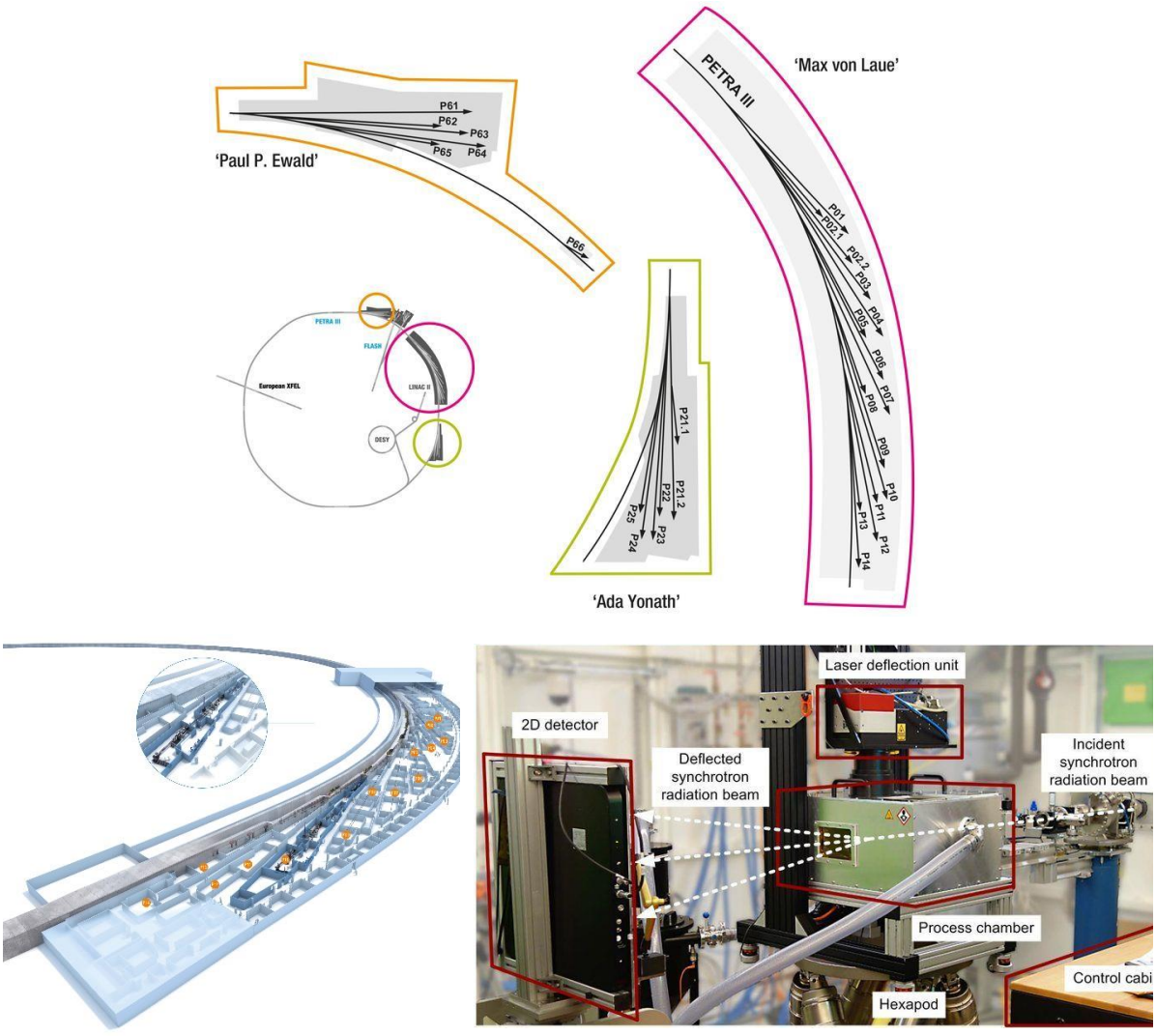

Figure 27. *P07B beamline at DESY*

The atomic order determination involved calculating the intensity ratio of I_{hkl}/I_{220}, using reflections from the predominant phase—up to 900°C from austenite and subsequently from martensite [216].

3.5.5. Transmission electron microscopy (TEM)

The Tecnai G2 F20 (200 kV) TEM was employed to obtain Selected Area Diffraction Pattern (SADP), as well as bright and dark field images. This microscope boasts features like an Energy Dispersive X-ray Microanalyzer (EDX), a High-Angle Annular Dark Field (HAADF) detector optimized for Scanning Transmission Electron Microscopy (STEM) applications, a Field Emission Gun (FEG), and high-resolution Gatan UltraScan along with wide-angle SIS Megaview cameras. An image of this microscope is illustrated in Figure 28. [216].

Figure 28. *Tecnai G2 F20 TEM*

Focused ion beam (FIB) cut lamellas (approx. 10 × 8 µm) for investigation were prepared using Helios 650HP SEM/FIB Dual Beam microscope (Thermo Fisher Scientific, previously FEl Company) with Octane Pro EDS detector (EDAX Inc.).

3.5.6. Differential scanning calorimetry (DSC)

Transformation temperatures were determined using a modular DSC Mettler-Toledo 822e model for the low temperature (Fig. 29.). Dynamic measurements were performed by 2 heating/cooling measurement cycles in the temperature range from -100 °C to 250 °C in nitrogen atmosphere, with a heating/cooling rate of 10 K min^{-1} for quaternary Cu-Al-Mn-Ag samples. Ternary Cu-Al-Ag samples were measured in the temperature range from -50 °C to 350 °C with a heating/cooling rate of 10 K min^{-1}. Cooling role was controlled by liquid nitrogen. Samples mass were around 100 mg [216].

Figure 29. *Mettler-Toledo 822e MDSC*

3.5.7. Microhardness

The microhardness of the samples was determined using a fully automated microhardness measuring system FM-ARS -9000 (Fig. 30.). The parameters for the hardness test were determined with a load of 100 g and a dwell time of 15 seconds. Prior to the microhardness measurements, each sample surface was subjected to a thorough preparation process that included careful cleaning, grinding and polishing to ensure the accuracy of the

results. Vickers microhardness values were calculated as the average of five individual measurements of each sample [216].

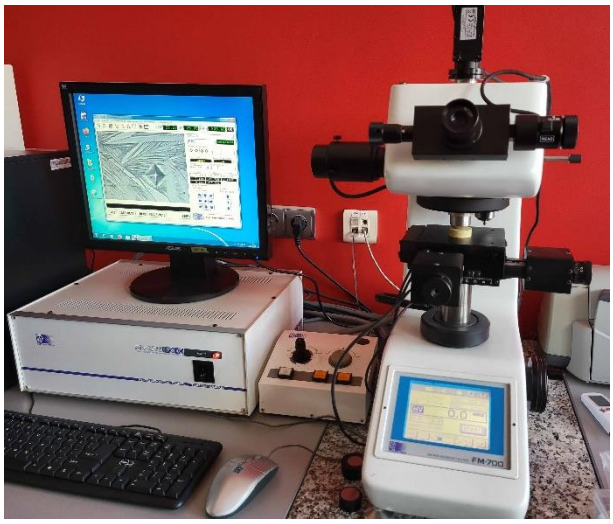

Figure 30. *FM-ARS -9000 Micro Vickers Tester.*

4. RESULTS AND DISCUSSION

In this chapter, the results systematically present empirical findings from a range of advanced characterization techniques. The overview of the results is divided into quaternary Cu-Al-Mn-Ag and ternary Cu-Al-Ag SMA systems. Each study begins with optical microscopy, providing an initial insight into the microstructure of the material. The study moves to a more detailed analysis using scanning electron microscopy, which reveals profound morphologies. X-ray and high-energy X-ray diffraction measurements delve into the crystalline structures of the material, while transmission electron microscopy allows an examination of the material's nanoscale intricacies. Differential scanning calorimetry provides information on thermal behavior and phase transformations. The section concludes with the test of mechanical properties (hardness). Together, these results provide a comprehensive understanding of the properties and behavior of the material.

4.1. Quaternary Cu-Al-Mn-Ag SMA alloys

4.1.1. Thermodynamic modelling

Based on calculations using the prepared database for the Cu-(9-10) Al-10Mn system, a vertical section of the phase diagram for 9% Mn was obtained, as shown in Figure 31.

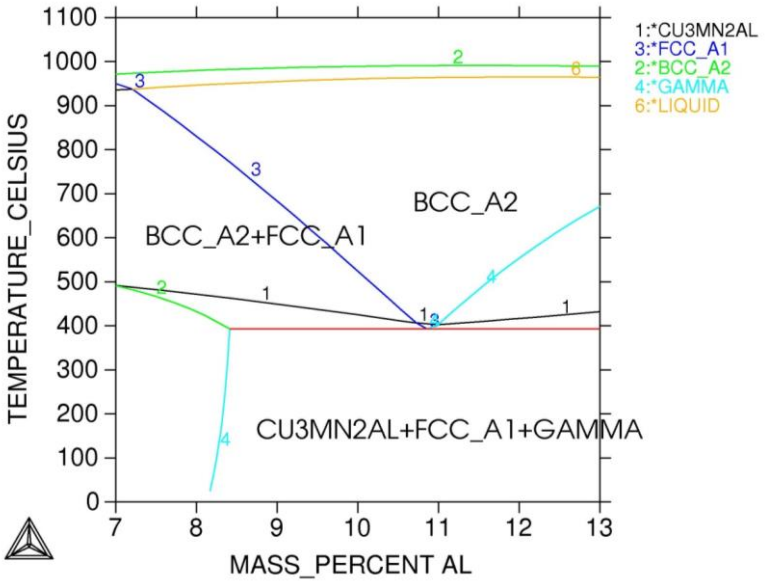

Figure 31. *Calculation of the Cu-9Al-10Mn system with optimized parameters for the ternary Cu-Al-Mn system according to Miettinen [213]*

The diagram reveals the high-temperature β phase region for 9% wt. Al content, from which a metastable martensitic structure forms upon rapid cooling. Under equilibrium conditions and due to slow solidification at a temperature of 390 °C, eutectoid decomposition of the beta phase into alpha and gamma phases occurs, as well as the precipitation of the τ_3 phase, a ternary phase with composition Cu_3Mn_2Al. This last phase, τ_3, cannot be determined using the commercial SSOL database, based on data for binary subsystems used in the table 3. presents the phases considered in the calculation for Cu-rich region of the ternary Cu-Al-Mn system with thermodynamic phase descriptions.

Based on calculations prepared with a database for the Cu-9Al-10Mn system, a vertical section of the phase diagram for 10%Mn is shown on Figure 31. The diagram clearly shows the high temperature beta phase region for Al contents of 9% wt., from which a metastable martensitic structure forms upon rapid cooling. Under equilibrium conditions and due to slow solidification at a temperature of 390 °C, eutectoid decomposition of the β phase into α and γ phases occurs, as well as precipitation of the τ_3 phase, a ternary phase, Cu_3Mn_2Al. This last phase, τ_3, cannot be determined with the commercial SSOL database. With rapid cooling from the β' phase in non-equilibrium conditions martensite phase occurs.

Table 3. *Calculated phases from Cu-9Al-10Mn system, a vertical section of the phase diagram for 10% wt. Mn*

Phase/Temperature range	**TD database name**	**Pearson's mark**	**Space group**	**Lattice parameters [pm]**
Liquid	L	-	-	-
α (fcc (Cu)) < 1083	FCC_A1	cF4	Fm3m	a = 361.48
β 1049-761	BCC_ A2	cI2	Im3m	a = 294.6
γ < 873	GAMMA	cF4	P43m	a = 871.32
cbcc (αMn) < 710	CBCC_A12	cI58	I43m	a = 891.39
τ_3 < 550	Cu_3Mn_2Al	cF24	Fd3m	a = 690.46

The table 3. gives an overview of the phases considered in the calculation for this region of the Cu-Al-Mn ternary system, with the thermodynamic names of the phases in the Thermo-Calc program and the basic parameters.

4.1.2. Microstructure investigations

Figure 32. presents OM micrographs of the as-cast Cu-9Al-16Mn-2Ag SMA using both bright field and polarized light techniques. The microstructure exhibits a dual-phase morphology, as α + β phase, with martensite's slender needles appearing at the grain boundaries. Post solution treatment and subsequent quenching, there's a transformation in morphology, revealing a fully developed martensite structure with diverse orientations within the grains, as shown in Figure 33. A notable reduction in grain size is evident in the quenched Cu-9Al-16Mn-2Ag alloy. Factors such as temperature, duration, and the cooling environment, all part of the thermal stabilization parameters, influence this grain size [216]. Depending on factors like chemical compositions, the e/a ratio, and chosen thermal stabilization techniques, Cu-Al-Mn alloys can exhibit dual martensite structures, β_1' (18R) and γ_1' (2H), during the heat-activated thermoelastic martensite transformation [211].

As structural order enhances, there's a stabilization of more γ_1'-martensite compared to β_1'-martensite. However, the structure order is the propelling factor for martensite that is more pronounced for the nucleation of 2H-type martensite. Both martensite types share many similarities, yet their morphological differences arise from distinct modes of non-uniform shear. Originating from the $L2_1$ (Heusler) phase, the β_1' (18R)-martensite has a stacking sequence of AB'CB'CA'CA'BA'BC'BC'AC'AB'. On the other hand, γ_1'-martensite typically emerges with higher aluminum concentrations, specifically exceeding 13 at%.

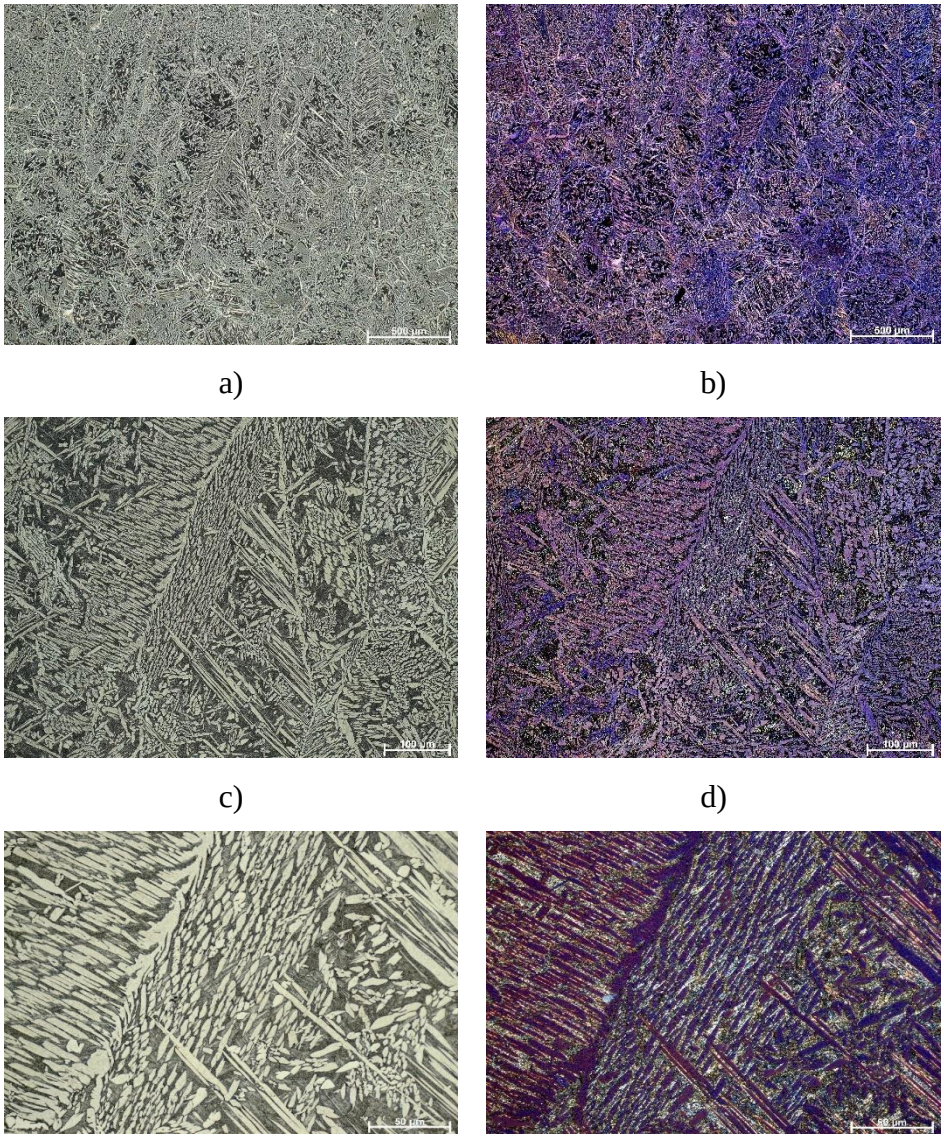

Figure 32. *OM micrographs of as-cast Cu-9Al-16Mn-2Ag SMA alloy: a) BF, mag. 100x, b) POL, mag 100x, c) BF, mag. 200x, d) POL, mag. 200x, e) BF, mag. 500x, f) POL, mag. 500x.*

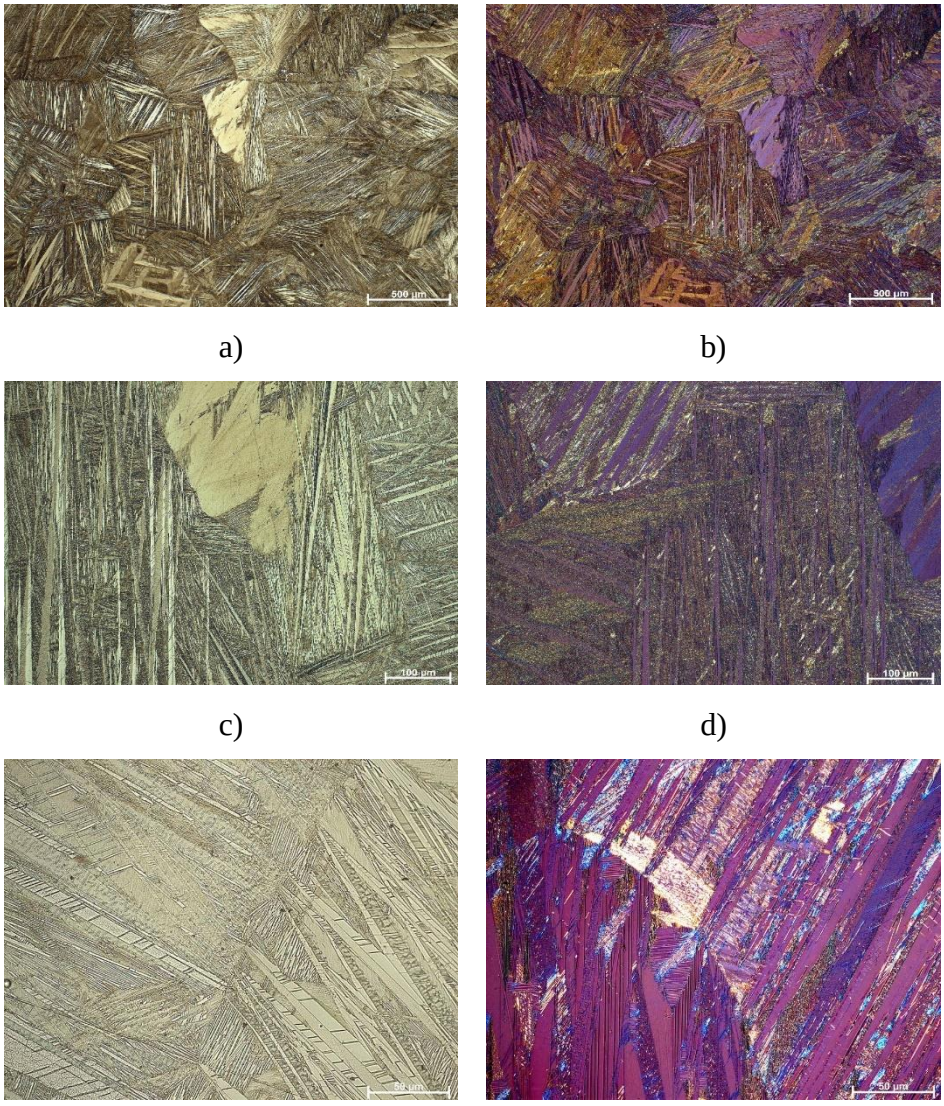

Figure 33. *OM micrographs of quenched Cu-9Al-16Mn-2Ag SMA alloy: a) BF, mag. 50x, b) POL, mag 50x, c) BF, mag. 200x, d) POL, mag. 200x,* e) BF, mag. 500x, f) POL, mag. 500x,

SEM images depict the initiation and growth of martensite plates at varied locations. These micrographs also illustrate the early phases of needle development between α-precipitates in the as-cast alloy (Fig. 34. a,c).

SEM investigations of the samples under study revealed a thorough transformation from austenite to martensite upon quenching, with no α-phase precipitation evident (as illustrated in Fig. 34. b, d). The predominantly spear-like morphology of martensite observed in the quenched alloy points to the β_1' martensite, characterized by a monoclinic structure. A zig-zag configuration of the β_1'-martensite is also discernible in areas (Fig. 34. d). Additionally,

the quenched alloy containing 16% wt. manganese showcases some broad martensite plates (Fig. 34. d). This may hint at the presence of minimal quantities of another martensite variant, γ_1', with an orthorhombic structure, but this should be determined through XRD analyses. The pattern of martensite is influenced by nucleation mechanisms and growth-related kinetics. It's acknowledged that the expansion of martensite plates during thermoelastic martensitic transformation is a gradual process, and new plate creation only happens when the expansion of current ones is hindered by grain boundaries [211]. β_1'-martensite needles display heightened thermoelastic behavior, which is linked to regulated expansion within self-accommodating groups.

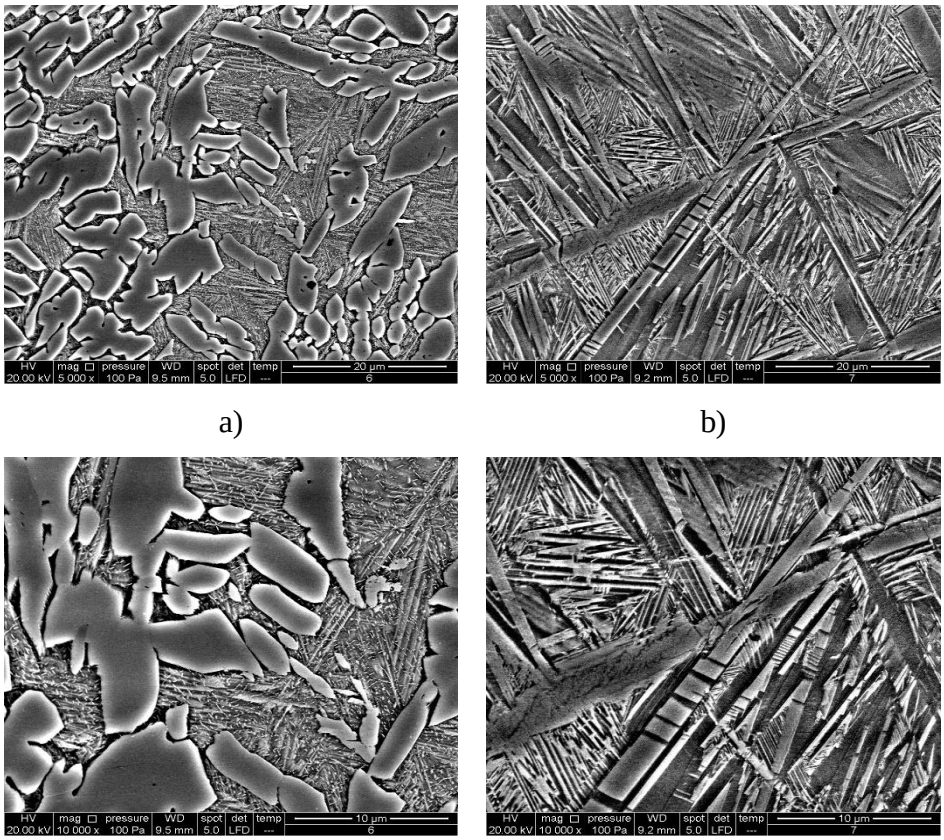

Figure 34. *SEM micrograph of Cu-9Al-16Mn-2Ag SMA alloy, mag. 5000x: a) As-cast state, b) Quenched state, and mag. 10000x: c) As-cast state, d) Quenched state*

In Figure 35., BS images, band contrast, and phase maps are presented for the as-cast Cu-9Al-16Mn-2Ag alloy, with the f.c.c.-Cu-phase (α-phase) precipitates highlighted in green. The quenched alloy is mainly characterized by spear-like forms in the β_1'-martensite plate group, as seen in Figure 35. e,f.). EBSD evaluations expose diverse patterns within microregions, corresponding to habit variants of the 18R martensite.

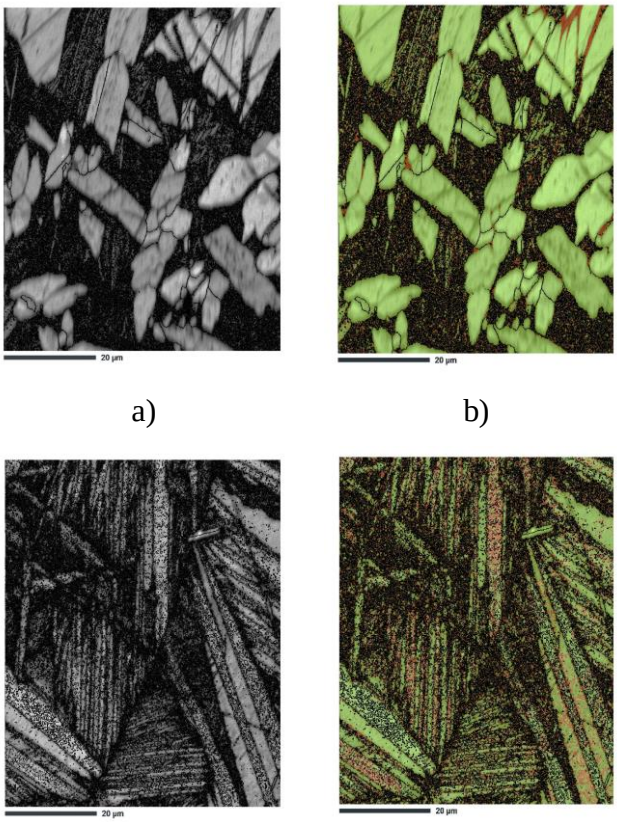

Figure 35. *Results of EBSD measurements: (a) band contrast image, (b) phase map for Cu9Al16Mn2Ag alloy in the as-cast state; (c) band contrast image, (d) phase map for Cu9Al16Mn2Ag alloy in the quenched state*

Complete martensitic structures in the alloy with reduced 7% wt. manganese content are illustrated in Figures 36. and 37., in both as-cast and quenched state. In the as-cast sample it can be observed some of parent phase, f.c.c. Cu. The quenched state demonstrates a denser martensite formation through twinning, evident in Figure 38. EDS examinations indicate consistent compositions across the martensitic matrix for the Cu-9Al-7Mn-2Ag alloy in both cast (Fig.39.) and quenched (Fig. 40.) states. In addition, the EBSD results (Fig. 41) confirm earlier observations at OM and SEM that the α-parent phase (f.c.c. Cu) is present in the martensite matrix in the as-cast state.

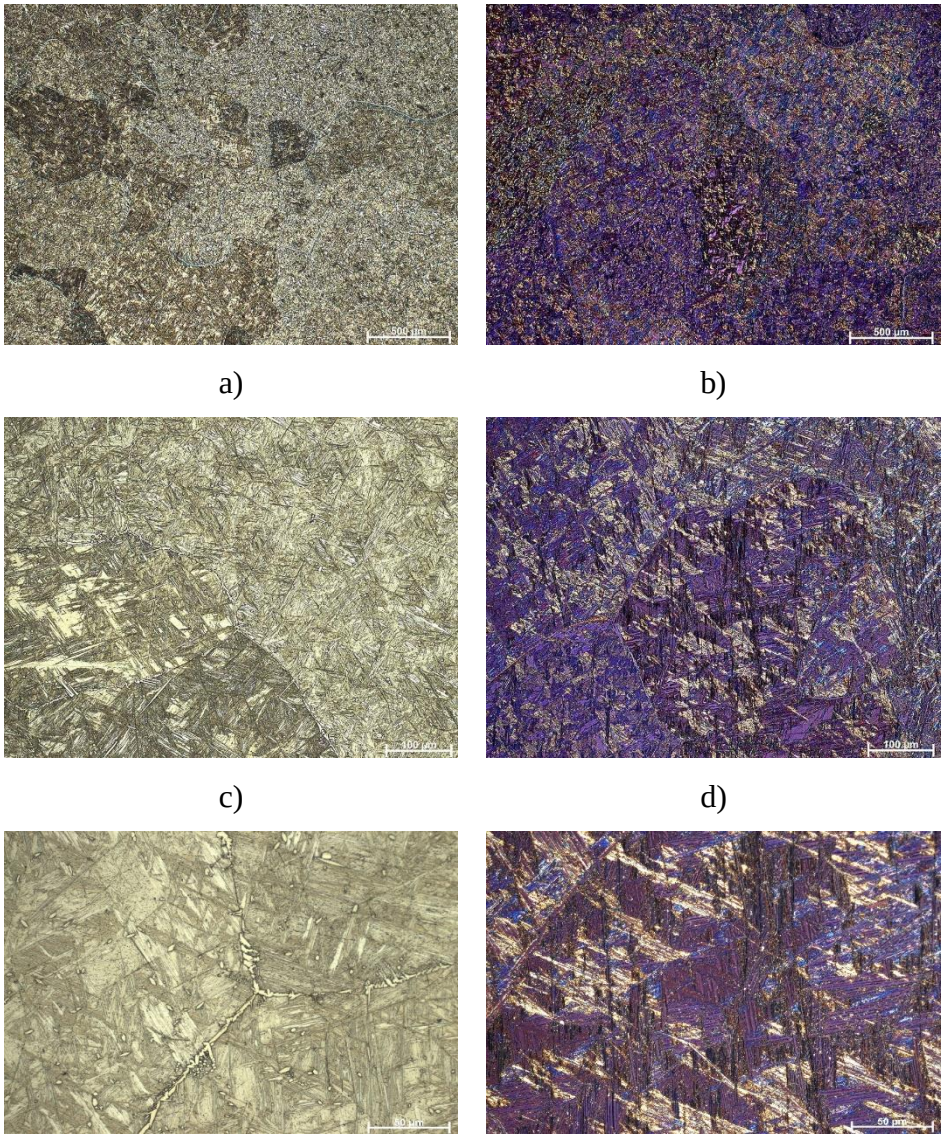

Figure 36. *OM micrographs of as-cast Cu-9Al-7Mn-2Ag SMA alloy: a) BF, mag. 50x, b) POL, mag 50x, c) BF, mag. 200x, d) POL, mag. 200x, e) BF, mag. 500x, f) POL, mag. 500x,*

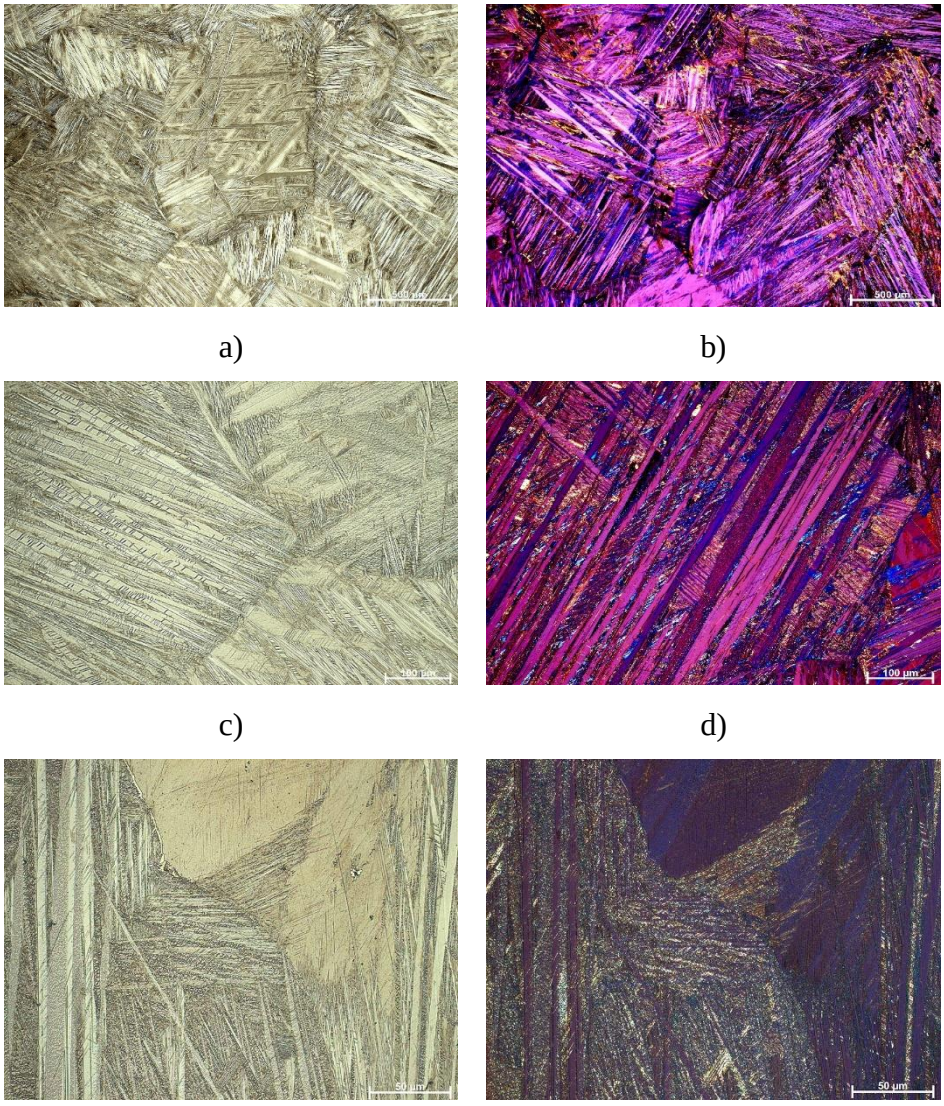

Figure 37. *OM micrographs of quenched Cu-9Al-7Mn-2Ag SMA alloy: a) BF, mag. 50x, b) POL, mag 50x, c) BF, mag. 200x, d) POL, mag. 200x, e) BF, mag. 500x, f) POL, mag. 500x,*

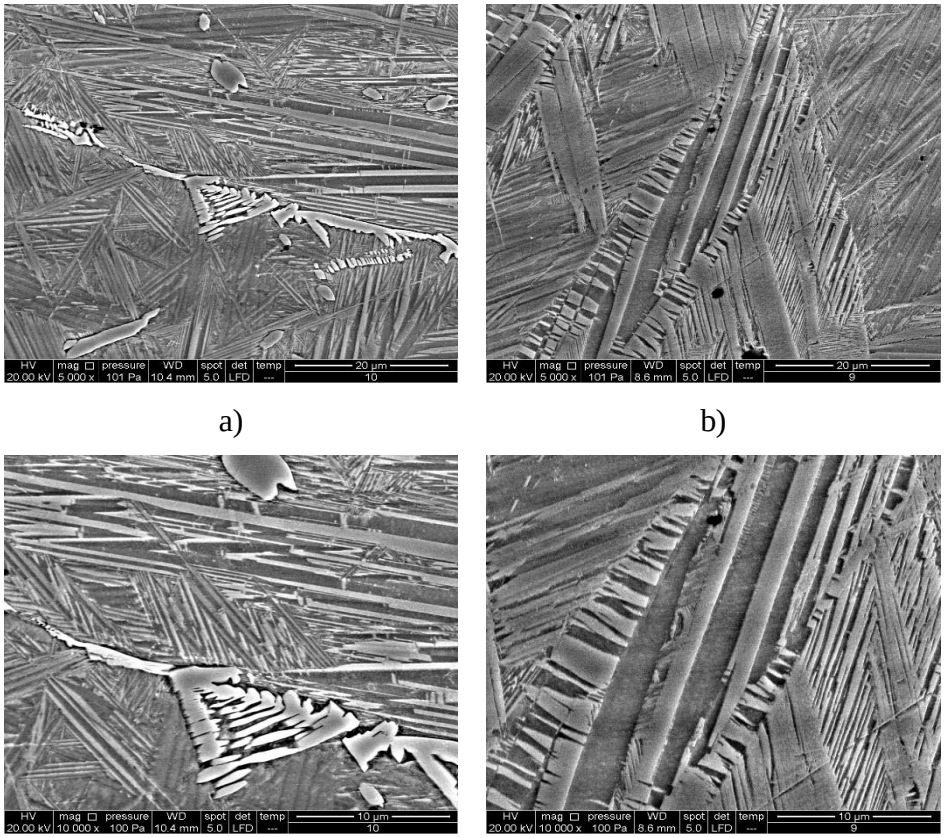

Figure 38. *SEM micrograph of Cu-9Al-7Mn-2Ag SMA alloy, mag. 5000x: a) As-cast state, b) Quenched state, and mag. 10000x: c) As-cast state, d) Quenched state*

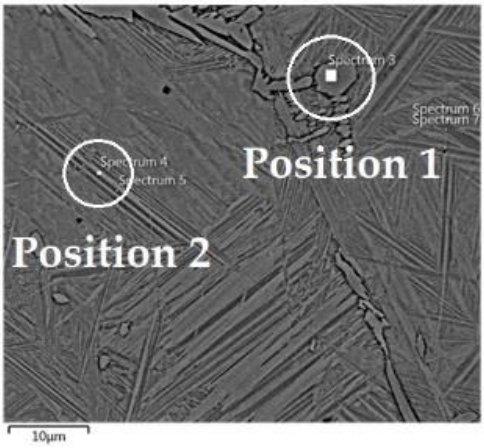

Element	Position 1 (wt.%)	Position 2 (wt.%)
Al	8.33 ±0.20	9.75 ±0.30
Mn	6.56 ±0.18	6.89 ±0.25
Cu	81.29 ±0.55	79.81 ±0.78
Ag	1.86 ±0.20	1.96 ±0.29

Figure 39. *EDS analysis of as-cast Cu-9Al-7Mn-2Ag alloy*

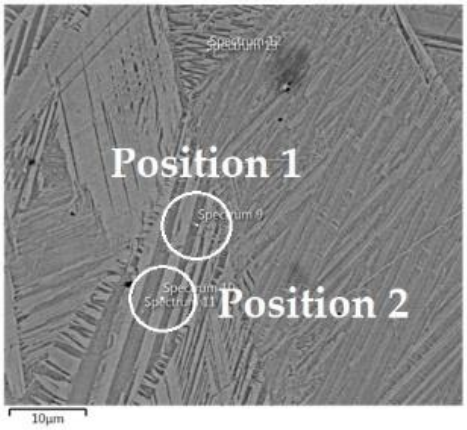

Element	Position 1 (wt.%)	Position 2 (wt.%)
Al	8.36 ± 0.39	8.27 ± 0.62
Mn	6.38 ± 0.34	6.27 ± 0.57
Cu	80.10 ± 1.14	82.49 ± 0.97
Ag	1.80 ± 0.39	2.98 ± 0.61

Figure 40. *EDS analysis of quenched Cu-9Al-7Mn-2Ag alloy*

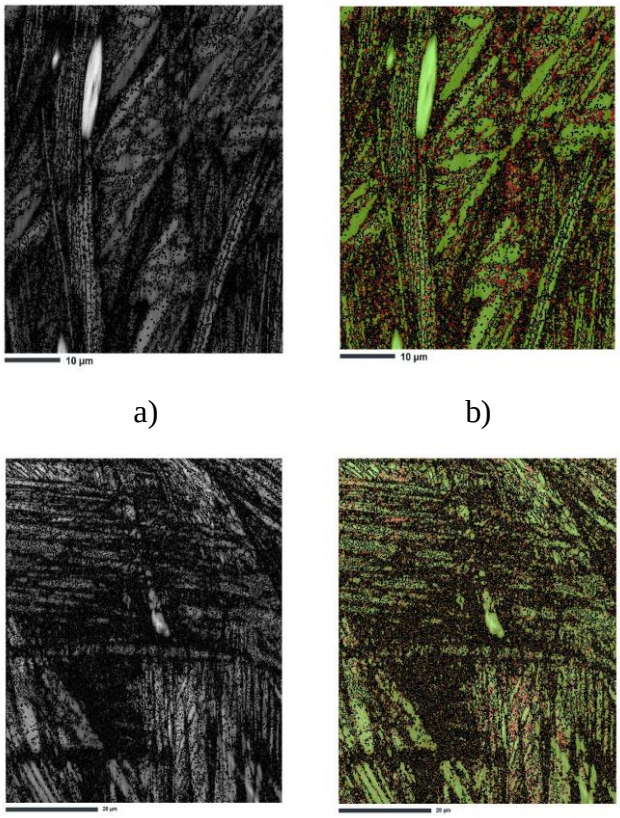

Figure 41. *Results of EBSD measurements: (a) band contrast image, (b) phase map for Cu9Al7Mn2Ag alloy in the as-cast state; (c) band contrast image, (d) phase map for Cu9Al7Mn2Ag alloy in the quenched state.*

Figure 42. and 43. show optical micrographs for higher concentrations of silver, Cu-9Al-7Mn-5Ag SMA alloy. It can be observed the most intense martensite morphology in the as-cast state and especially in the quenched state for all investigated quaternary SMA alloys.

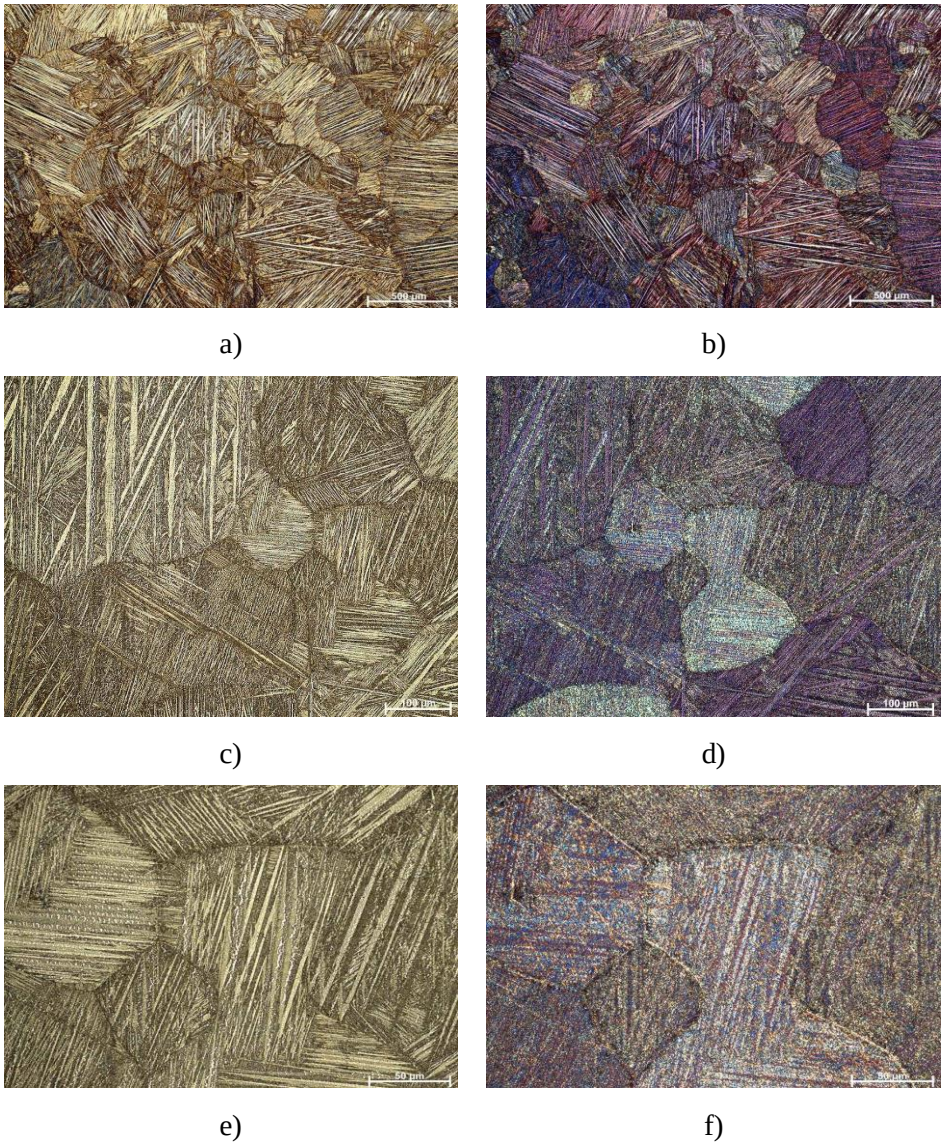

Figure 42. *OM micrographs of as-cast Cu-9Al-7Mn-5Ag SMA alloy: a) BF, mag. 50x, b) POL, mag 50x, c) BF, mag. 200x, d) POL, mag. 200x, e) BF, mag. 500x, f) POL, mag. 500x*

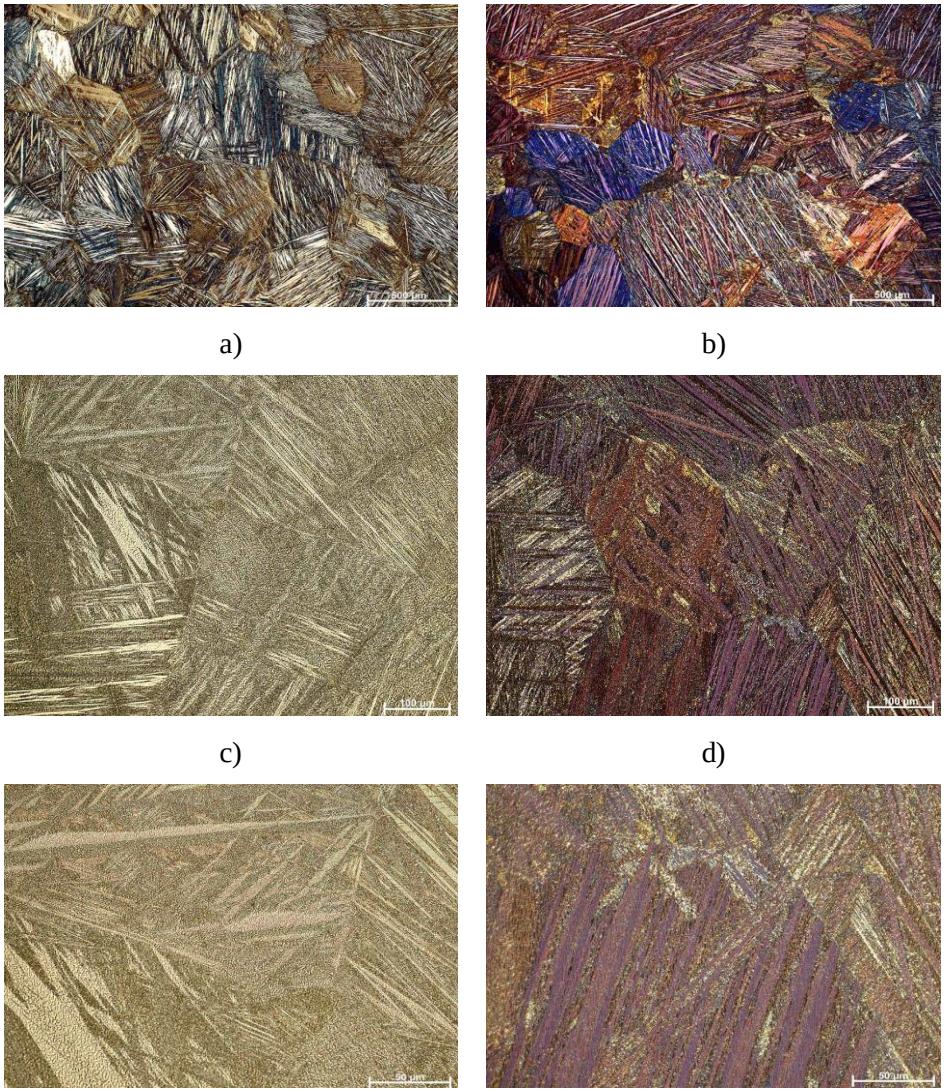

Figure 43. *OM micrographs of quenched Cu-9Al-7Mn-5Ag SMA alloy: a) BF, mag. 50x, b) POL, mag 50x, c) BF, mag. 200x, d) POL, mag. 200x, e) BF, mag. 500x, f) POL, mag. 500x*

SEM micrographs (Fig. 44.) show the presence of V-type martensite β_1' 18R, but the plates are drastically intense after quenching. As- cast specimens show precipitates of pure silver (Fig. 44. a,c), which are found inside the grains and were significant of the grain boundaries. After quenching, the same precipitations can be seen in martensite pates with EDS examinations across the martensitic matrix (Fig. 44.).

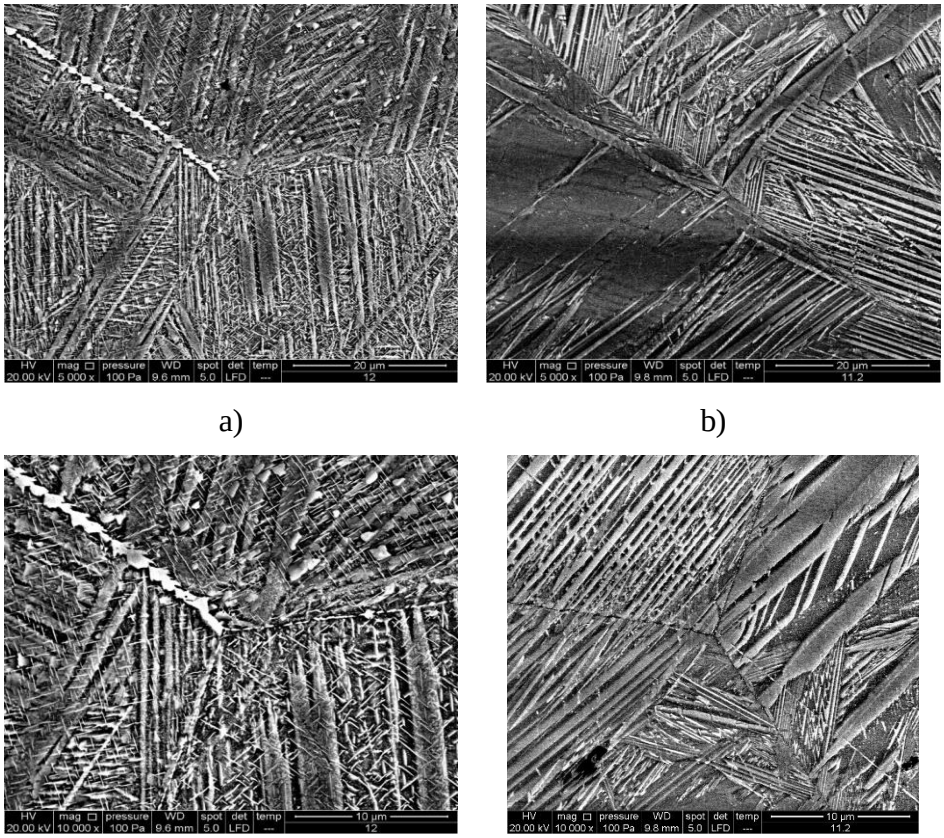

Figure 44. *SEM micrograph of Cu-9Al-7Mn-5Ag SMA alloy, mag. 5000x: a) As-cast state, b) Quenched state, and mag. 10000x: c) As-cast state, d) Quenched state*

The EBSD analysis of the Cu-9Al-7Mn-5Ag alloy in Figure 45. shows similar contrast and phase maps to the Cu-9Al-7Mn-2Ag alloy. However, there is a clearer martensite morphology and less heavily strained regions and phase boundaries, indicating a more stable martensite formation threw structure.

In contrast to the above Cu- SMA alloys, alloys with 10% wt. manganese and different silver compositions do not show a formation of martensite structure after quenching (Figs. 46-53.). OM micrographs Cu-9Al-10Mn-2Ag SMA alloy show some small pieces of forced martensite plates and long, elevated grains that differ from other Cu-9Al-10Mn-xAg samples (Fig. 46.). It can be seen that the grain size significantly decreases at a silver content of 7% wt. (Fig. 48.).

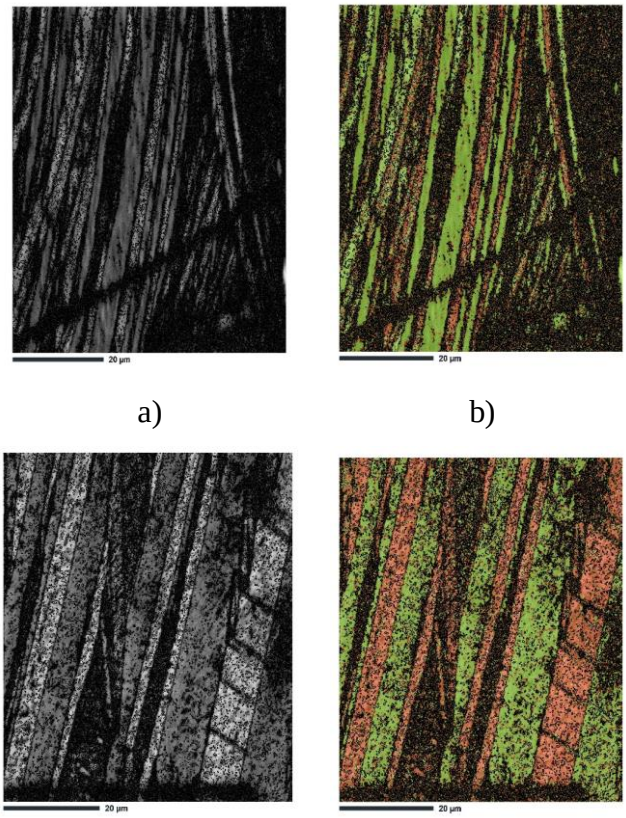

a) b)

c) d)

Figure 45. *Results of EBSD measurements for the Cu9Al7Mn5Ag alloy: a) band contrast image, b) phase map in the as-cast state, and c) band contrast image, d) phase map in the quenched state.*

a) b)

Figure 46. *OM micrographs of quenched Cu-9Al-10Mn-2Ag SMA alloy: a) BF, mag. 50x, b) POL, mag 50x*

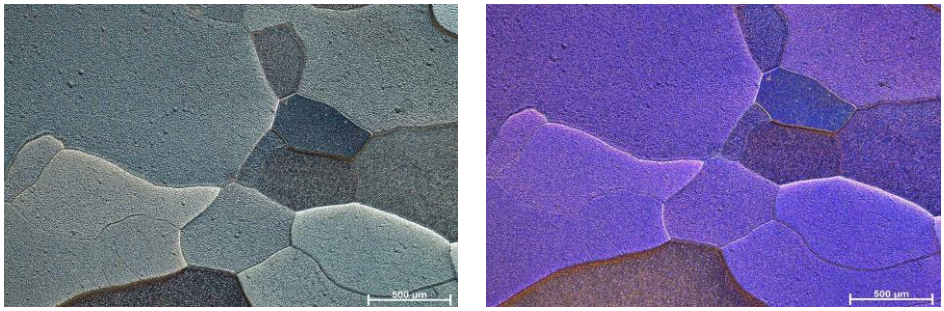

a) b)

Figure 47. *OM micrographs of quenched Cu-9Al-10Mn-5Ag SMA alloy: a) BF, mag. 50x, b) POL, mag 50x*

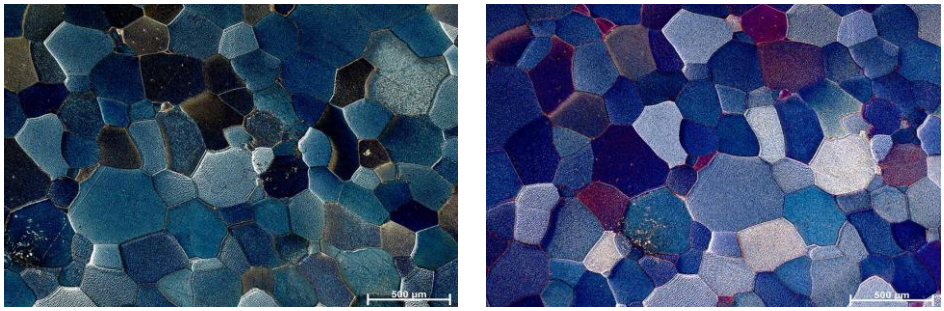

a) b)

Figure 48. *OM micrographs of quenched Cu-9Al-10Mn-7Ag SMA alloy: a) BF, mag. 50x, b) POL, mag 50x*

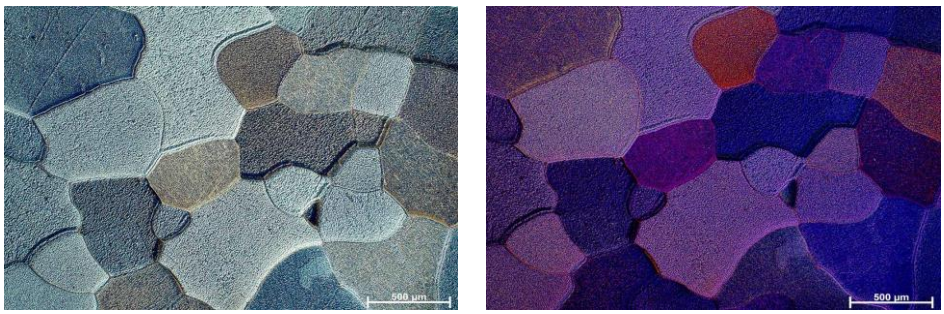

a) b)

Figure 49. *OM micrographs of quenched Cu-9Al-10Mn-8Ag SMA alloy: a) BF, mag. 50x, b) POL, mag 50x*

SEM micrographs (Figs. 50-53.) show a predominantly austenitic phase in Cu-9Al-10Mn-xAg SMA alloys, with some light silver precipitates in quenched Cu-9Al-10Mn-5Ag and Cu-9Al-10Mn-8Ag SMA alloys. It is not entirely clear why Cu alloys with 10% wt. Mn do not have a martensitic structure, but the absence of martensite after heat treatment could indicate that the M_s temperature of those SMA alloys is at much lower temperatures, below room temperature.

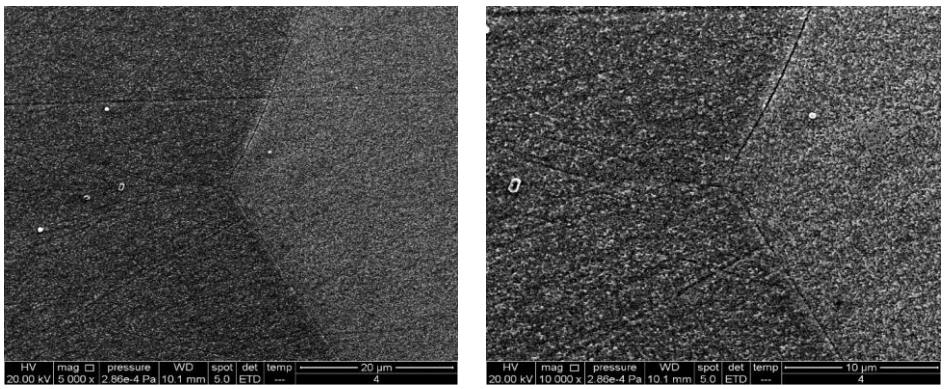

a) b)

Figure 50. *SEM micrograph of quenched Cu-9Al-10Mn-2Ag SMA alloy: a) mag. 5000x, b) mag. 10000x.*

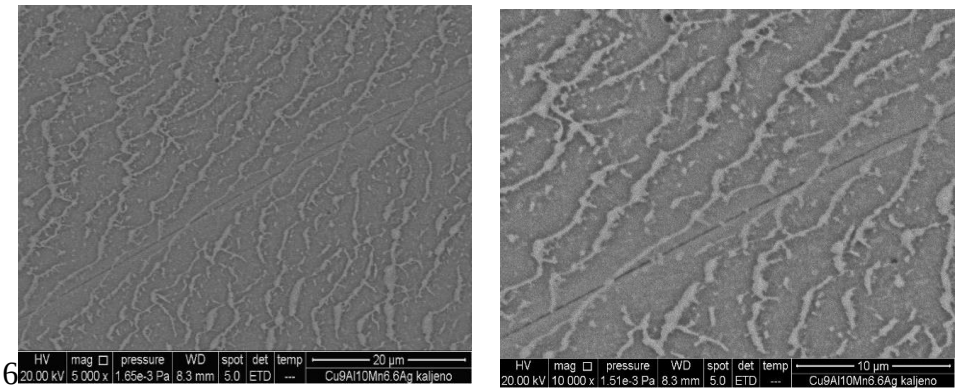

6

a) b)

Figure 51. *SEM micrograph of quenched Cu-9Al-10Mn-5Ag SMA alloy: a) mag. 5000x, b) mag. 10000x*

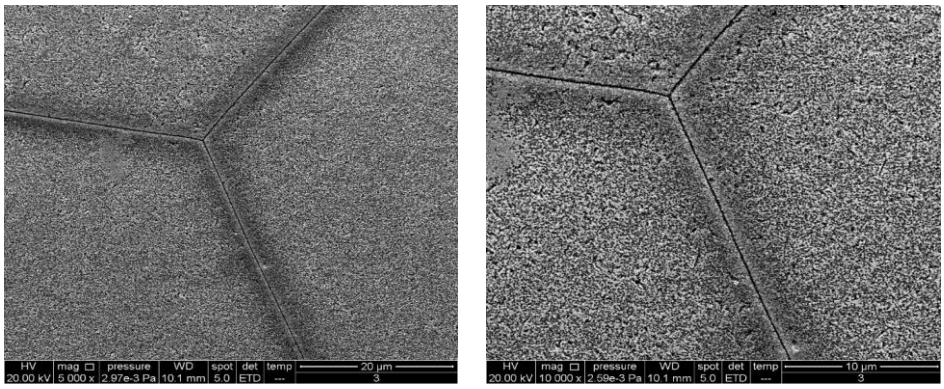

a) b)

Figure 52. *SEM micrograph of quenched Cu-9Al-10Mn-7Ag SMA alloy: a) mag. 5000x, b) mag. 10000x.*

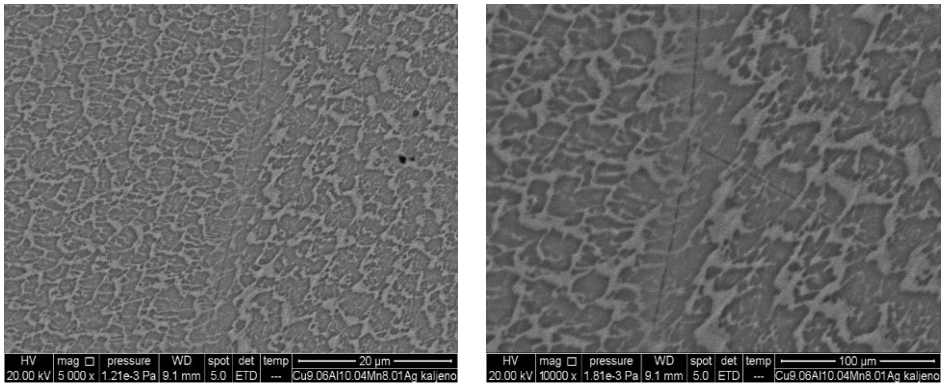

a) b)

Figure 53. *SEM micrograph of quenched Cu-9Al-10Mn-8Ag SMA alloy: a) mag. 5000x, and b) mag. 10000x*

After microstructure investigations, the quaternary SMA alloys Cu-9Al-16Mn-5Ag, Cu-9Al-16Mn-7Ag, and Cu-9Al-7Mn-7Ag showed a completely non-homogeneous microstructure.

4.1.3. X-ray diffraction analysis (XRD)

Both results confirmed results of OM and SEM results and coexistence of two martensite types in the quenched Cu-9Al-16Mn-2Ag alloy, β_1' (18R) monoclinic and γ_1' (2H) orthorhombic structures (Fig. 54). XRD results also confirmed precipitates of α-phase (f.c.c. Cu) and two-phase morphology in as-cast samples. Before heat treatment martensite is only partially formed, but it was detected β_1' and γ_1' martensite in the structure.

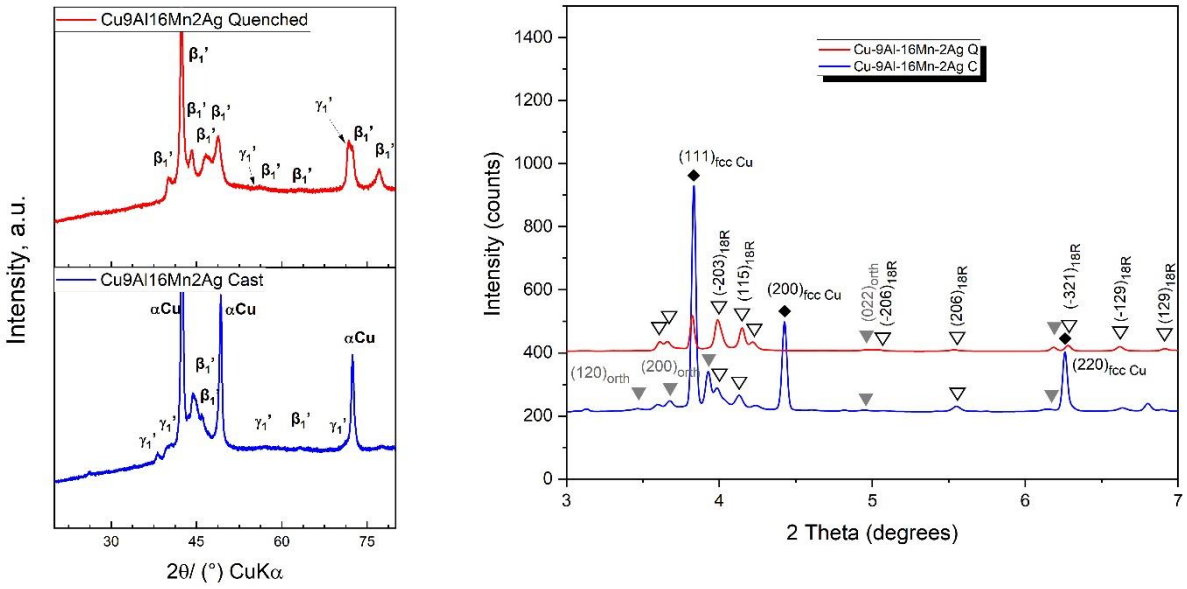

a) b)

Figure 54. *XRD diffractogram of Cu-9Al-16Mn-2Ag SMA alloy: a) regular XRD diffractogram, b) high-energy X-ray diffraction measurements from synchrotron*

Only one martensite type, β_1'(18R) is confirmed in Cu-9Al-7Mn-2Ag alloy (Fig. 55.). For the as-cast version of the alloy, pronounced α-phase (f.c.c. Cu) peaks emerge, suggesting the existence of Cu precipitation.

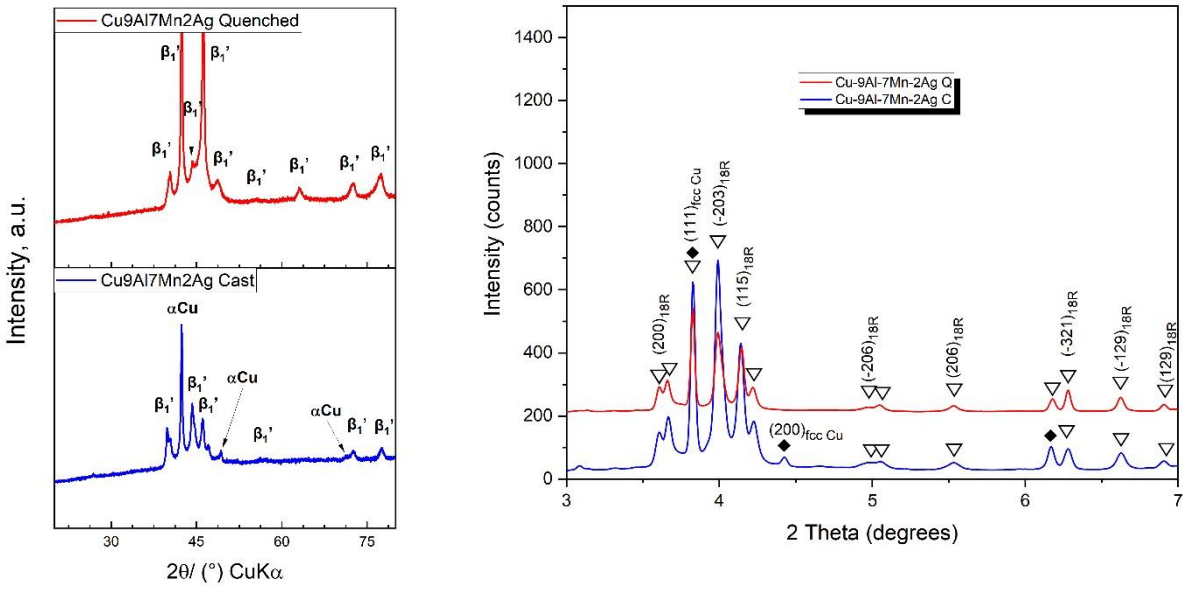

a) b)

Figure 55. *XRD diffractogram of Cu-9Al-7Mn-2Ag SMA alloy: a) regular XRD diffractogram, b) high-energy X-ray diffraction measurements from synchrotron*

Same composition of aluminum and manganese, but with higher silver content, Cu-9Al-7Mn-5Ag SMA alloy, shows precipitates of pure silver in the as-cast sample (Fig. 56.), what is not detected in other Cu-SMA alloys, with 16 and 7% wt. of manganese. In both states, as-cast and quenched, it is confirmed β_1' (18R) martensite.

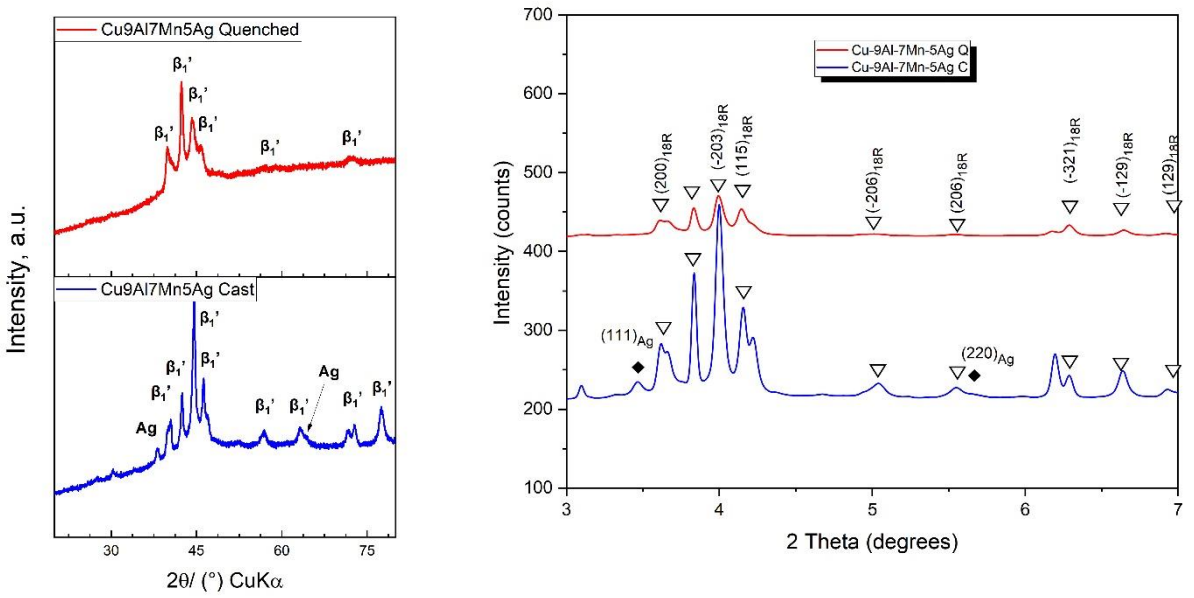

a) b)

Figure 56. *XRD diffractogram of Cu-9Al-7Mn-5Ag SMA alloy: a) regular XRD diffractogram, b) high-energy X-ray diffraction measurements from synchrotron*

XRD results for Cu-SMA alloys with 9% wt. of Al and 10% wt. of Mn, confirmed only austenite phase in all samples, both as-cast and quenched, with some of silver precipitates in samples with 5 and 7% wt. of silver (Figs. 57.-59.).

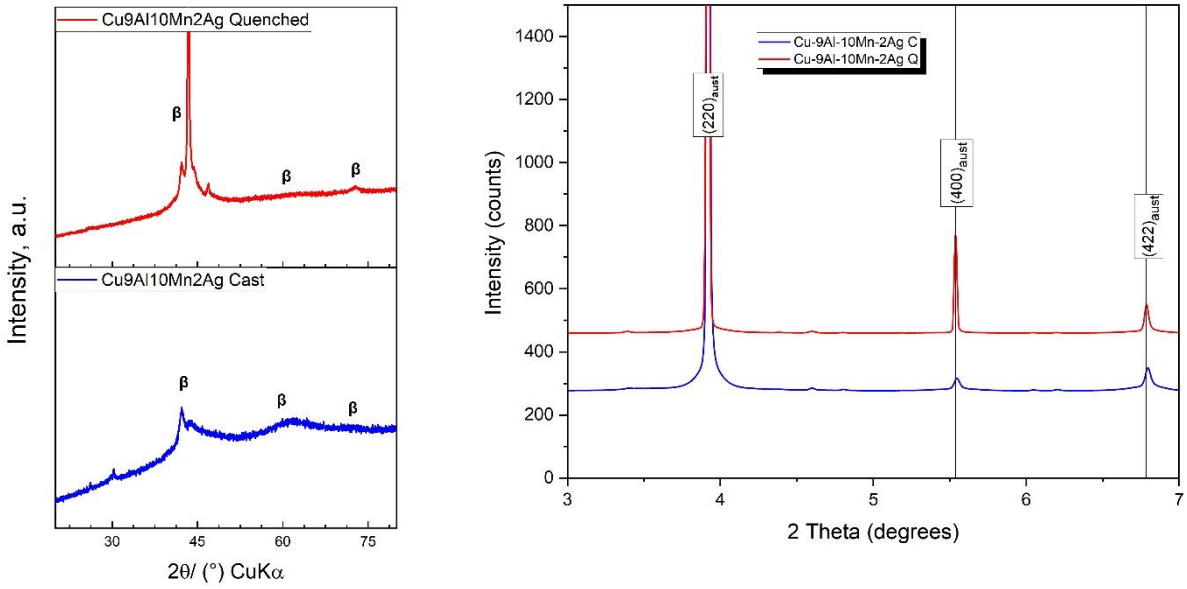

a) b)

Figure 57. *XRD diffractogram of Cu-9Al-10Mn-2Ag SMA alloy: a) regular XRD diffractogram, b) high-energy X-ray diffraction measurements from synchrotron*

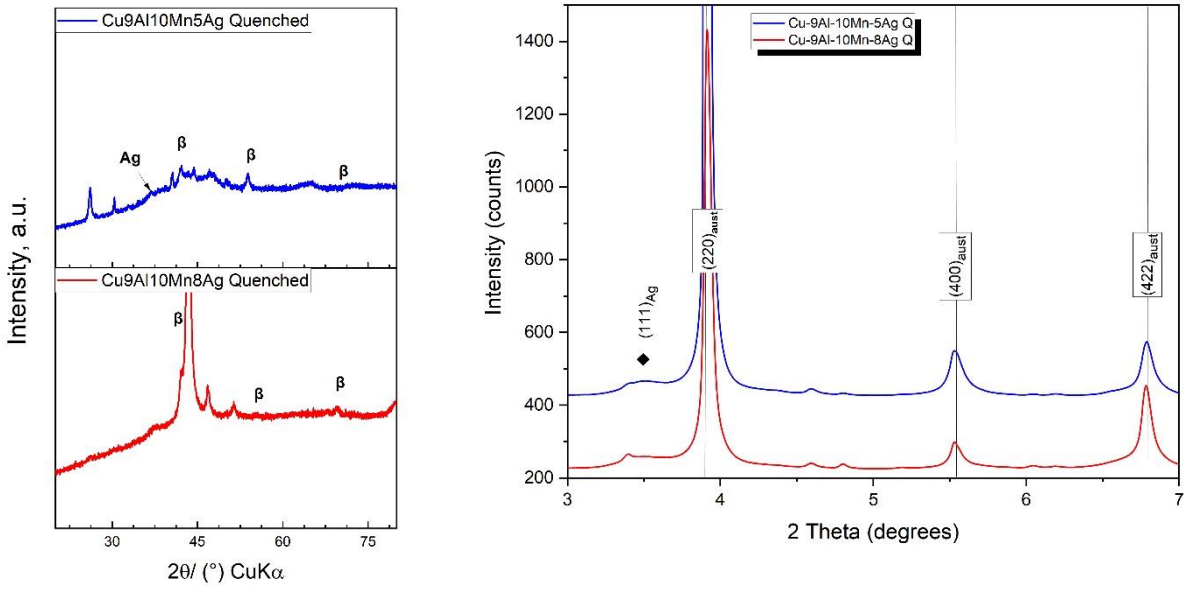

a) b)

Figure 58. *XRD diffractogram of quenched Cu-9Al-10Mn-5Ag and Cu-9Al-10Mn-8Ag SMA alloys: a) regular XRD diffractogram, b) high-energy X-ray diffraction measurements from synchrotron*

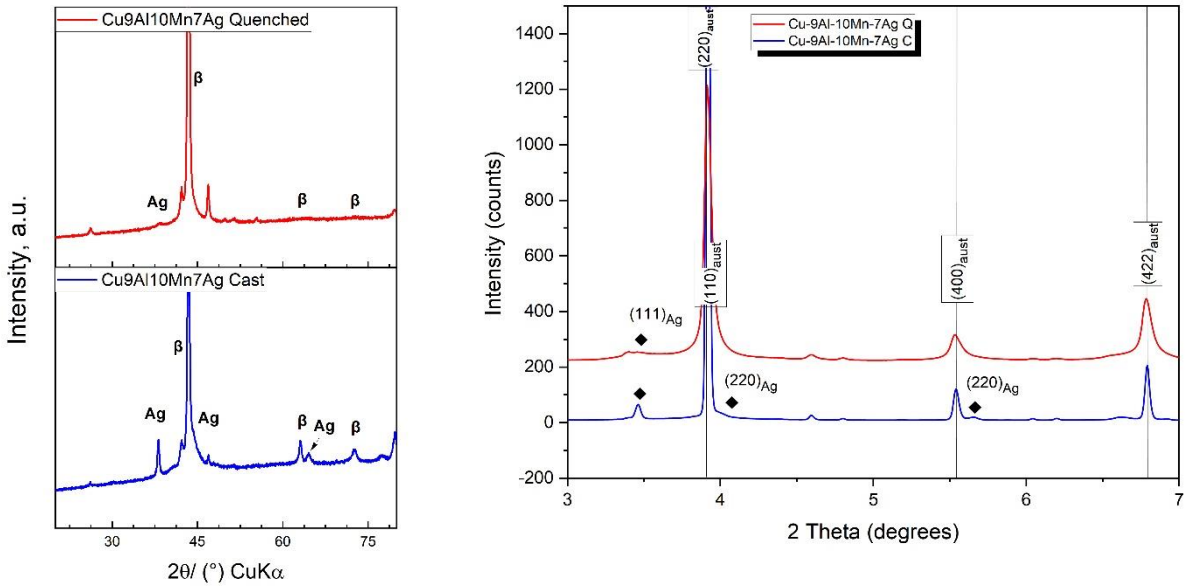

a) b)

Figure 59. *XRD diffractogram of Cu-9Al-10Mn-7Ag SMA alloy: a) regular XRD diffractogram, b) high-energy X-ray diffraction measurements from synchrotron*

4.1.4. Transmission electron microscopy (TEM)

The sample Cu-9Al-7Mn-5Ag SMA, with completely formed martensite structure after heat treatment was chosen for TEM analysis, (Fig. 60.-61.). It is confirmed β_1'(18R) structure. Figure 61.c shows the observed corresponding orientation of the selected electron diffraction patterns (SADP) of the [010] zone axis. The listed planes are parallel to the zone axis and are represented by points perpendicular to the crystallographic planes. Indicating that the SADP shows two martensitic variants of β_1' (18R) martensite visible in the dark field images in Figure 61. a, b.

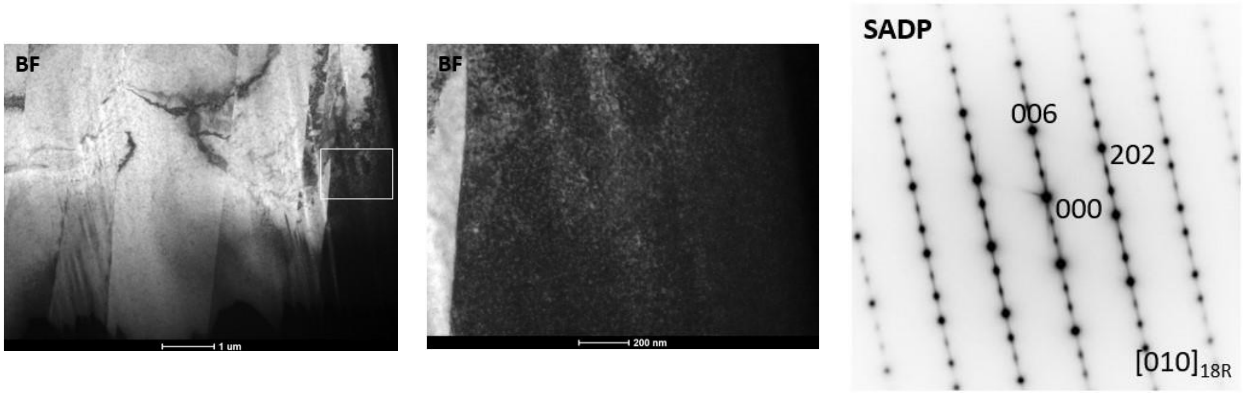

a) b) c)

Figure 60. *Microstructure of the quenched Cu9Al7Mn5Ag sample observed through a TEM: a) bright-field TEM image, b) enlarged area depicted in a bright-field TEM image, c) Selected Area Diffraction Pattern (SADP) corresponding to t to the area highlighted in Figure 60.a).*

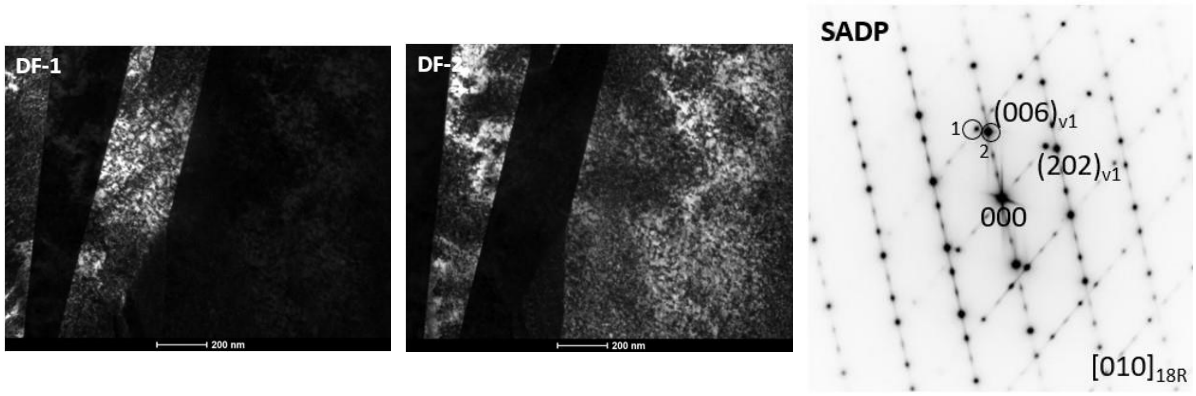

a) b) c)

Figure 61. *Microstructure of the quenched Cu9Al7Mn5Ag sample observed through a TEM: a) dark-field TEM image captured from reflections 1, b) dark-field TEM image captured from reflections 2, c) Selected Area Diffraction Pattern (SADP) corresponded to the area highlighted in Figures. 61.a) and b).*

4.1.5. Thermal analysis (DSC)

Figures from 62. through 73. display the DSC results, which are also summarized in the Table 4. The martensite transformation is a first-order process. This transition isn't merely associated with alterations in the specific heat capacity, it also involves the release of latent heat during the transformation.

DSC results for as-cast Cu-9Al-16Mn-2Ag alloy show two exothermic peaks, the first one was detectable, at M_s= 36°C, and the second one at M_s= 13°C, after 2nd cooling cycle (Fig. 62.). Results indicated existence at least partially martensite, mostly of one martensite structure β_1', and some parts of γ_1'structure.

Martensite transformation in quenched Cu-9Al-16Mn-2Ag alloy is significantly intensive, it can be seen larger exothermic peaks, with higher enthalpies of fusion. Start of martensitic transformations at M_s= 65°C in both cooling cycles, and finish temperature at M_f= 1°C (1st cooling cycle) and M_f=-15°C (2nd cooling cycle), respectively (Fig. 63.). With a lower content of manganese, 7 wt.%, the as-cast sample shows a shift of a M_s toward lower temperature, M_s= 21°C in 1st cooling cycle, and M_s = 13°C, M_f = -56°C (Fig. 64., Tab. 4.). After quenching, transition temperatures were shifted to higher values, M_s = 63°C and M_f = -44°C (2nd cycle) (Fig. 65.). Quenched samples with 7% wt. and 16% wt. of manganese exhibit similar martensitic start transformation M_s, but the enthalpy of transformation is significantly higher in Cu-9Al-7Mn-2Ag alloy, due to the more intense formation of martensite layers (Fig. 65.). Multiple exothermic peaks observable in DSC thermograms are related to reorientations of martensite layers and different martensitic structures [216].

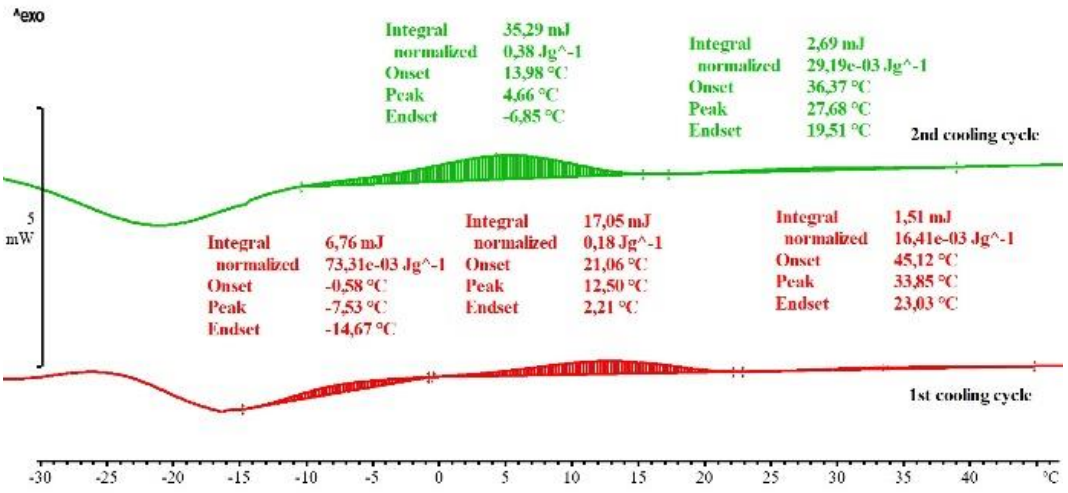

Figure 62. *DSC cooling curves of as-cast Cu-9Al-16Mn-2Ag alloy*

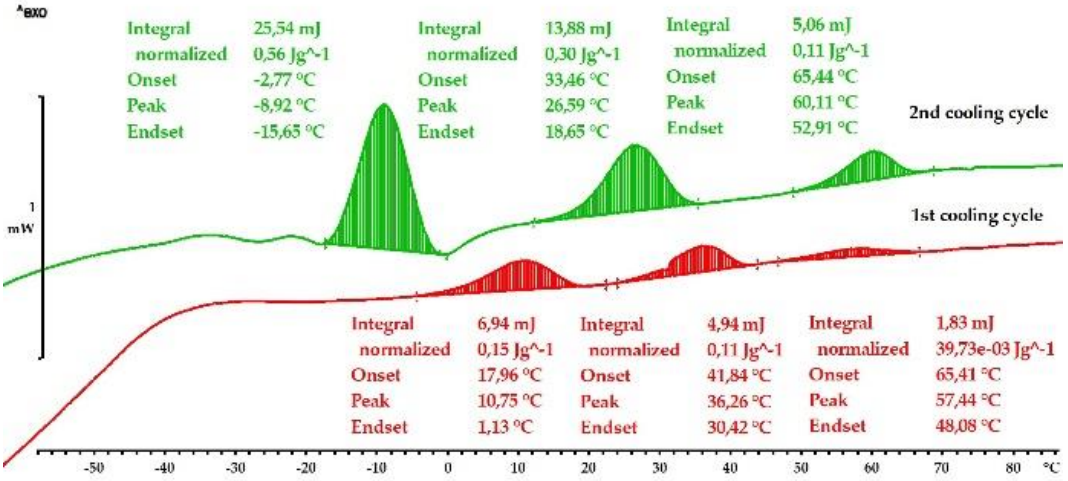

Figure 63. *DSC cooling curves of quenched Cu-9Al-16Mn-2Ag alloy*

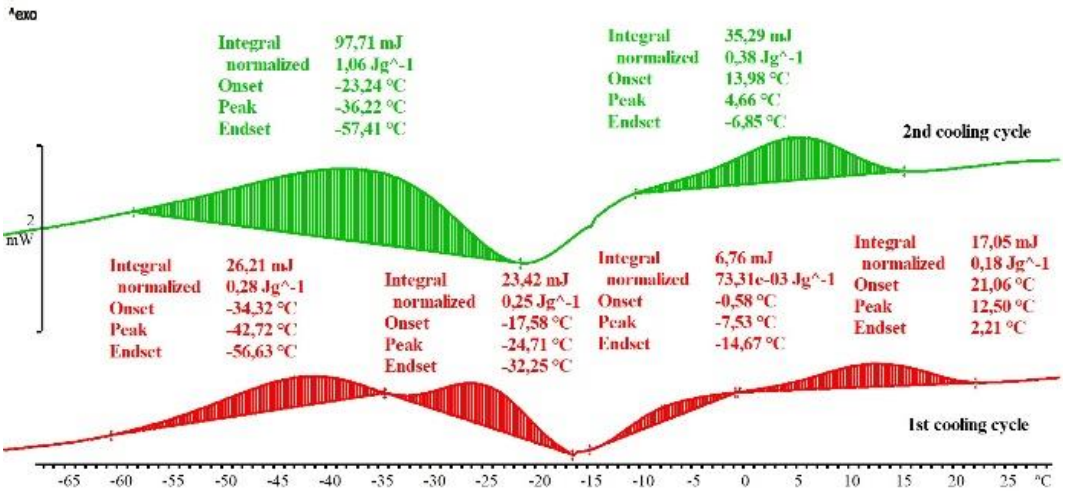

Figure 64. *DSC cooling curves of as-cast Cu-9Al-7Mn-2Ag alloy*

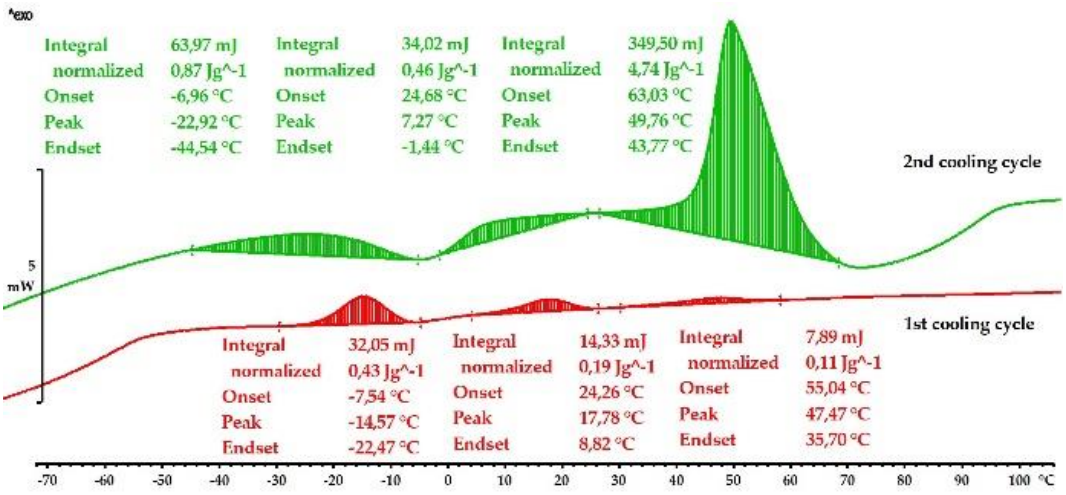

Figure 65. *DSC cooling curves of quenched Cu-9Al-7Mn-2Ag alloy*

As-cast Cu-9Al-7Mn-5Ag alloy shows the start of martensitic transformation M_s = 50°C and M_f = 1°C (2nd cycle) (Fig. 66.). After quenching, the transition temperatures were shifted to lower values, M_s = 30°C and M_f = -53°C (2nd cycle) (Fig. 67.). So, higher content of silver shifts M_s temperature to higher values (Figs. 64.-66.). Reminding influences on decreases of start martensite temperature.

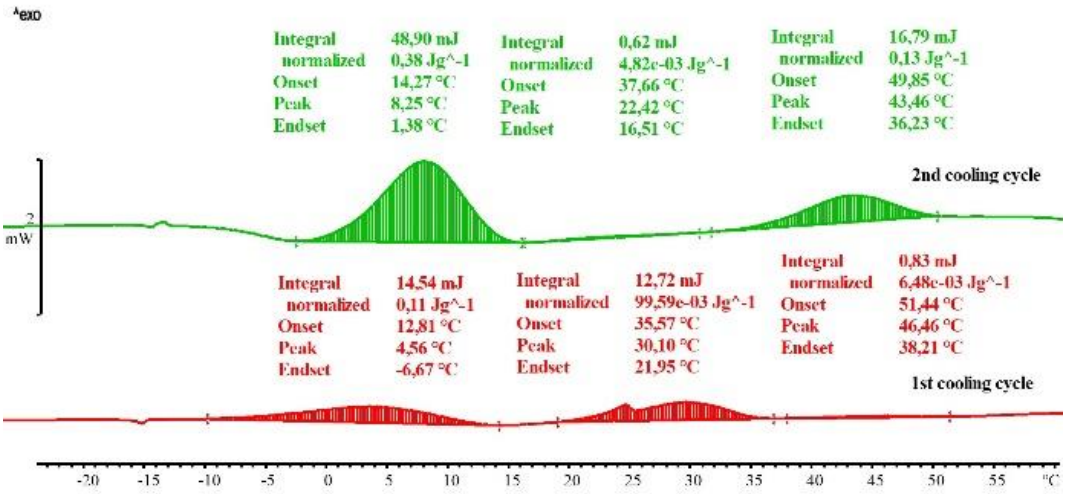

Figure 66. *DSC cooling curves of as-cast Cu-9Al-7Mn-5Ag alloy*

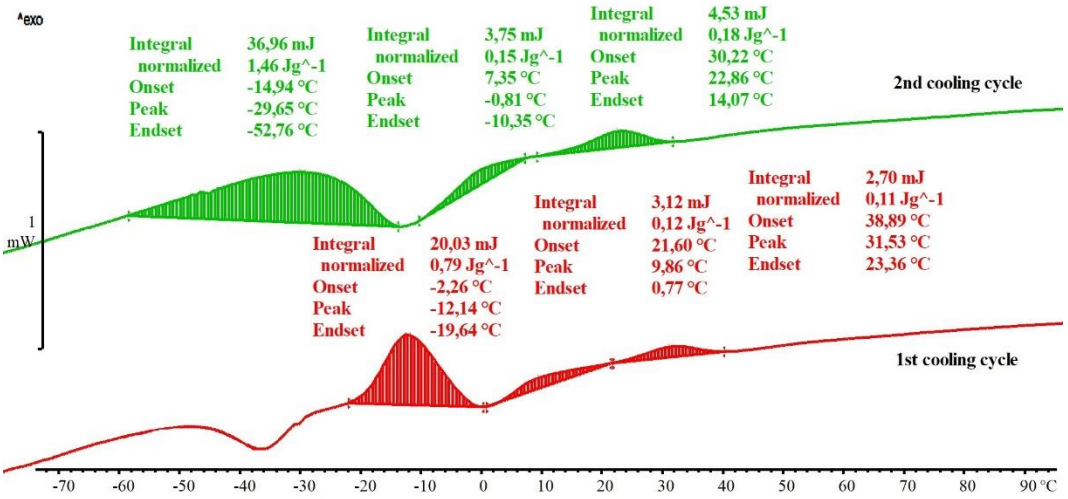

Figure 67. *DSC cooling curves of quenched Cu-9Al-7Mn-5Ag alloy*

DSC analysis of Cu-9Al-10Mn-xAg alloys showed only big exothermal peaks at significantly low temperatures. Figures 68.-69. Show DSC thermograms for Cu-9Al-10Mn-2Ag alloy, as-cast and quenched. As-cast alloy show exothermic peaks, with start temperature -44°C and -58°C (2nd cycle). Quenched alloy shows higher start temperature, at -31°C and finished at -65°C. With higher content of silver 7% wt. exothermic peaks are shifted to higher values (Figs. 70., 71.).

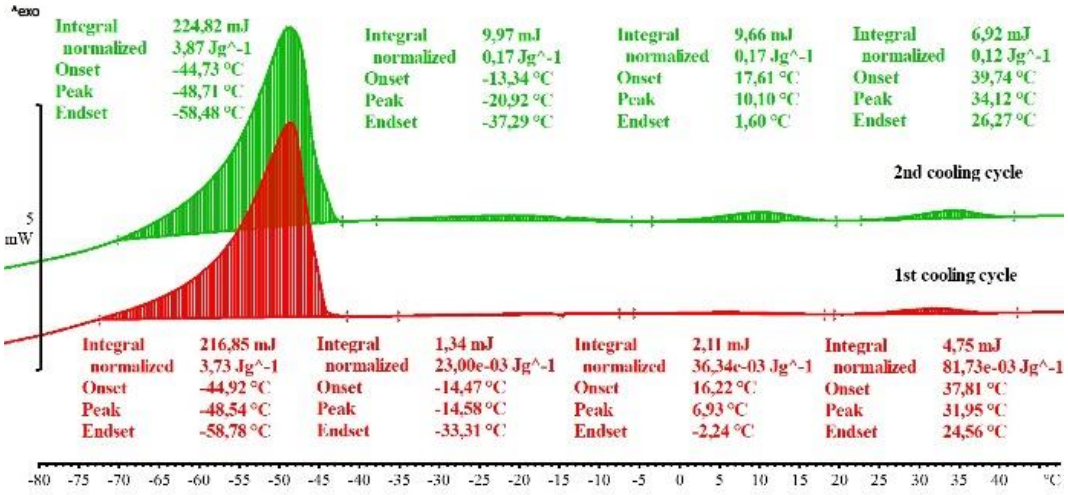

Figure 68. *DSC cooling curves of as-cast Cu-9Al-10Mn-2Ag alloy*

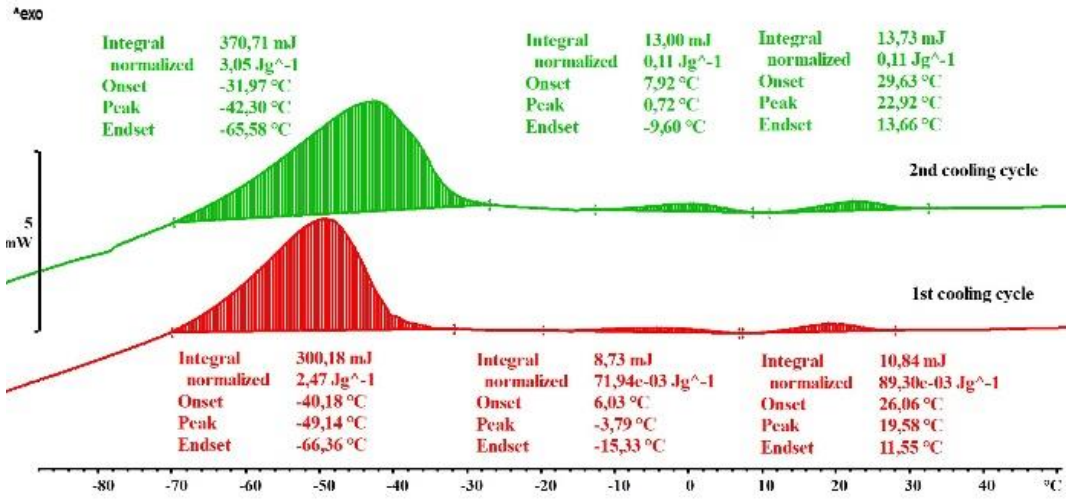

Figure 69. *DSC cooling curves of quenched Cu-9Al-10Mn-2Ag alloy*

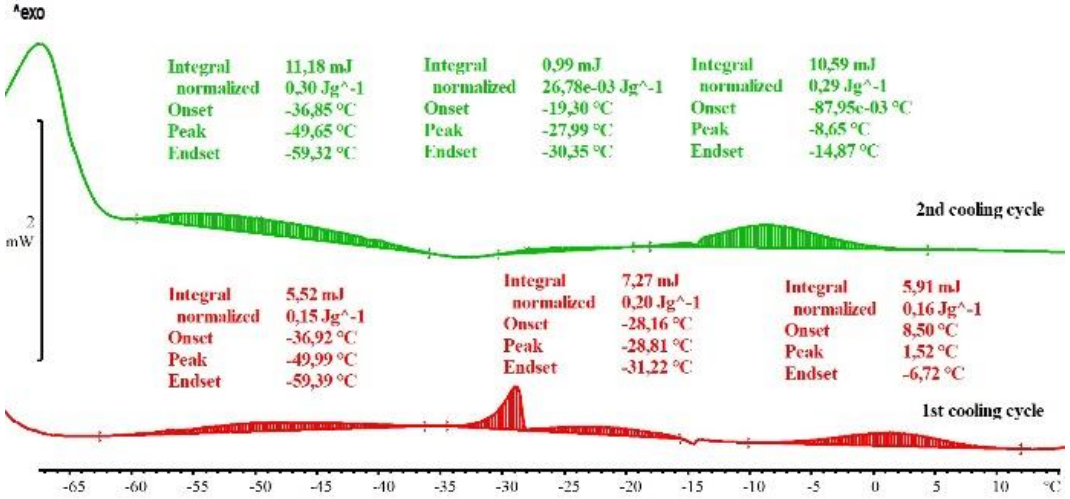

Figure 70. *DSC cooling curves of as-cast Cu-9Al-10Mn-7Ag alloy*

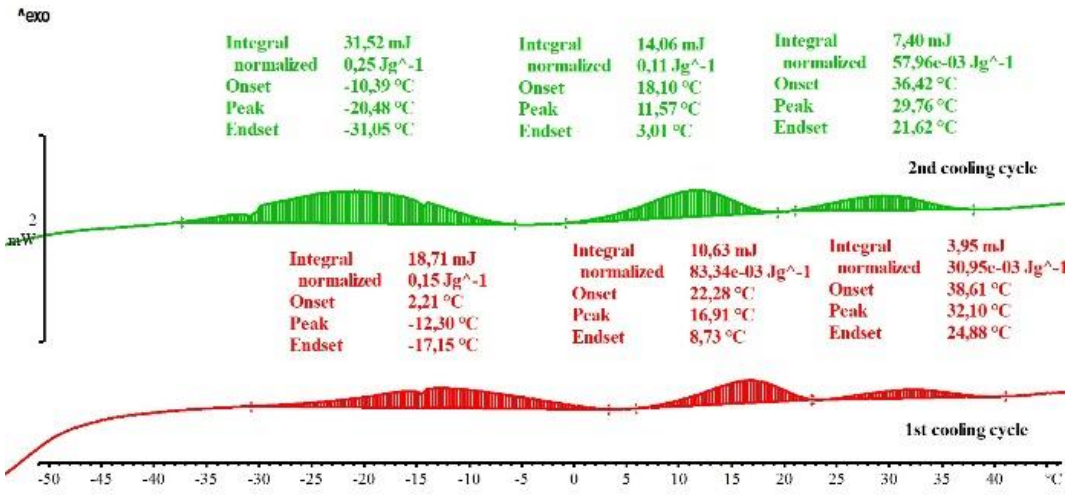

Figure 71. *DSC cooling curves of quenched Cu-9Al-10Mn-7Ag alloy*

Table 4. *DSC results of martensitic transformation temperatures and fusion enthalpy*

No.:	Sample:	M_s/°C (1st cycle)	M_f/°C (1st cycle)	M_s/°C (2nd cycle)	M_f /°C (2nd cycle)	ΔH (J/g) (2nd cycle)
1	as-cast Cu-9Al-16Mn-2Ag	45	-15	36	-7	0,41
2	quenched Cu-9Al-16Mn-2Ag	65	1	65	-15	0,97
3	as-cast Cu-9Al-7Mn-2Ag	21	-56	14	-57	1,44
4	quenched Cu-9Al-7Mn-2Ag	55	-22	64	-44	6,07
5	as-cast Cu-9Al-7Mn-5Ag	51	-7	50	1	0,51
6	quenched Cu-9Al-7Mn-5Ag	39	-20	30	-53	1,79

4.1.6. Microhardness

The microhardness of the studied Cu-Al-Mn-Ag SMA alloys is determined and presented in Table 5. Almost all investigated Cu-SMA alloys show decreased values of microhardness after quenching, what is common to SMA alloys.

The first group of alloys included those with variations in both Ag and Mn content, specifically Cu-9Al-XMn-YAg, where X represents 7, 16% wt. Mn, and Y represents 2, 5% wt. Ag. Only in Cu-SMA alloy with 16 %wt. of manganese shows a unique increase in microhardness on quenching, what is probably consequences of formation of the fragile γ_1' phase in microstructure. Alloys with a lower Mn content exhibited results that aligned with existing literature references [95-130].

In a study conducted by Silva [10], it was noted that adding Mn to a Cu-11% Al alloy notably boosts its microhardness. Yet, when 3% Ag is incorporated, the Cu-11% Al alloy experiences a minor decline in microhardness. Silva [10] highlighted that manganese modifies the boundary of phase stability, making the eutectoid reaction undetectable in annealed Cu-11% Al and Cu-11% Al-3% Ag alloy variants. Even though the introduction of silver has a minimal influence on phase transitions or microhardness, it amplifies the magnetic moment of the Cu-11% Al-10% Mn alloy approximately 2.7-fold. Additionally, it decelerates the eutectoid and peritectoid reactions in the annealed Cu-11% Al alloy. In contrast, Jain [215] discovered that the hardness of as-cast alloy samples rises in tandem with the Al:Mn ratio. Yet, for

quenched specimens, the hardness diminishes, and this reduction aligns with the Al:Mn ratio. This can be ascribed to the emergence of gentler martensitic phases at elevated ratios [216].

Cu–Al–Mn-Ag SMA alloys with a reduced manganese content of 7% wt. of manganese exhibit higher microhardness than alloys with 16% wt. of manganese addition. This indicates that the manganese content affects the microhardness in such a way that the hardness of the alloys decreases with increasing manganese content. The opposite is the case for the composition of the Cu–Al–Mn-Ag SMA alloys with higher silver addition, as the silver addition increases, the hardness of the alloy increases.

Table 5. *Microhardness of Cu–Al–Mn-Ag SMA alloys*

Cu-Al-Mn-Ag system			**Microhardness**					
No.	**Sample**	**State**	**1**	**2**	**3**	**4**	**5**	**Average**
1	Cu-9Al-16Mn-2Ag	As-cast	167,27	192,51	201,81	170,12	180,97	182,54
2	Cu-9Al-16Mn-2Ag	Quenched	244,93	235,50	237,01	238,24	241,69	239,47
3	Cu-9Al-16Mn-5Ag	As-cast	334,33	331,94	355,88	331,89	337,98	338,40
4	Cu-9Al-16Mn-5Ag	Quenched	347,65	367,40	353,06	355,98	357,74	356,37
5	Cu-9Al-16Mn-7Ag	As-cast	329,37	329,30	347,65	344,93	338,01	337,85
6	Cu-9Al-16Mn-7Ag	Quenched	398,69	438,22	412,53	367,45	403,85	404,15
7	Cu-9Al-7Mn-2Ag	As-cast	241,72	248,12	246,48	244,68	246,12	245,42
8	Cu-9Al-7Mn-2Ag	Quenched	241,72	248,17	238,52	243,67	246,12	242,38
9	Cu-9Al-7Mn-5Ag	As-cast	239,32	274,34	250,18	232,38	283,17	249,06
10	Cu-9Al-7Mn-5Ag	Quenched	257,90	229,05	225,83	153,14	213,41	216,48
11	Cu-9Al-7Mn-7Ag	As-cast	238,14	208,47	212,36	235,03	212,89	221,38
12	Cu-9Al-7Mn-7Ag	Quenched	290,75	305,78	264,89	276,76	285,27	284,69
13	Cu-9Al-10Mn-2Ag	As-cast	297,21	283,23	292,52	328,92	292,54	300,47
14	Cu-9Al-10Mn-2Ag	Quenched	276,56	282,53	286,47	280,34	282,64	281,71
15	Cu-9Al-10Mn-5Ag	Quenched	326,90	358,77	361,78	344,96	348,97	348,28
16	Cu-9Al-10Mn-7Ag	As-cast	261,87	250,23	278,78	274,30	287,87	266,30
17	Cu-9Al-10Mn-7Ag	Quenched	339,66	337,07	331,90	334,87	338,14	336,33
18	Cu-9Al-10Mn-8Ag	Quenched	314,81	364,62	353,06	326,90	373,51	346,58

4.2. Ternary Cu-Al-Ag SMA alloys

4.2.1. Microstructure investigations

Microstructural examination of the studied Cu-Al-Ag alloys in both the as-cast and quenched states was performed using OM and SEM (Figs. 72-98.). OM images were taken in bright field settings and under polarized light.

The as-cast state microstructure, as depicted in Figure 72., presents precipitates od α-phase within β_1' matrix. Investigated ternary Cu-Al-Ag alloys show very good shape memory properties and potential for high temperature applications. At the grain boundaries, early signs of martensite structure formation are evident. Within the grains, brief needle-like martensite crystals are discernible, likely of the β_1'-type, boasting a monoclinic 18R structure originating from the DO_3 parent phase. Polarized OM images clearly highlight grain boundaries and distinct orientations of the martensite crystals within them. Following quenching, a fully developed martensite structure becomes apparent (Fig. 73.). The visible crystals are solely of the β_1'-martensite type, primarily exhibiting a characteristic zig-zag formation (Figs. 73-74.). Due to their controlled growth in self-accommodating patterns, these β_1'-martensite variants demonstrate thermoelastic properties [214]. Needle-type and wedge-type 18R martensite formations are presented in Figure 74.

SEM images of the quenched state reveal the presence of only a single type of martensite. Notably absent are the coarse plates characteristic of γ_1' martensite, another thermally induced martensite variant found in Cu-Al SMAs. The nucleation driving force for γ_1' (2H) outstrips that for β_1' (18R) martensite. Whether the 18R and 2H structures coexist hinges on both the alloy's composition and the specifics of its thermal treatment. Distinct morphologies characterize β_1' and γ_1', stemming from their unique inhomogeneous shear mechanisms. For 18R martensite, this inhomogeneous shear results from the scattered stacking disorder in the β-parent phase. Conversely, in 2H martensite, such shear arises due to twinning on a {1 2 1} plane [214, 216].

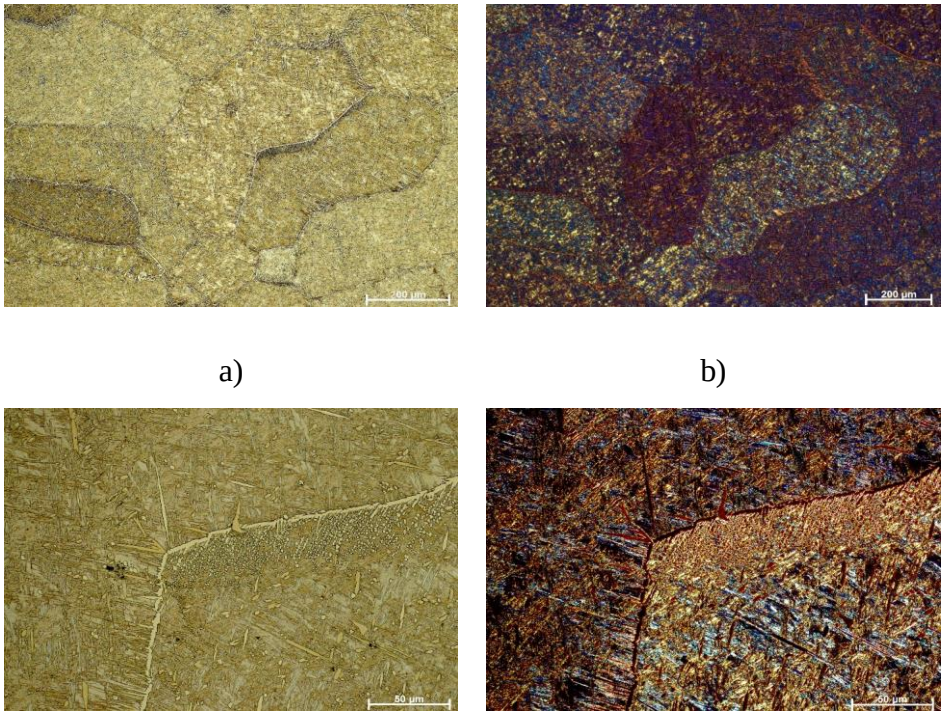

a) b)

c) d)

Figure 72. *OM micrographs of as-cast Cu-10Al-1Ag SMA alloy: a) BF, magnification 100x, b) POL, magnification 100x, c) BF, magnification 500x, d) POL, magnification 500x*

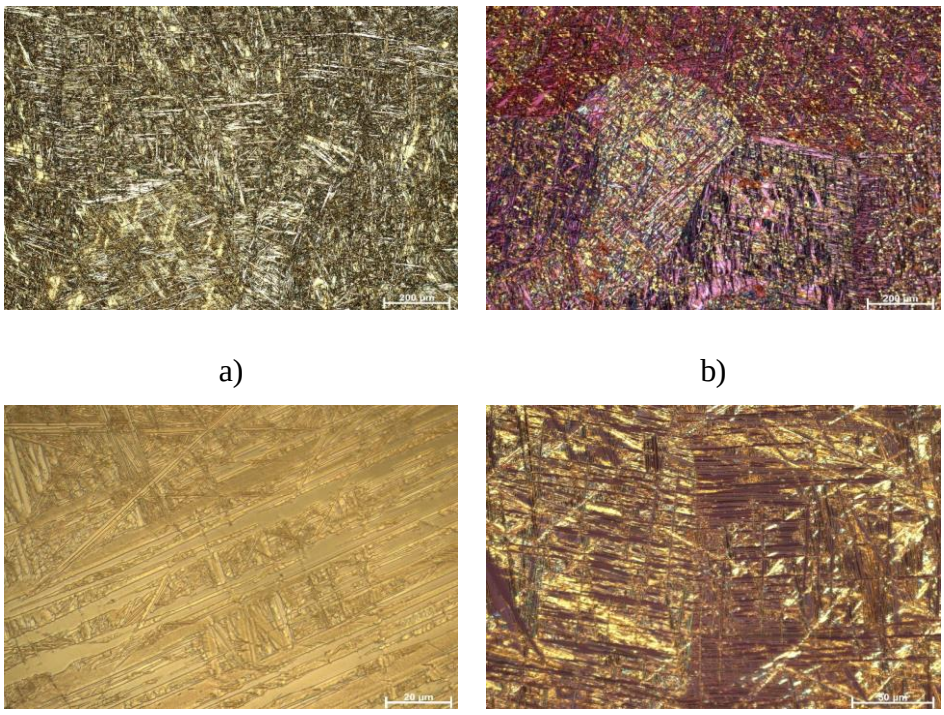

a) b)

c) d)

Figure 73. *OM micrographs of quenched Cu-10Al-1Ag shape memory alloy: a) BF, magnification 100x, b) POL, magnification 100x, c) BF, magnification 500x, d) POL, magnification 500x*

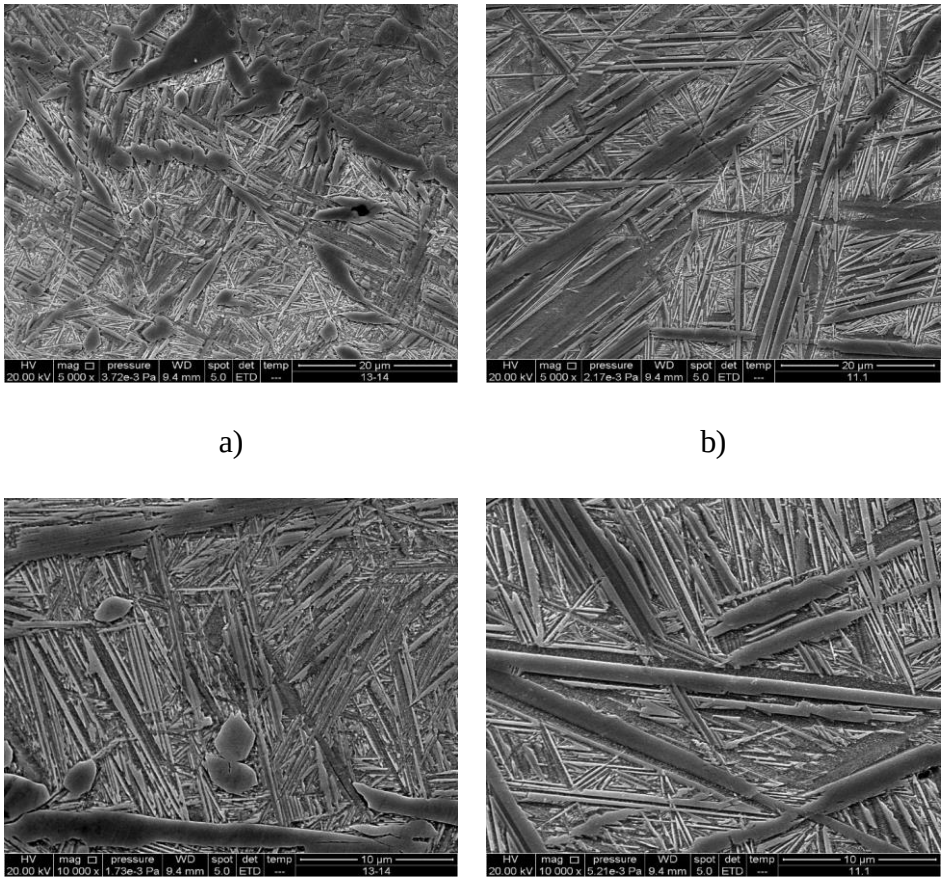

Figure 74. *SEM micrograph of Cu-10Al-1Ag shape memory alloy, magnification 5000x: a) as-cast state, b) quenched state, and magnification 10000x: c) as-cast state, d) quenched state*

SEM-EDS analysis of both investigated states confirmed designated composition (Figs. 75.-76.).

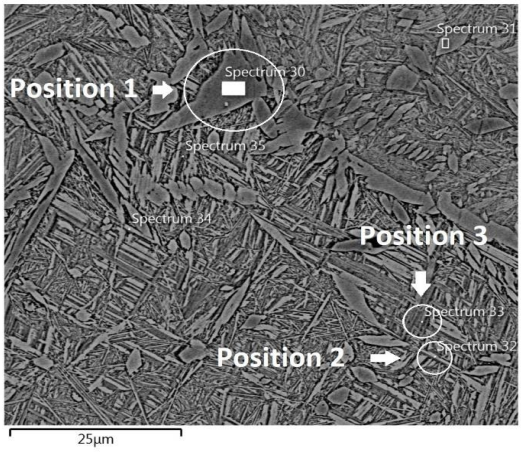

Element	Position 1 (wt.%)	Position 2 (wt.%)
Al	8.82 ±0.25	9.87 ±0.46
Cu	88.17 ±0.70	83.39 ±1.30
Ag	1.40 ±0.23	1.27 ±0.40

Figure 75. *EDS analysis of as-cast Cu-10Al-1Ag alloy*

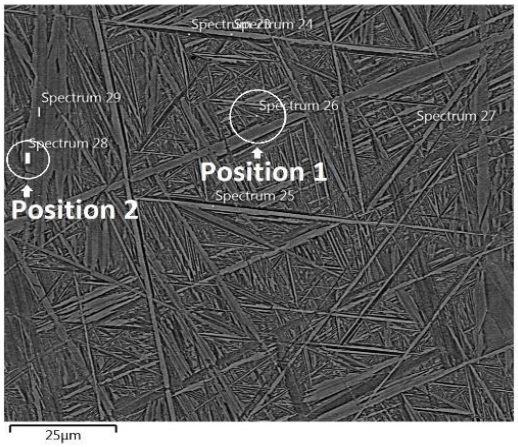

Element	Position 1 (wt.%)	Position 2 (wt.%)
Al	10.92 ±0.46	10.90 ±0.51
Cu	88.00 ±0.59	88.17 ±0.64
Ag	1.09 ±0.42	0.93 ±0.44

Figure 76. *EDS analysis of quenched Cu-10Al-1Ag alloy*

Cu-10Al-2Ag alloy in the as-cast state has two-phase morphology, with α precipitate and even detectable 18R martensite (Figs. 77-78.)

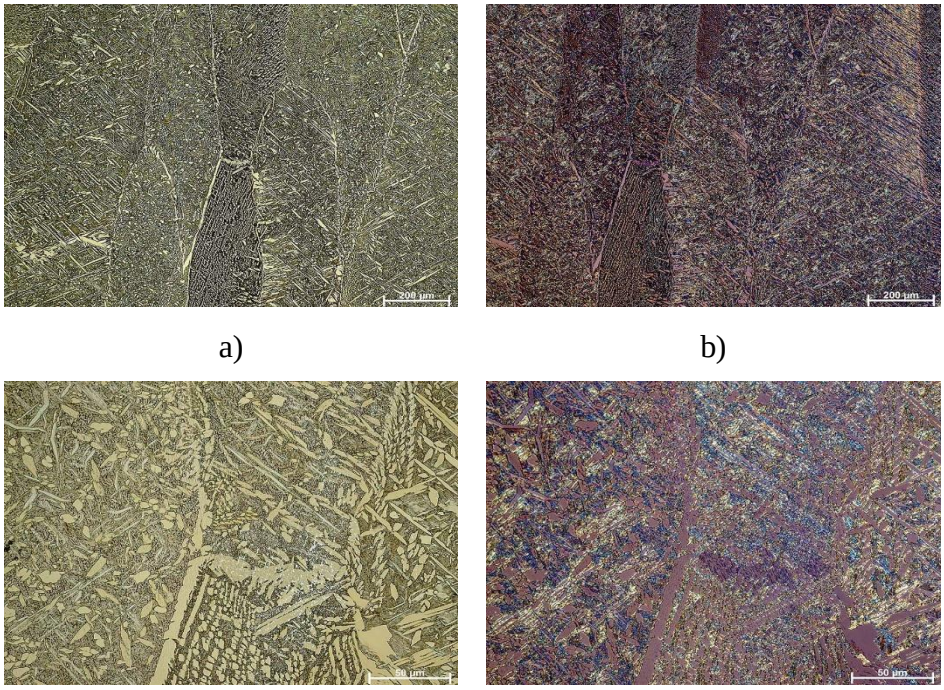

a) b)

c) d)

Figure 77. *OM micrographs of as-cast Cu-10Al-2Ag SMA alloy: a) BF, mag. 100x, b) POL, mag 100x, c) BF, mag. 500x, d) POL, mag. 500x*

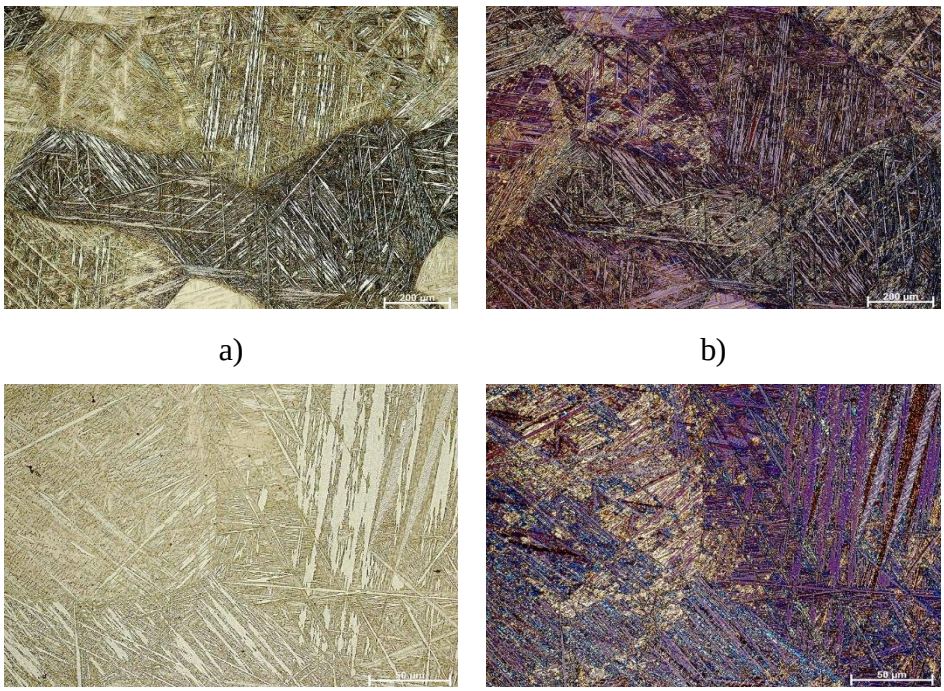

a) b)

c) d)

Figure 78. *OM micrographs of Quenched Cu-10Al-2Ag SMA alloy: a) BF, mag. 100x, b) POL, mag 100x, c) BF, mag. 500x, d) POL, mag. 500x*

SEM micrographs (Fig. 79.) show that in both samples, as in the previous sample, there is only martensite of V type β_1'. Moreover, after quenching, as in the previous Cu-10Al-1Ag SMA alloy, the alloy forms a fully developed martensite structure in the metal matrix, with most of the β_1' martensite present with zigzag formations.

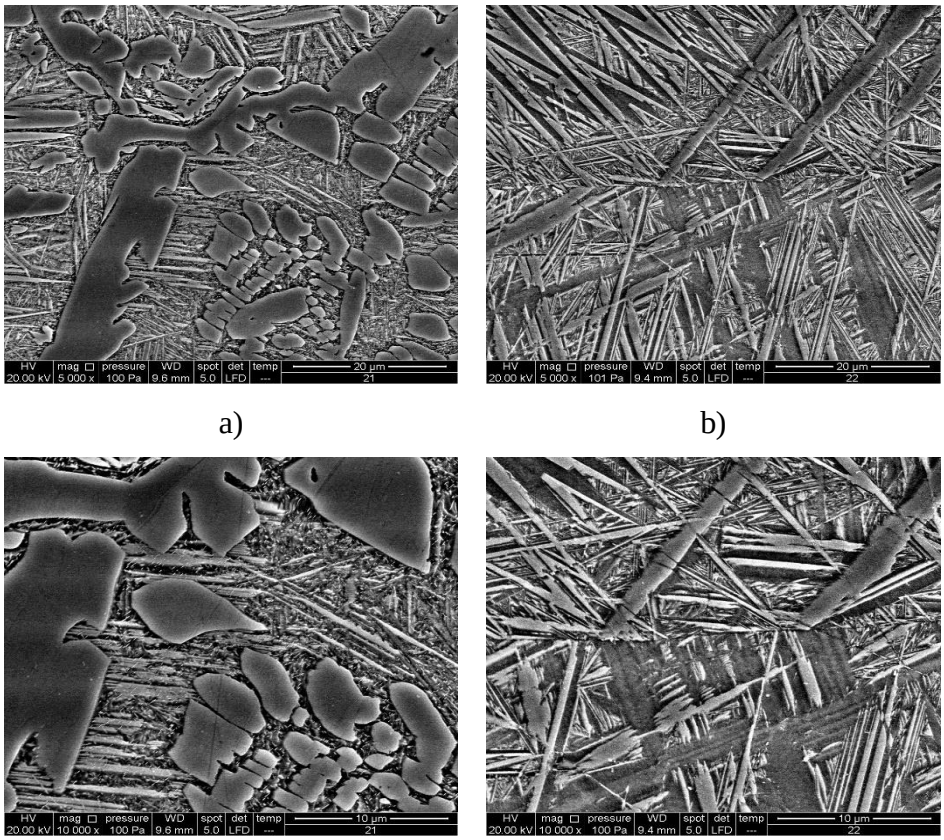

Figure 79. *SEM micrograph of Cu-10Al-2Ag SMA alloy, mag. 5000x: a) As-cast state, b) Quenched state, and mag. 10000x: c) As-cast state, d) Quenched state*

In EBSD analysis on Figure 80., BS images, band contrast, and phase maps are presented for the as-cast Cu-10Al-2Ag SMA alloy, were the α-phase (f.c.c)-Cu precipitates are highlighted in green. The quenched alloy is mainly characterized by spear-like forms in the β_1'-martensite plate group, as seen in Figure 80. d). EBSD evaluations expose diverse patterns within microregions, corresponding to habit variants of the 18R martensite.

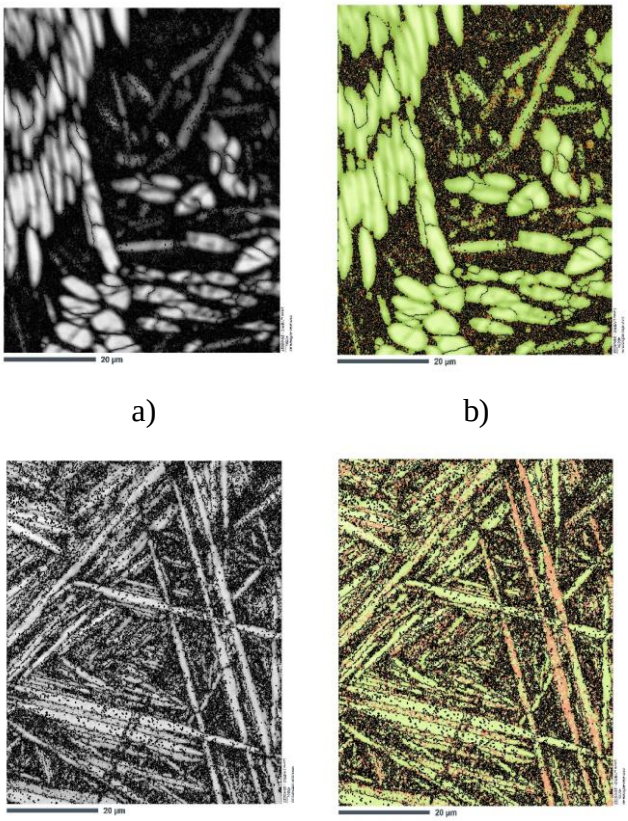

Figure 80. *Results of EBSD measurements for the Cu10Al2Ag alloy: a) band contrast image, b) phase map in the as-cast state, and c) band contrast image, d) phase map in the quenched state.*

OM the microscopic images of the Cu-10Al-5Ag SMA alloy in the as-cast and quenched state show elongated grains with martensite needles (Fig. 81.). Higher silver contents in the composition of Cu-Al-Ag SMA alloys affect the martensite and make the martensite needles thinner and longer compared to earlier alloys. After quenching, silver precipitates can be observed through the martensite matrix (Figs. 81.-83.).

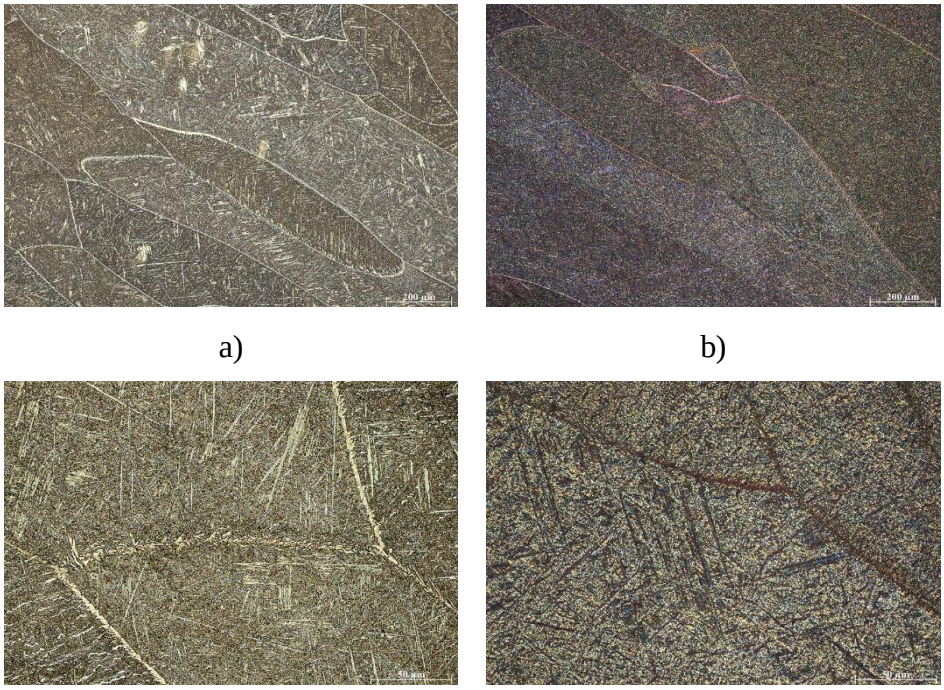

a) b)

c) d)

Figure 81. *OM micrographs of as-cast Cu-10Al-5Ag SMA alloy: a) BF, mag. 100x, b) POL, mag 100x, c) BF, mag. 500x, d) POL, mag. 500x*

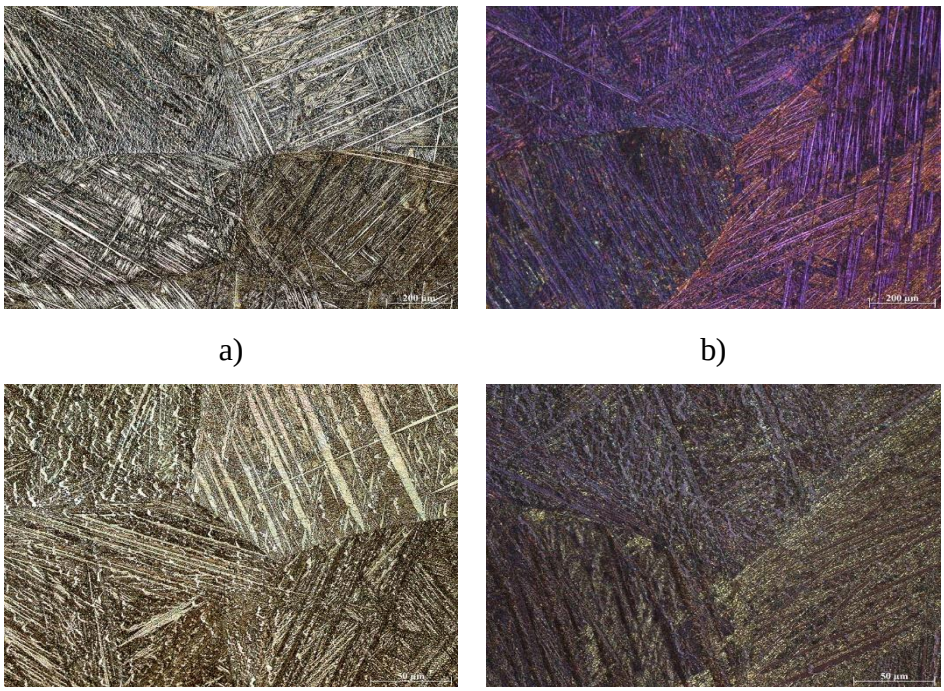

a) b)

c) d)

Figure 82. *OM micrographs of Quenched Cu-10Al-5Ag SMA alloy: a) BF, mag. 100x, b) POL, mag 100x, c) BF, mag. 500x, d) POL, mag. 500x*

As with the previous alloys, the SEM micrographs (Fig. 83.) show the presence of V-type martensite β_1', in both states, and clearly the noticeable influence of silver addition, which was previously detected on OM micrographs. The alloy shows small Ag precipitates, which appear especially at the grain boundaries. After quenching, the same precipitates can be seen in the martensite images, which were found at EDS in the martensitic matrix for both SMA alloys, Cu-10Al-2Ag and Cu-10Al-5Ag (Fig. 84-85.).

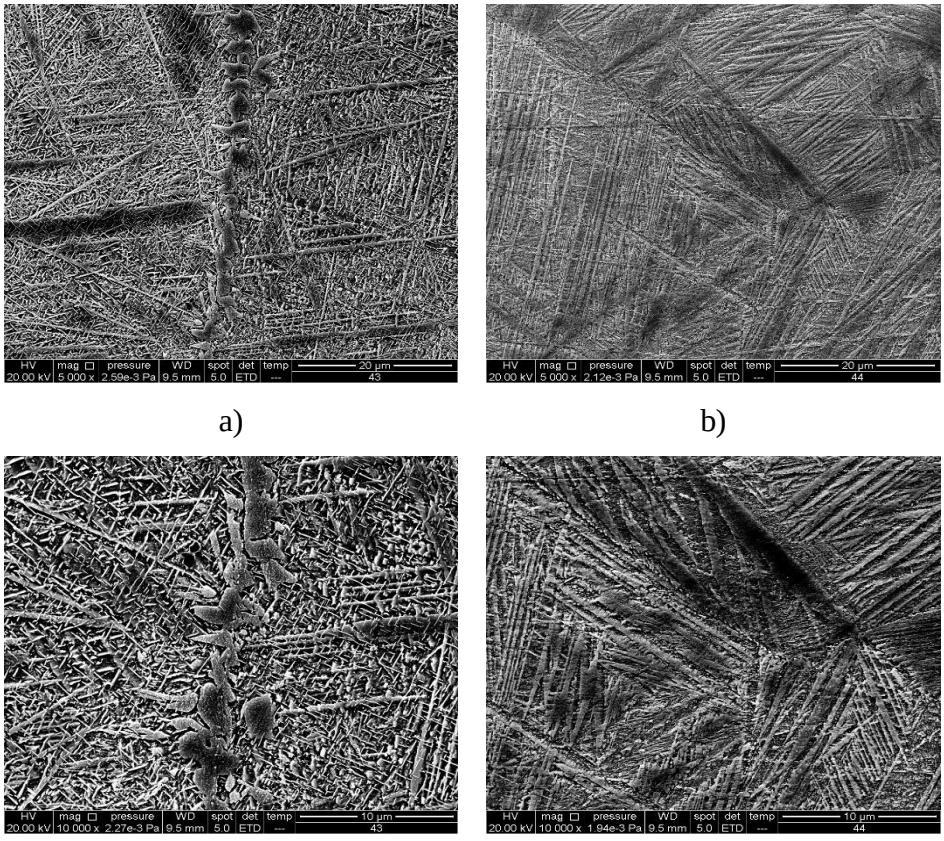

Figure 83. *SEM micrograph of Cu-10Al-5Ag SMA alloy, mag. 5000x: a) As-cast state, b) Quenched state, and mag. 10000x: c) As-cast state, d) Quenched state*

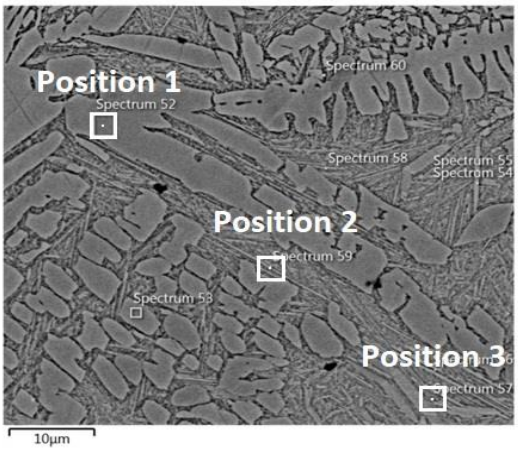

a)

Element	Position 1 (wt.%)	Position 2 (wt.%)	Position 3 (wt.%)
Al	9.46 ±0.24	10.91 ±0.52	9.22 ±0.40
Cu	86.21 ±0.69	84.09 ±1.38	84.01 ±1.11
Ag	2.16 ±0.23	1.74 ±0.47	2.42 ±0.40

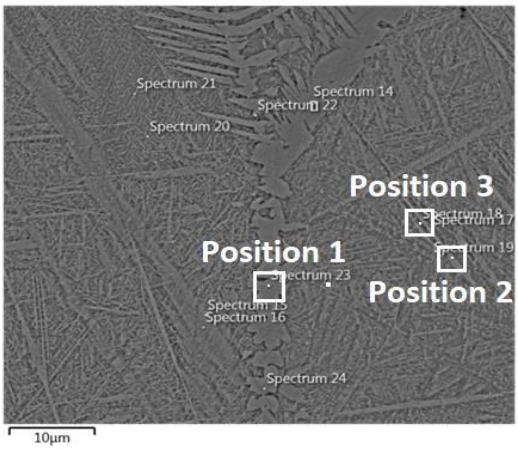

b)

Element	Position 1 (wt.%)	Position 2 (wt.%)	Position 3 (wt.%)
Al	8.96 ±0.34	10.33 ±0.40	9.12 ±0.39
Cu	85.41 ±0.50	85.09 ±0.56	85.71 ±0.57
Ag	5.62 ±0.40	4.58 ±0.43	5.16 ±0.45

Figure 84. *EDS analysis of: a) as-cast Cu-10Al-2Ag alloy, b) as-cast Cu-10Al-5Ag alloy*

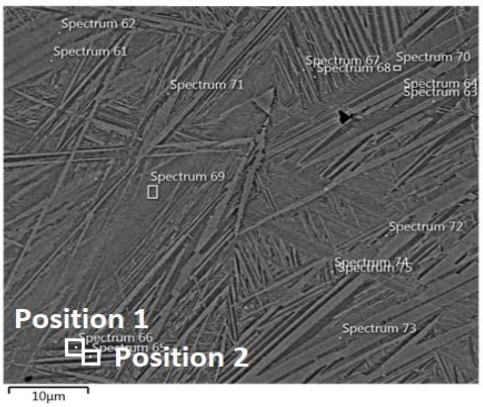

a)

Element	Position 1 (wt.%)	Position 2 (wt.%)
Al	9.93 ±0.52	10.57 ±0.45
Cu	85.19 ±1.35	86.48 ±0.59
Ag	2.20 ±0.51	2.96 ±0.42

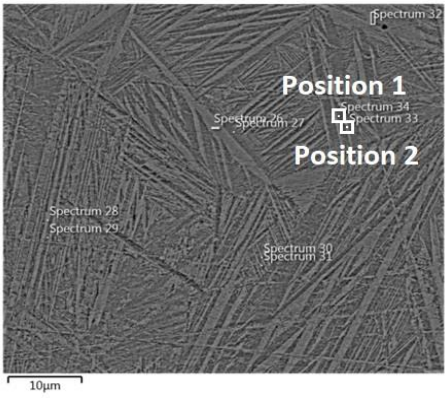

b)

Element	Position 1 (wt.%)	Position 2 (wt.%)
Al	9.80 ±0.31	10.16 ±0.33
Cu	81.05 ±0.85	81.41 ±0.88
Ag	6.32 ±0.35	6.58 ±0.38

Figure 85 *EDS analysis of: a) quenched Cu-10Al-2Ag alloy, b) quenched Cu-10Al-5Ag alloy*

The EBSD analysis of the quenched Cu-10Al-5Ag alloy in Figure 86. shows similar contrast and phase maps to those of the quenched Cu-10Al-2Ag alloy. However, there is a more distinct martensite morphology and heavily strained regions and phase boundaries in the as-cast state that differ, indicating an influence of silver addition on martensite formation and throwing structure.

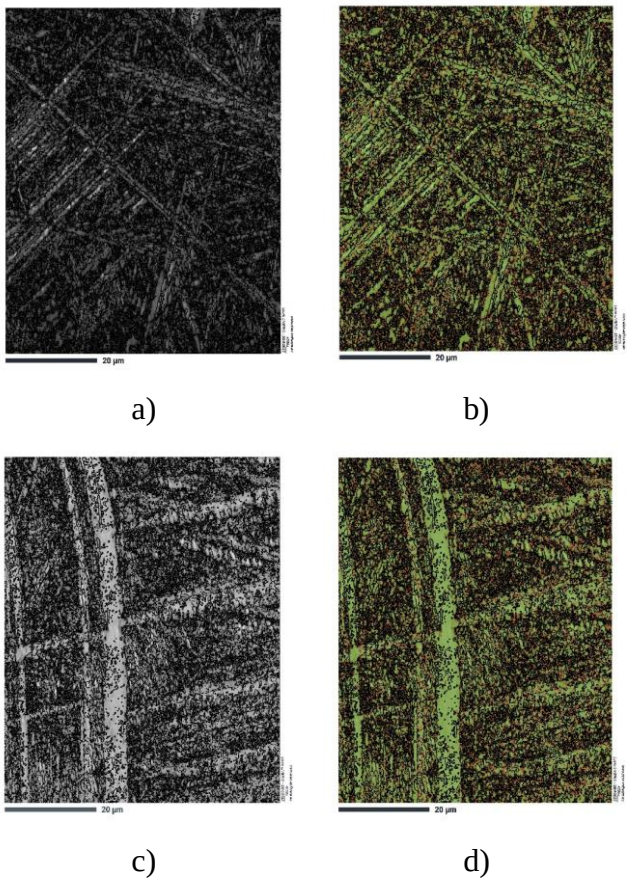

Figure 86. *Results of EBSD measurements for the Cu10Al5Ag alloy: a) band contrast image, b) phase map in the as cast state, and c) band contrast image, d) phase map in the quenched state.*

Similar observations are seen with higher composition of silver, 7% wt. (Figs. 87.-91.).

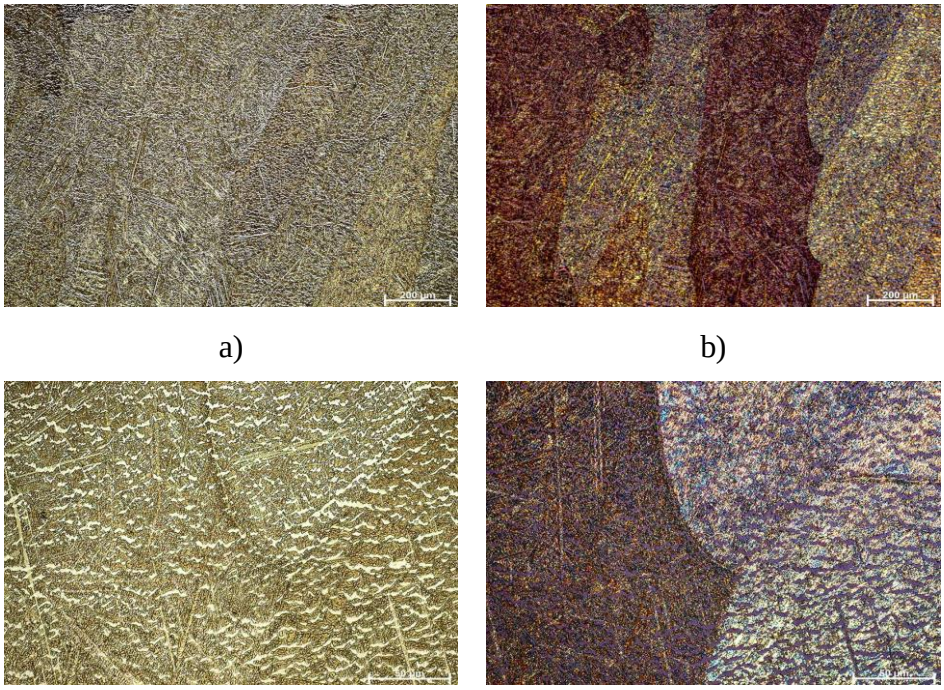

a) b)

c) d)

Figure 87. *OM micrographs of as-cast Cu-10Al-7Ag SMA alloy: a) BF, mag. 100x, b) POL, mag 100x, c) BF, mag. 500x, d) POL, mag. 500x*

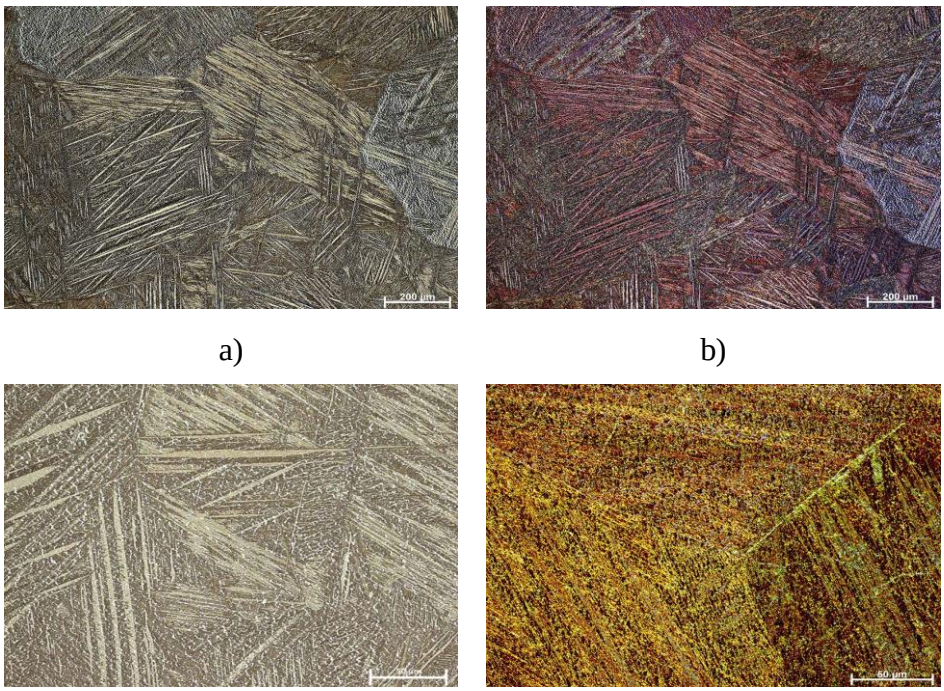

a) b)

c) d)

Figure 88. *OM micrographs of quenched Cu-10Al-7Ag SMA alloy: a) BF, mag. 100x, b) POL, mag 100x, c) BF, mag. 500x, d) POL, mag. 500x*

SEM micrographs (Fig. 89.) also show the presence of V-type martensite β_1', in both states. The as-cast Cu-10Al-7Ag alloy shows silver precipitates in the metal matrix and especially at the grain boundaries. After quenching, the same precipitates are seen in martensite pates. In both states, the precipitates were detected by EDS examination over the metal matrix of the Cu-10Al-7Ag alloy and shown in Figure 90.

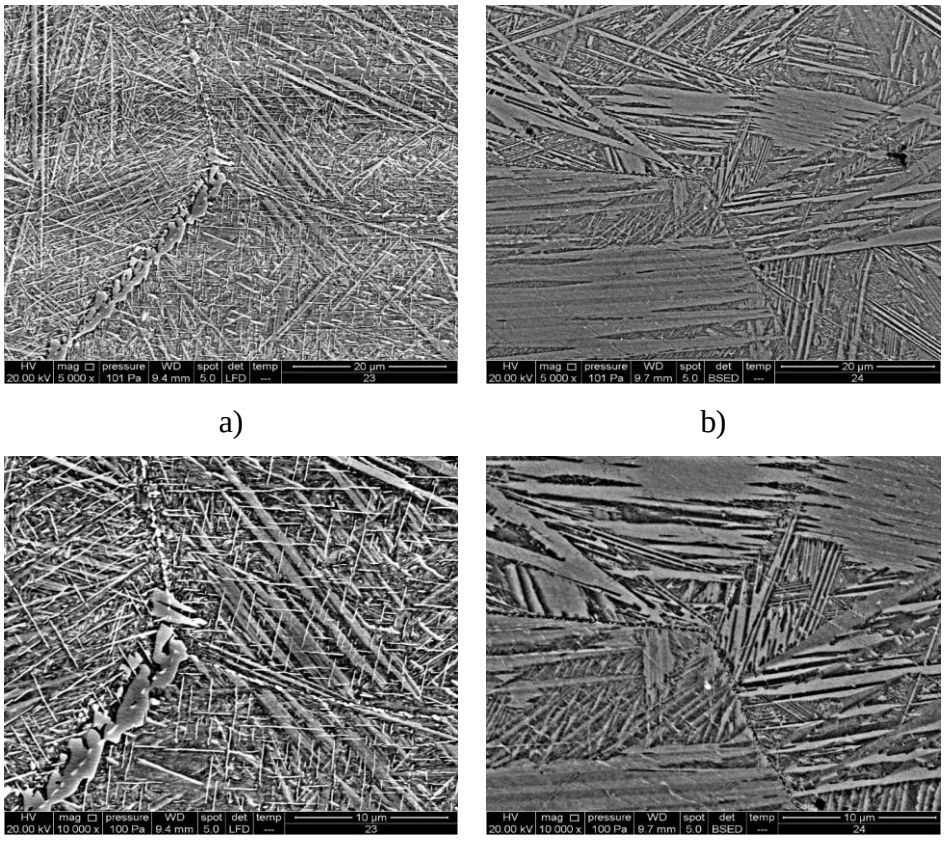

Figure 89. *SEM micrograph of Cu-10Al-7Ag SMA alloy, mag. 5000x: a) As-cast state, b) Quenched state, and mag. 10000x: c) As-cast state, d) Quenched state*

The EBSD evaluations show different patterns within microregions corresponding to habit variants of the 18R martensite. One notable difference detected in Figure 91. is in the size of the martensite needles when comparing the as-cast and quenched states.

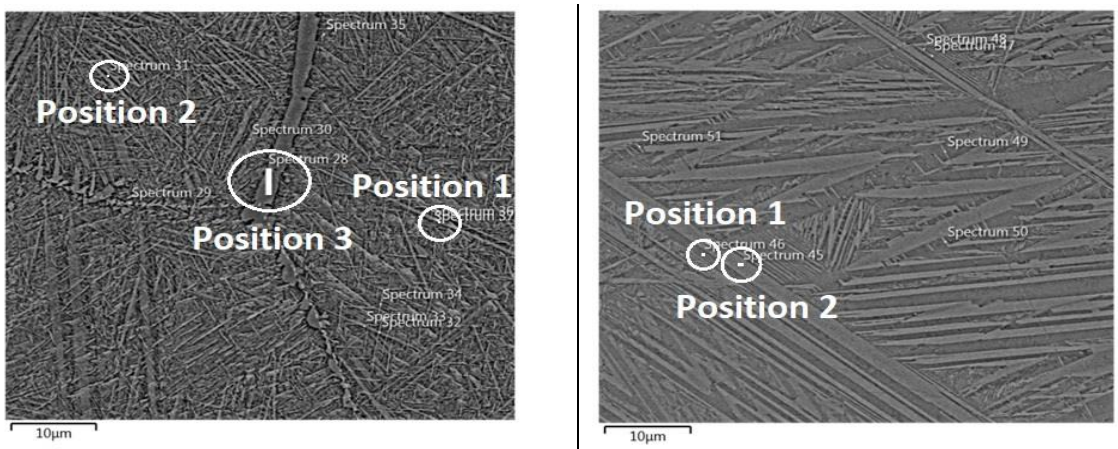

a) b)

Element	Position 1 (wt.%)	Position 2 (wt.%)	Position 3 (wt.%)
Al	9.21 ±0.20	11.67 ±0.56	10.28 ±0.42
Cu	80.87 ±0.55	81.90 ±0.81	81.51 ±0.63
Ag	6.78 ±0.24	6.44 ±0.65	8.21 ±0.52

Element	Position 1 (wt.%)	Position 2 (wt.%)
Al	9.70 ±1.11	9.70 ±1.11
Cu	80.41 ±1.70	80.41 ±1.70
Ag	9.89 ±1.42	9.89 ±1.42

***Figure 90**. EDS analysis of Cu-10Al-7Ag alloy; a) As-cast state, b) quenched state*

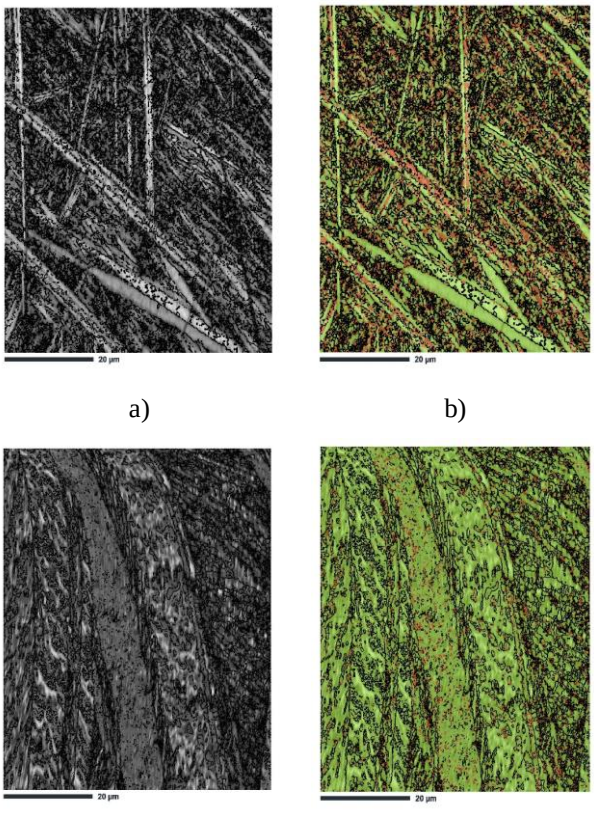

a) b)

c) d)

***Figure 91.** Results of EBSD measurements for the Cu10Al7Ag alloy: a) band contrast image, b) phase map in the as-cast state, and c) band contrast image, d) phase map in the quenched state.*

Cu-10Al-20Ag SMA alloy show a completely different morphology (Figs. 92.-96.). The Cu-10Al-20Ag SMA alloy in Figure 92. shows a saturated metal matrix with silver precipitates. The martensite structure is difficult to distinguish. The heat treatment process (Fig. 95.) affects the precipitation in such a way that the Ag precipitation from the metal matrix in the initial state undergoes a secondary process under high temperature, and the Ag precipitation from the matrix goes to the grain boundaries and is deposited there, affecting the grains.

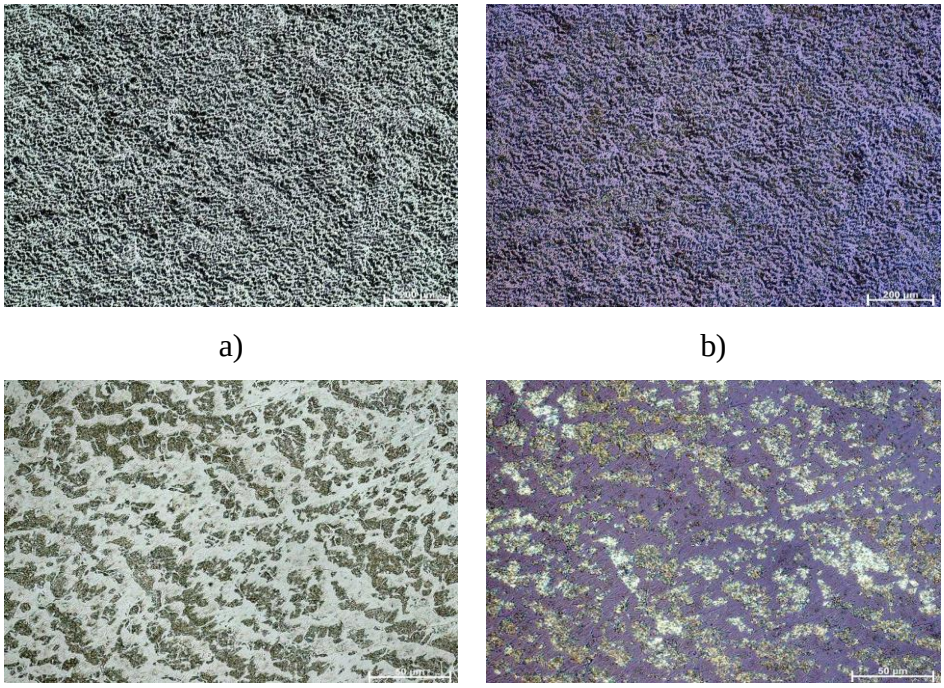

a) b)

c) d)

Figure 92. *OM micrographs of as-cast Cu-10Al-20Ag SMA alloy: a) BF, mag. 100x, b) POL, mag 100x, c) BF, mag. 500x, d) POL, mag. 500x*

SEM micrographs (Fig. 94.) show the existence of V-type martensite β1', in both states under high magnifications, characterized by thin, needle-like shapes, as in the previously shown alloys. The precipitation of silver is visible in each state, but it is noticeable that the silver precipitates collect as nodules on the grains and also precipitate on the grain boundaries after quenching. What is further EDS examination in the metal matrix of Cu-10Al-20Ag alloy in both states (Fig. 95.).

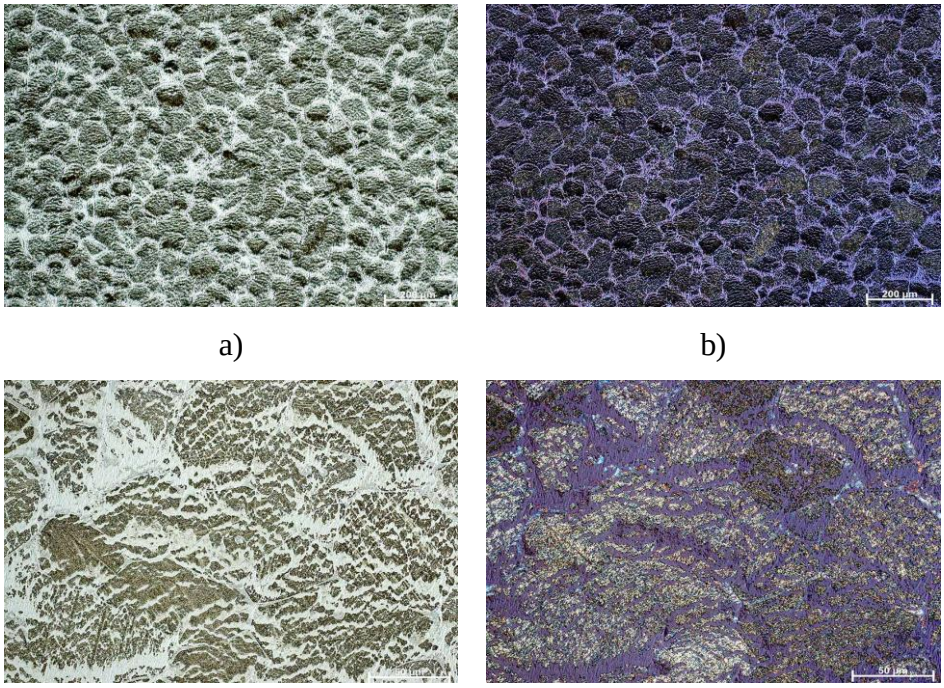

a) b)

c) d)

Figure 93. *OM micrographs of Quenched Cu-10Al-20Ag SMA alloy: a) BF, mag. 100x, b) POL, mag 100x, c) BF, mag. 500x, d) POL, mag. 500x*

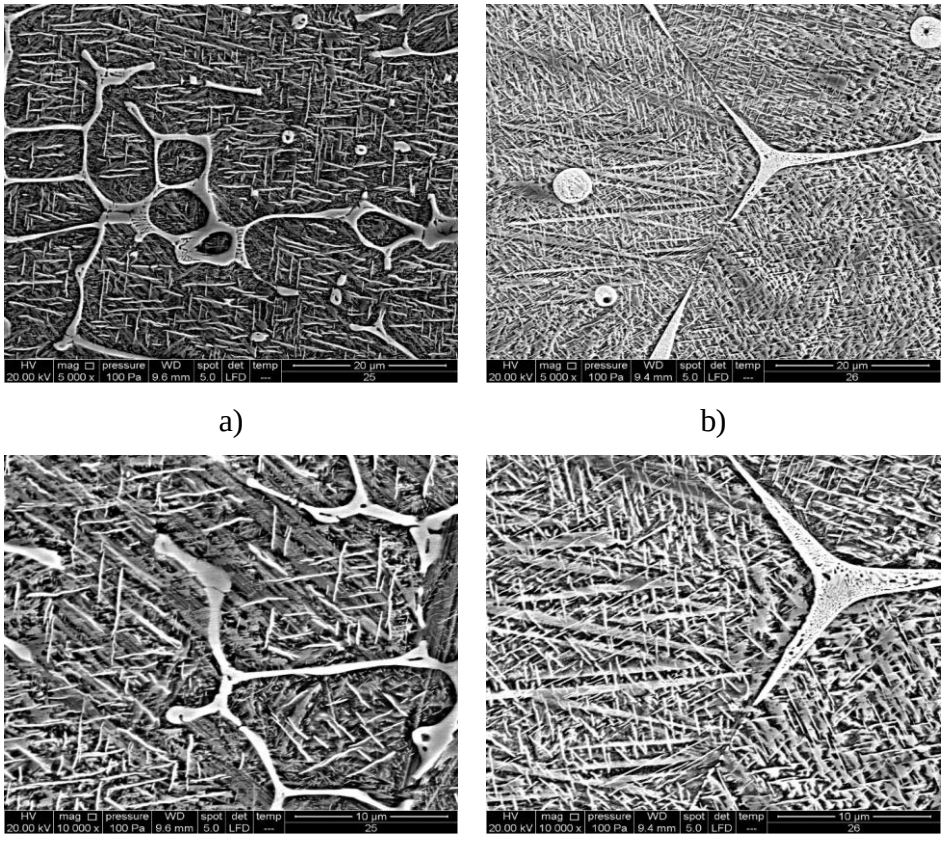

a) b)

c) d)

Figure 94. *SEM micrograph of Cu-10Al-20Ag SMA alloy, mag. 5000x: a) As-cast state, b) Quenched state, and mag. 10000x: c) As-cast state, d) Quenched state*

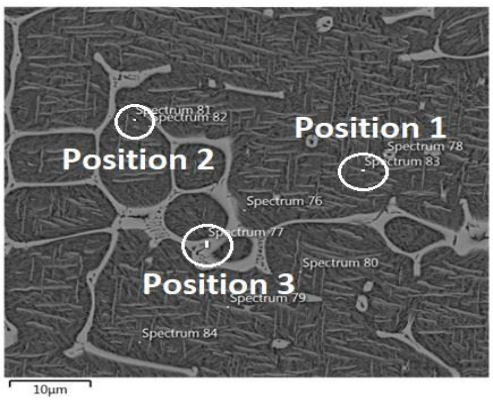

a)

Element	Position 1 (wt.%)	Position 2 (wt.%)	Position 3 (wt.%)
Al	10.37 ±1.04	12.01 ±0.76	5.11 ±0.38
Cu	70.78 ±1.86	73.97 ±1.21	37.19 ±0.95
Ag	18.85 ±1.70	14.01 ±1.06	57.71 ±0.96

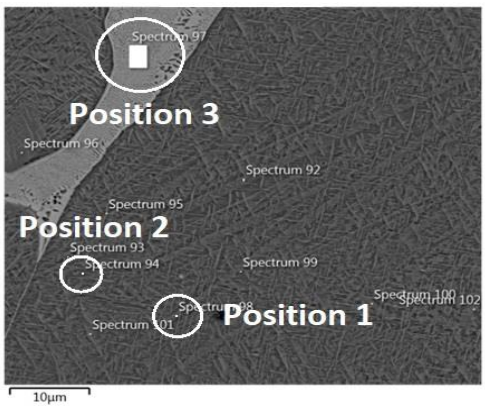

b)

Element	Position 1 (wt.%)	Position 2 (wt.%)	Position 3 (wt.%)
Al	10.99 ±1.07	10.88 ±1.06	5.00 ±0.76
Cu	68.60 ±1.84	71.49 ±1.75	30.49 ±1.85
Ag	20.40 ±1.66	17.64 ±1.55	64.50 ±1.89

Figure 95. *EDS analysis of Cu-10Al-20Ag alloy; a) as-cast state, b) quenched state*

EBSD analysis in Figure 96. confirms the presence of spear-like forms as a β_1' martensite plate group.

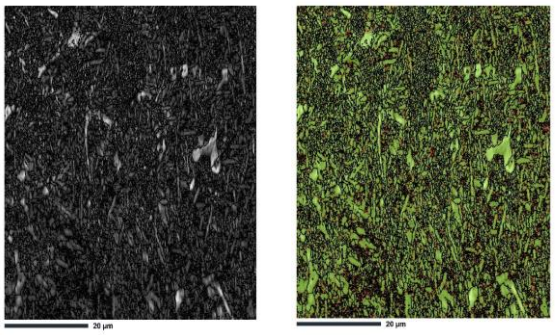

a) b)

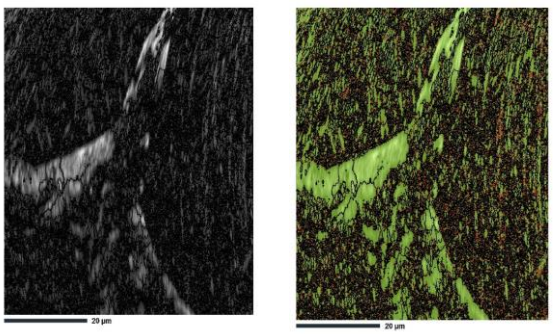

c) d)

Figure 96. *Results of EBSD measurements for the Cu10Al20Ag alloy: a) band contrast image, b) phase map in the as-cast state, and c) band contrast image, d) phase map in the quenched state.*

4.2.2. X-ray diffraction analysis (XRD)

XRD results confirmed phase identifications in ternary Cu-Al-Ag SMA alloys. Both high-energy X-ray diffraction results confirmed results of OM and SEM results and coexistence of β_1' (18R) monoclinic martensite type in the Cu-Al-Ag SMA alloys. XRD results also confirmed precipitates of α-phase (f.c.c. Cu) in as-cast state of alloys with low additions of silver composition in as-cast states (Figs. 97., 98.).

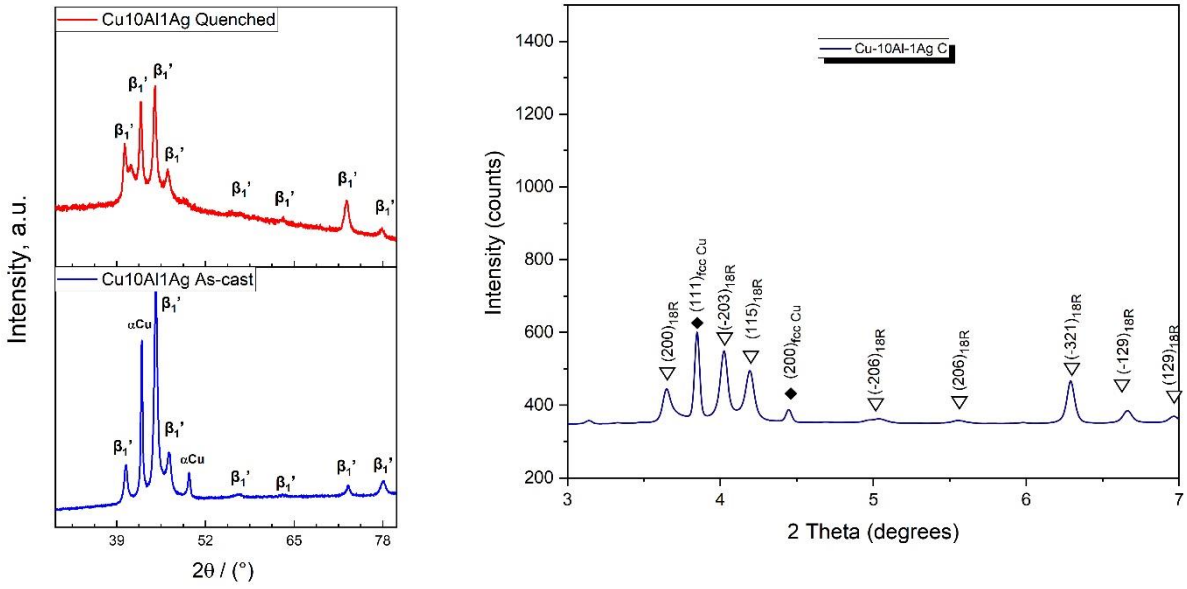

a) b)

Figure 97. *XRD diffractogram of Cu-10Al-1Ag SMA alloy: a) regular XRD diffractogram, b) high-energy X-ray diffraction measurements from synchrotron*

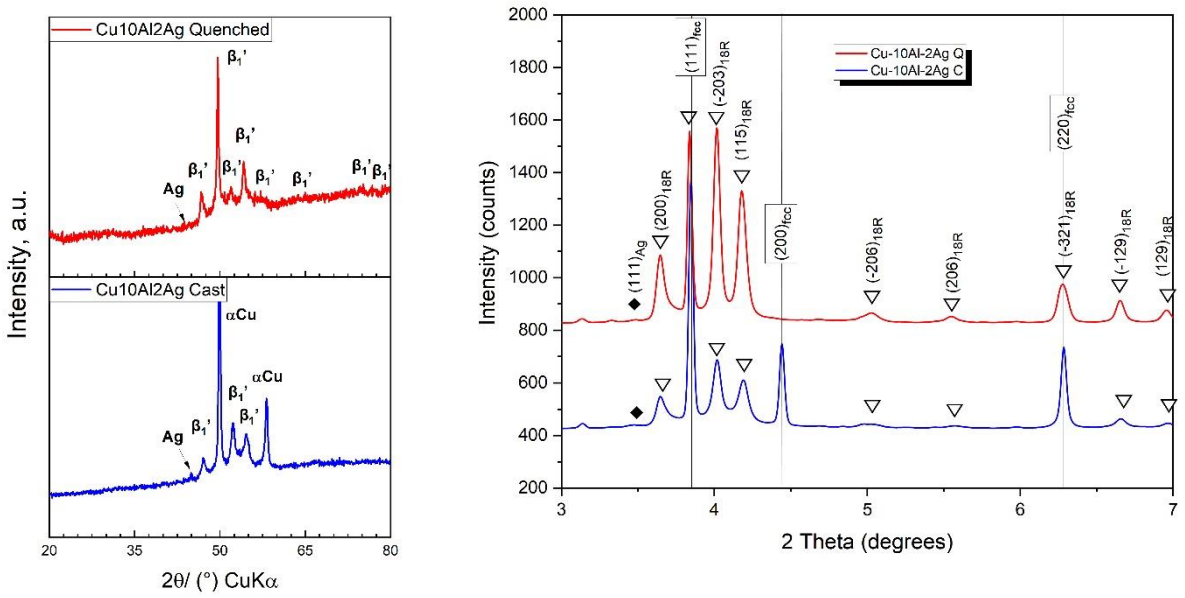

a) b)

Figure 98. *XRD diffractogram Cu-10Al-2Ag SMA alloy: a) regular XRD diffractogram, b) high-energy X-ray diffraction measurements from synchrotron*

The XRD results also confirmed precipitates of pure silver in alloys with higher addition of silver compositions, which was identified in both states (Figs. 99.-101.).

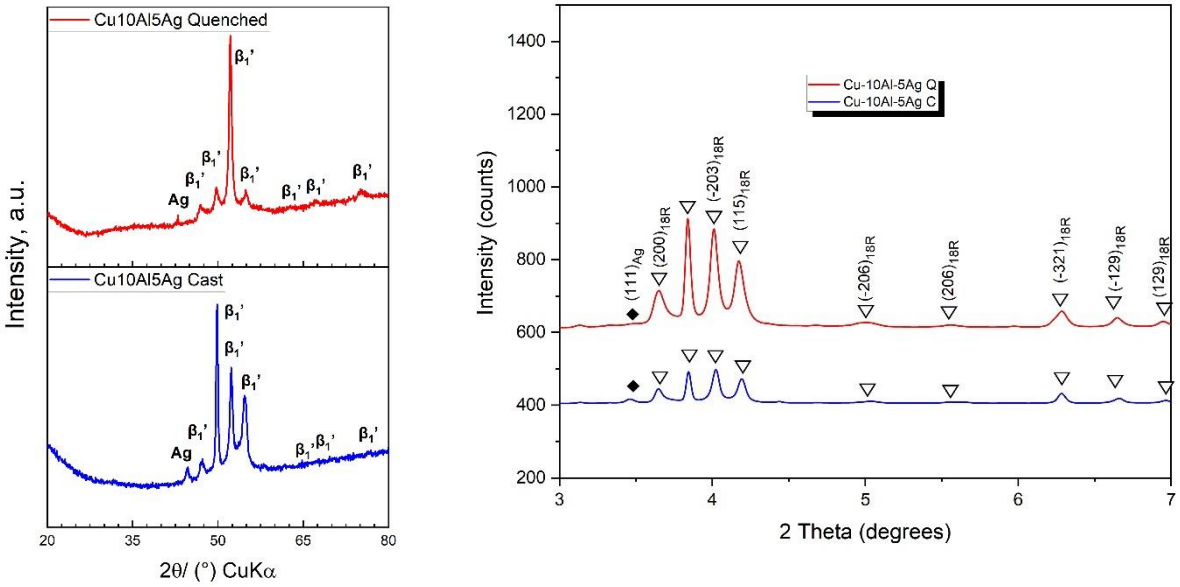

a) b)

Figure 99. *XRD diffractogram of Cu-10Al-5Ag SMA alloy: a) regular XRD diffractogram, b) high-energy X-ray diffraction measurements from synchrotron*

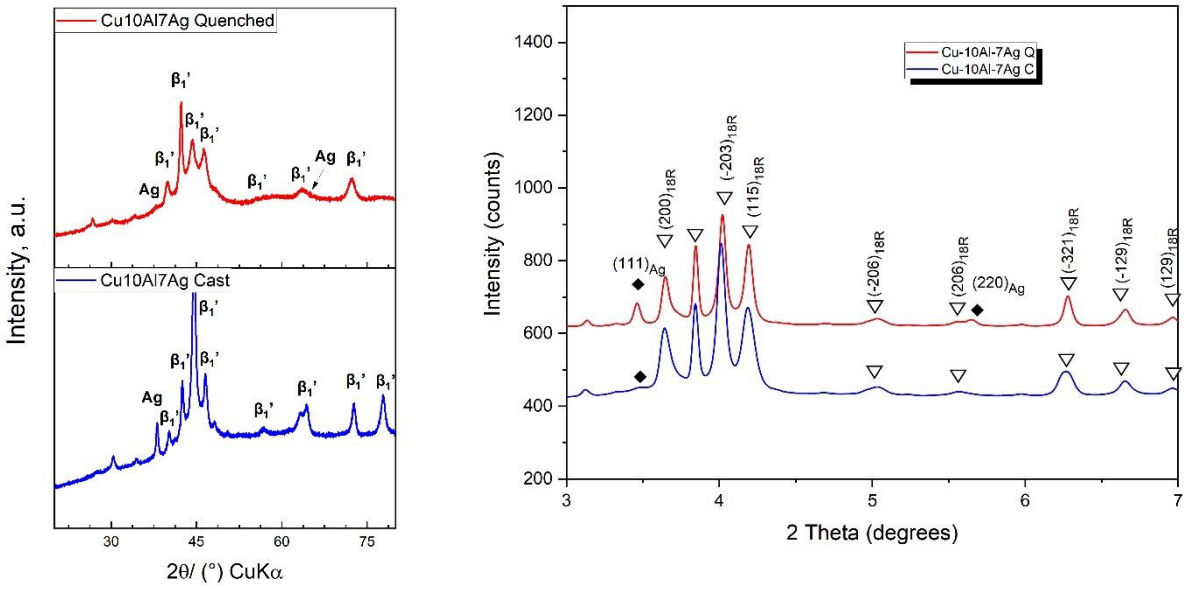

a) b)

Figure 100. *XRD diffractogram of Cu-10Al-7Ag SMA alloy: a) regular XRD diffractogram, b) high-energy X-ray diffraction measurements from synchrotron*

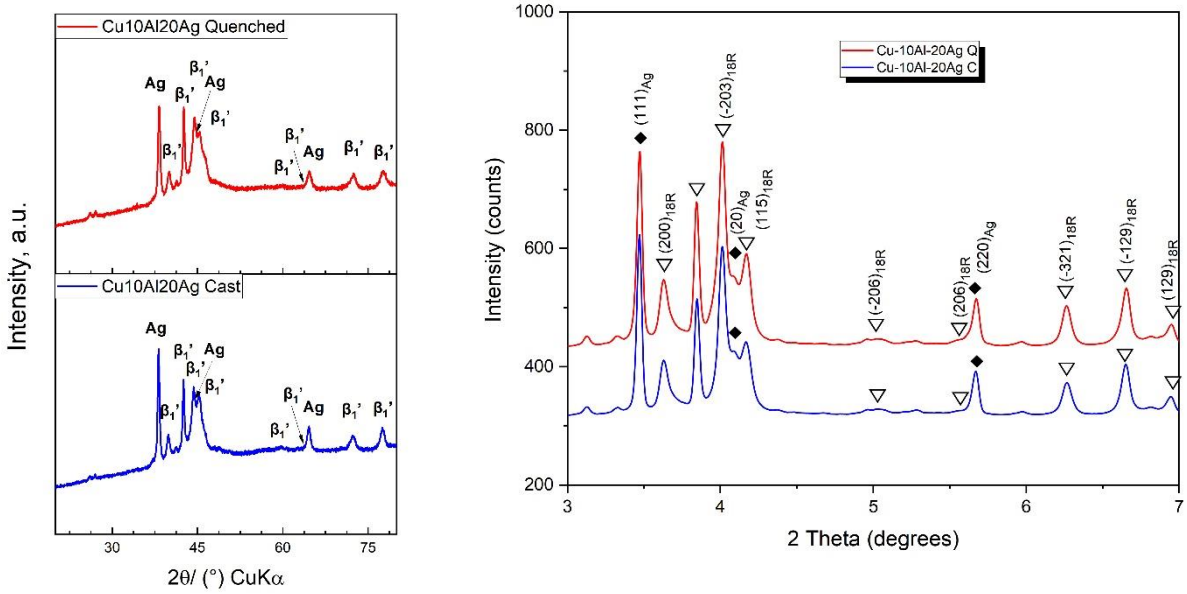

a) b)

Figure 101. *XRD diffractogram of Cu-10Al-20Ag SMA alloy: a) regular XRD diffractogram, b) high-energy X-ray diffraction measurements from synchrotron*

4.2.3. Transmission electron microscopy (TEM)

The sample Cu-10Al-7Ag SMA, with completely formed martensite structure in as-cast and quenched state was chosen for TEM analysis, (Fig. 102-105.). It is confirmed β_1'(18R) structure both quenched (Fig. 102.) and as-cast (Fig. 104.) state.

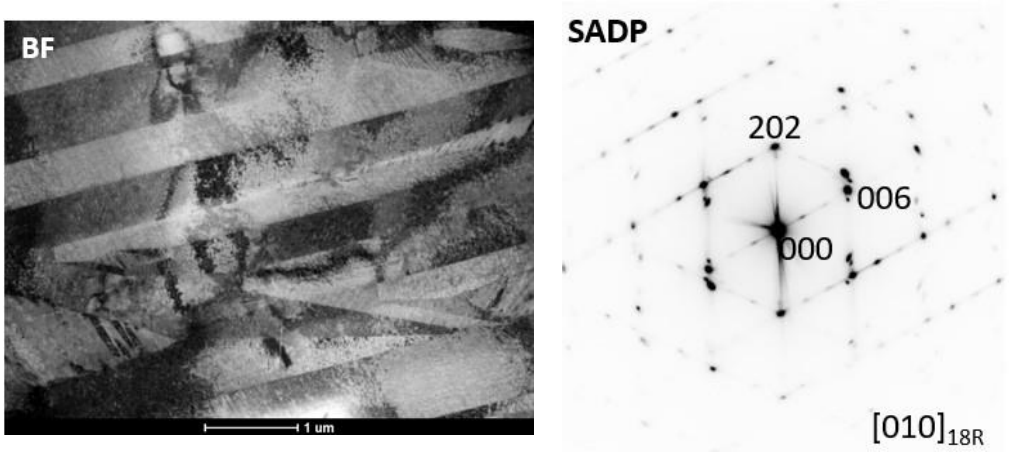

a) b)

Figure 102. *Microstructure of the quenched Cu10Al7Ag sample observed through a Transmission Electron Microscope (TEM): a) bright-field TEM image, b) Selected Area Diffraction Pattern (SADP).*

In addition, Figure 103. as well as Figure 105. shows the observed corresponding orientation of the selected electron diffraction patterns (SADP) of the [010] zone axis. The listed planes are parallel to the zone axis and are represented by points perpendicular to the crystallographic planes. This indicates that the SADP shows two martensitic variants of β_1' (18R) martensite visible in the darkfield images.

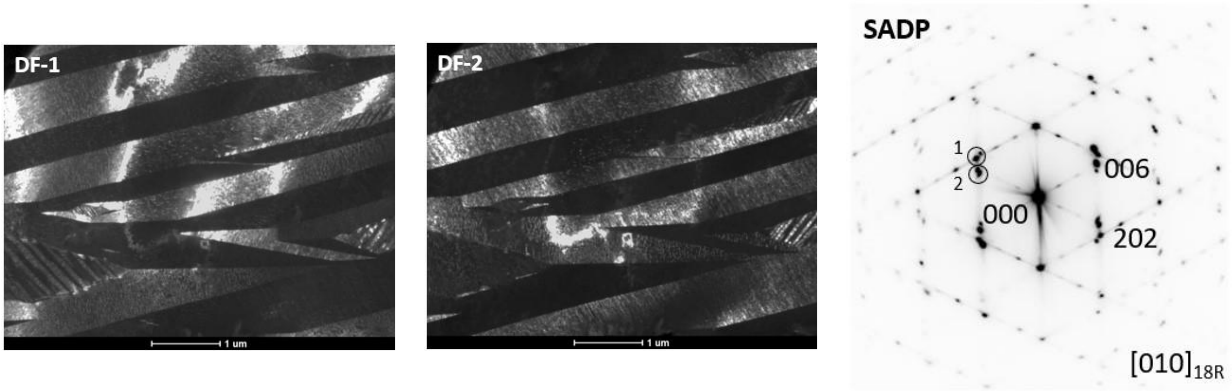

a) b) c)

Figure 103. *Microstructure of the quenched Cu10Al7Ag sample observed through a Transmission Electron Microscope (TEM): a) dark-field TEM image captured from reflections 1, b) dark-field TEM image captured from reflections 2, c) Selected Area Diffraction Pattern (SADP) of corresponded area.*

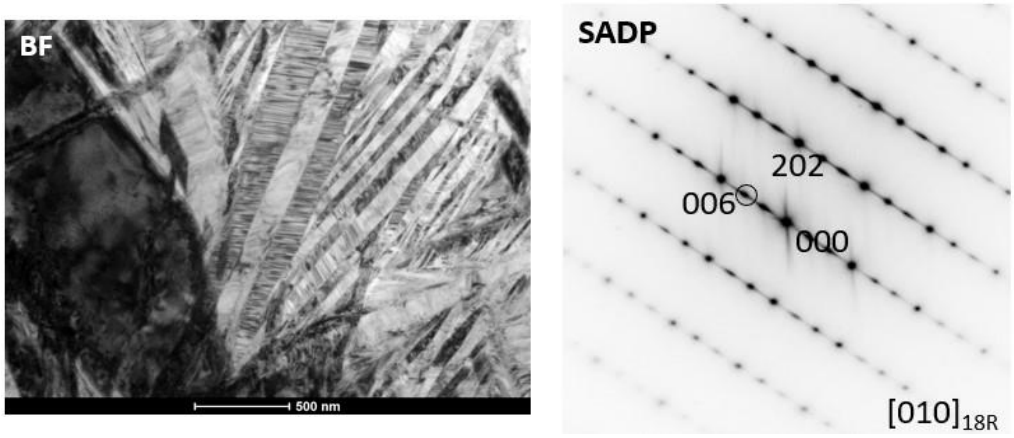

a) b)

Figure 104. *Microstructure of the as-cast Cu10Al7Ag sample observed through a Transmission Electron Microscope (TEM): a) bright-field TEM image, b) Selected Area Diffraction Pattern (SADP).*

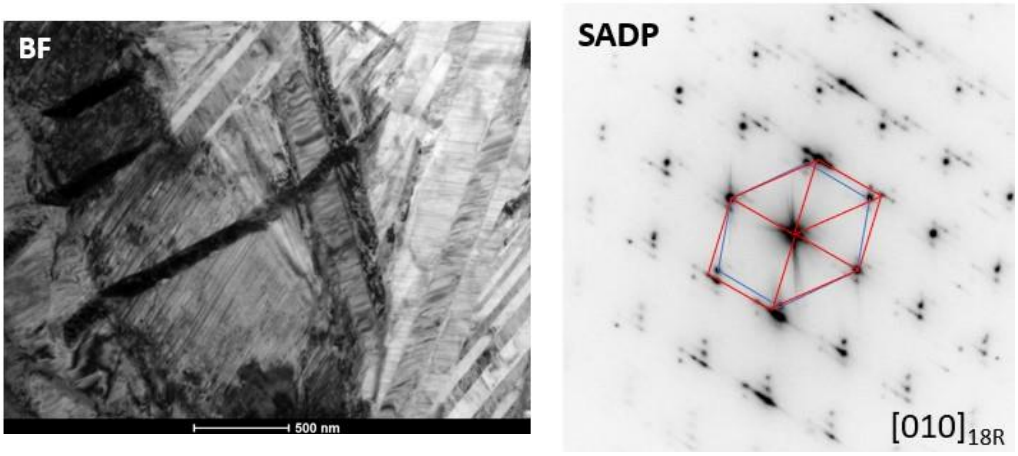

a) b)

Figure 105. *Microstructure of the as-cast Cu10Al7Ag sample observed through a Transmission Electron Microscope (TEM): a) bright-field TEM image, b) Selected Area Diffraction Pattern (SADP).*

4.2.4. Thermal analysis (DSC)

The DSC thermogram for as-cast Cu-10Al-1Ag alloy shows martensite transformation in cooling curves with start and finish temperatures of martensite transformation, M_s = 183 °C and M_f = 154 °C (1st cooling cycle) and 151 °C (2nd cooling cycle). Martensitic transformation temperatures didn`t change significantly in the first and second cycle (Tab. 6.). In relation to as-cast alloy start martensite temperature is similar, but transformation releases higher heat fusion, and finish transformation temperature is shifted to lower value. DSC results indicate that the formed β_1'-martensite is thermally stable, which is very important for the application of SMA.

With higher content of silver M_s mostly increases, beside Cu-10Al-1Ag alloy. Quenched alloys mostly have lower M_f in relations to as-cast alloys.

In the second cooling cycle, the DSC results in Table 6. for various Cu-Al-Ag SMA alloys are presented. The Cu-10Al-2Ag alloy indicates martensite transformation start and finish temperatures of M_s = 172 °C and M_f = 157 °C in as-cast state, while after quenching temperatures of M_s = 204 °C and M_f = 144 °C. The as-cast Cu-10Al-5Ag alloy records start and finish transformations temperatures of M_s = 181 °C and M_f = 147 °C, and after quenching, M_s = 183 °C and M_f = 145 °C. The Cu-10Al-7Ag alloy displays in as-cast state M_s = 169 °C and M_f = 86 °C, with after quenching values of M_s = 175 °C and M_f = 95 °C. Lastly, the as-cast

Cu-10Al-20Ag alloy shows start and finish transformations M_s = 196 °C and M_f = 167 °C, with a shift to M_s = 172 °C and M_f = 119 °C after quenching (Fig. 106.). Across all these alloys, the formed β_1'-martensite demonstrates thermal stability, crucial for the application of SMA.

Table 6. *DSC results of martensitic transformation temperatures and fusion enthalpy*

No.:	Sample:	M_s/°C (1st cycle)	M_f/°C (1st cycle)	M_s/°C (2nd cycle)	M_f /°C (2nd cycle)	ΔH (J/g) (2nd cycle)
1	as-cast Cu-10Al-1Ag	183	154	183	151	0,05
2	quenched Cu-10Al-1Ag	183	129	180	133	0,09
3	as-cast Cu-10Al-2Ag	173	160	172	157	0,001
4	quenched Cu-10Al-2Ag	211	143	204	144	0,08
5	as-cast Cu-10Al-5Ag	173	150	181	147	0,015
6	quenched Cu-10Al-5Ag	180	145	183	145	0,03
7	as-cast Cu-10Al-7Ag	178	95	169	86	0,06
8	quenched Cu-10Al-7Ag	176	99	175	95	0,07
9	as-cast Cu-10Al-20Ag	208	141	196	167	0,52
10	quenched Cu-10Al-20Ag	167	126	172	119	1,37

While OM and SEM find it difficult to detect and observe thin and small β_1'-martensite plates in the Cu-10Al-20Ag SMA alloys in both states, the DSC results in Figure 106. clearly show martensite transformation and confirm its existence as shown in XRD (Fig. 101.).

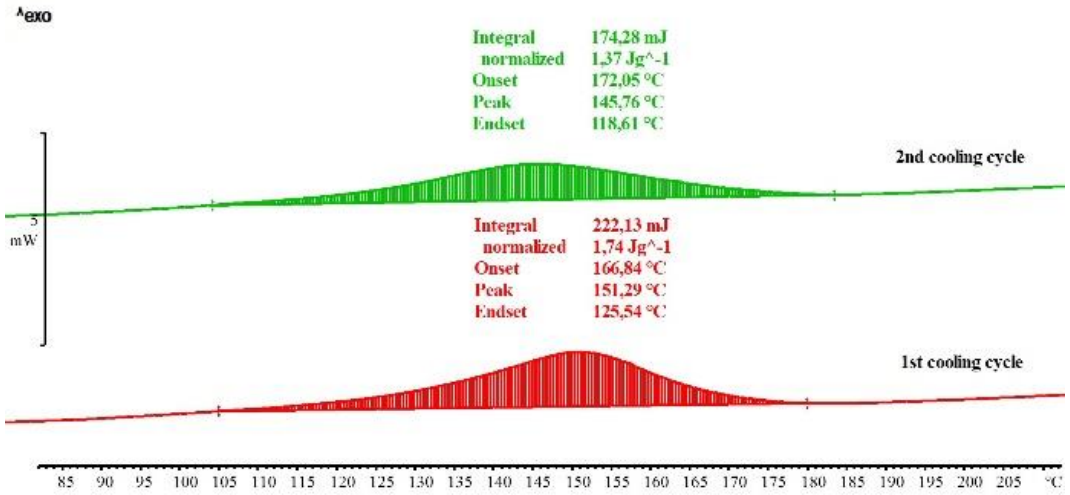

Figure 106. *DSC cooling curves of quenched Cu-10Al-20Ag alloy*

4.2.5. Microhardness

The microhardness of the studied Cu-Al-Ag SMA alloys is determined and presented in Table 7. Results show typical behavior of SMA alloys, and mostly lower microhardness in martensitic structure, after quenching (Tab. 7.).

In the case of Cu-10Al-20Ag SMA and Cu-10Al-2Ag SMA alloys, the microhardness increases after quenching. This increased hardness is probably due to the high precipitation saturation of the alloy due to the high silver addition in the composition of the alloys. For alloys with a lower silver addition, the deviation is likely due to an inhomogeneous sample.

Table 7. *Microhardness of Cu–Al–Ag SMA alloys*

Cu-Al-Ag system			**Microhardness**					
No.	**Sample**	**State**	**1**	**2**	**3**	**4**	**5**	**Average**
1	Cu-10Al-1Ag	As-cast	314,94	292,65	284,43	295,89	307,84	297,34
2	Cu-10Al-1Ag	Quenched	278,57	284,55	270,88	269,11	280,45	278,00
3	Cu-10Al-2Ag	As-cast	153,13	139,67	175,08	146,15	175,05	153,51
4	Cu-10Al-2Ag	Quenched	213,39	222,63	242,84	232,36	257,92	227,81
5	Cu-10Al-5Ag	As-cast	302,74	297,89	297,56	295,15	295,98	297,86
6	Cu-10Al-5Ag	Quenched	274,87	277,23	262,79	273,36	271,24	271,90
7	Cu-10Al-7Ag	As-cast	225,68	287,79	323,21	278,72	323,34	278,85
8	Cu-10Al-7Ag	Quenched	186,57	250,05	184,20	222,53	181,80	210,84
9	Cu-10Al-20Ag	As-cast	151,35	154,92	164,49	160,59	147,86	157,84
10	Cu-10Al-20Ag	Quenched	196,70	194,09	210,49	191,59	225,77	198,22

5. CONCLUSION

Based on the results, the following conclusions can be drawn:

- Cu-Al-Mn-Ag and Cu-Al-Ag SMA alloys were successfully produced by melting pure metals in an electric arc furnace.
- Thermodynamic modelling was prepared to determine temperature ranges of stable phases for equilibrium conditions.
- Microstructural analysis by OM, SEM, EBSD, XRD and TEM confirmed existence of two type of martensite structure β_1' (18R) and γ_1' (2H) in quenched Cu-9Al-16Mn-2Ag alloy, while in other SMA alloys was detected only one β_1' (18R) martensite structure.
- The addition of silver influences the martensite transformation in SMA alloys in such a way that the martensite length and size decrease the higher the silver addition in the alloys.
- The Cu-9Al-10Mn-XAg alloys in the as-cast and quenched state, where X stands for 2, 5, 7 and 8 % Ag addition, did not exhibit a martensite structure but rather showed an austenite phase, indicating that these alloys have a low transformation temperature M_s.
- The addition of silver tends to increase the M_s temperature and boarder martensitic transformations with lower M_f temperatures in most as-cast Cu SMA alloys. In addition, the addition of manganese tends to shift the M_s temperature to lower values, while quenching increases these temperatures. Heat treatment process of Cu SMA alloys primarily lowers the M_f temperature.
- Cu-Al-Mn-Ag SMA alloys exhibit lower microhardness after quenching, a property typical of Cu based SMA alloys. Exceptionally, the alloy with a manganese addition of 16% wt. shows a unique increase in microhardness after quenching, which is probably due to the formation of the brittle γ_1' phase in its microstructure. In addition, alloys with a lower manganese addition, namely 7% wt. exhibit higher microhardness values than alloys with a manganese addition of 16% wt. Indicating that increasing the manganese addition in the composition of Cu–Al–Mn-Ag SMA alloys tends to decrease the

hardness. For silver additions, the relationship is reversed. As the silver addition increases, the hardness of the alloy increases. Microhardness measurements show a typical behavior for Cu-Al-Ag SMA alloys, which predominantly exhibit reduced microhardness in the martensitic structure after quenching.

- Among the quaternary Cu-Al-Mn-Ag SMA alloys studied, Cu-9Al-16Mn-2Ag, Cu-9Al-7Mn-2Ag, and Cu-9Al-7Mn-5Ag exhibited the best functional properties and favorable martensitic transformation in their microstructures. In ternary Cu-Al-Ag SMA alloys the outstanding functional properties were shown compositions Cu-10Al-5Ag and Cu-10Al-7Ag.

REFERENCE

[1] Kainuma, R. Recent progress in shape memory alloys. Mater. Trans., 59, 3, 2018, 327-331.

[2] Wadood, A., Brief Overview on Nitinol as Biomaterial. Adv. Mat. Sci. and Eng., 9, 2016, 4173138.

[3] Rodriguez, J., et al. Shape-morphing composites with designed micro-architectures. Sci. Rep. 6, 2016.

[4] Dobrzanski, L., et al. Nitinol Type Alloys General Characteristics and Applications in Endodontics. Processes 10, 2022, 101.

[5] Mazzer, E. M., da Silva, M. R., Gargarella, P. Revisiting Cu-based shape memory alloys: Recent developments and new perspectives. J. Mater. Res., 37, 1, 2022, 162-182.

[6] Silva, L.S., Silva, R.A.G. Alloys-by-design: role of atomic properties on the phase equilibria of CuAlMn-based alloys. Mater. Charact., 163, 2020, 110304.

[7] Šimšić, Z.S., et al. Thermal analysis and microstructural investigation of Cu-rich alloys in the Cu–Al–Ag system. J. Alloys Compd., 612, 2014, 486-492.

[8] Silva, R.A.G., et al. Characteristics of the Cu–18.84 at.%Al–10.28 at.%Mn–1.57 at.%Ag alloy after slow cooling from high temperatures. J. Thermal. Anal. Calorim., 121, 2015, 1233.

[9] Motta, M.B.J.L., et al. Kinetics of bainite precipitation in the $Cu_{69.3}$ $Al_{18.8}$ $Mn_{10.3}$ $Ag_{1.6}$ alloy. Mater. Chem. Phys., 188, 2017, 125–130.

[10] Silva, R.A.G., et al. Investigation of thermal, mechanical and magnetic behaviors of the Cu-11%Al alloy with Ag and Mn additions, Mater. Charact., 75, 2013, 194-199.

[11] Xi, X., et al. The ultrahigh functional response of CuAlMnNb shape memory alloy by selective laser melting. J. Mater. Res. Tech., 20, 2022, 671.

[12] Santos, C.M.A., et al. Phase stability in the Cu-9wt%Al-10wt%Mn-3wt%Ag alloy. J. Phys. Chem. Solids., 104, 2017, 145-151.

[13] Pilz, C.B., et al. Microstructure and phase stability of CuAlMnAgZr multicomponent alloys. Mater. Chem. Phys., 241, 2020, 122343.

[14] Zhu, J.J., Liew, K.M. Description of Deformation in Shape Memory Alloys from DO_3 Austenite to 18R Martensite by Group Theory. Acta Mater., 51, 9, 2003, 2443.

[15] Velázquez, D., et al. Spinodal Decomposition, Chemical and Magnetic Ordering in Cu–Al–Mn Shape Memory Alloys. Mater. Chem. Phys., 246, 2020, 122793.

[16] Suru, M.G., et al. Precipitation Effects on the Martensitic Transformation in a Cu-Al-Ni Shape Memory Alloy. J. Mater. Eng. Perform., 25, 4, 2016, 1562.

[17] Qian, S., et al. Elastocaloric effect in CuAlZn and CuAlMn shape memory alloys under compression. Philos. Trans. Royal Soc. A, 374, 2074, 2016, 20150309.

[18] Zaeem, M.A., et al. A Review of Computational Modeling Techniques in Study and Design of Shape Memory Ceramics. Comput. Mater. Sci., 160, 2019, 120–136.

[19] Lagoudas, D.C. Shape Memory Alloys - Modeling and Engineering Applications. Springer, New York, 2008.

[20] Olson, G.B., Cohen, M. Kinetics of strain-induced martensitic nucleation. Scr. Metall. 9, 1975, 1247–1254.

[21] Salzbrenner, R.J., Cohen, M. On the thermodynamics of thermoelastic martensitic transformations. Acta Metall. 27, 1979, 739–748.

[22] Jani, J.M., Leary, M., Subic, A., Gibson, M.A. A review of shape memory alloy research, applications and opportunities. Mater. Des., 56, 2014, 1078–1113.

[23] Otsuka, K., Wayman, C.M. Shape Memory Materials. Cambridge University Press, Cambridge, 1998.

[24] Kato, H., Yasuda, Y., Sasaki, K. Thermodynamic assessment of the stabilization effect in deformed shape memory alloy martensite. Acta Mater. 59, 2011, 3955–3964.

[25] Sun, L., et al. Stimulus-Responsive Shape Memory Materials: A Review. Mater. Des., 33, 2012, 577–640.

[26] Vajpai, S.K., Dube, R.K., Sangal, S. Microstructure and properties of Cu–Al–Ni shape memory alloy strips prepared via hot densification rolling of argon atomized powder preforms. Mater. Sci. Eng. A, 529, 2011, 378–387.

[27] Biesiekierski, A., et al. Investigations into Ti–(Nb,Ta)–Fe alloys for biomedical applications. Acta Biomater., 32, 2016, 336-347.

[28] Laureanda, C. One Way and Two Way—Shape Memory Effect: Thermo—Mechanical Characterization of Ni—Ti Wires. Doctoral dissertation, University of Pavia, Italy, 2008.

[29] Alaneme, K. K., Okotete, E. A. Reconciling viability and cost-effective shape memory alloy options–A review of copper and iron-based shape memory metallic systems. Eng. Sci. Technol. an Int. J. ENG. SCI. TECHNOL., 19, 3, 2016, 1582-1592.

[30] Huang, W.M., et al. Shape Memory Materials. Mater. Today, 13, 7-8, 2010, 54–61.

[31] Hornbogen, E. Comparison of Shape Memory Metals and Polymers. Adv. Eng. Mater., 8, 1-2, 2006, 101–106.

[32] Sun, L., et al. The Temperature Memory Effect and the Influence of Thermo-Mechanical Cycling in Shape Memory Alloys. Smart Materials and Structures, 19, 5, 2010, 055005.

[33] Fan, K., et al. Water-Responsive Shape Memory Hybrid: Design Concept and Demonstration. Express Polym. Lett., 5, 5, 2011, 409–416.

[34] Hartwell, A. Shape Memory Alloys for Small Scale Actuation. Thesis, Massachusetts Institute of Technology, Department of Mechanical Engineering, 2018.

[35] Lexcellent, C. Shape-memory Alloys Handbook. John Wiley & Sons, New York, 2013.

[36] Ivanić, I. The effect of heat treatment on microstructure and properties of CuAlNi shape memory alloy. Doctoral thesis, University of Zagreb, Faculty of Metallurgy, 2017.

[37] Mehrabi, K. Characterization and Optimization of the Two-Way Effect in Melt-spun NiTi-based Shape Memory Alloys. Doctoral thesis, Montanuniversität, Leoben, 2011.

[38] Ölander, A. An electrochemical investigation of solid cadmium-gold alloys. J. Am. Chem. Soc., 54.10, 1932, 3819-3833.

[39] Greninger, A.B., Mooradian V.G. Strain transformation in metastable beta copper-zinc and beta copper-Ti alloys. Trans. Aime., 128, 1938, 337-369.

[40] Kurdjumov, G.V., Khandros L.G. First reports of the thermoelastic behavior of the martensitic phase of Au-Cd alloys. Doklady Akademii Nauk SSSR, 66.2, 1949, 211-213.

[41] Chang, L.C., Read, T. A. Plastic deformation and diffusionless phase changes in metals-The gold-cadmium beta phase. JOM, 3.1, 1951, 47-52.

[42] Wayman, C.M., Harrison J.D. The origins of the shape memory effect. JOM, 41.9, 1989, 26-28.

[43] Schetky L.M. Shape Memory Alloys. Sci. Am., 241, 5, 1979, 74-82.

[44] Srinivasan, A.V., McFarland D.M. Smart structures, analysis and design. Cambridge University Press, 2001, 1212-1212.

[45] Castleman, L.S., et al. Biocompatibility of nitinol alloy as an implant material. J. Biomed. Mater. Res., 10.5, 1976, 695-731.

[46] Cutright, D.E., et al. Tissue reaction to nitinol wire alloy. Oral. Surg. Oral. Med. Oral. Pathol., 35, 1973, 578-584.

[47] Abavisani, I., et al. Multifunctional Properties of Shape Memory Materials in Civil Engineering Applications: A State-of-the-Art Review. J. Build. Eng., 44, 2021, 102657.

[48] Shahinpoor, M. Fundamentals of Smart Materials. 1st ed. Royal Society of Chemistry, 2020.

[49] Minorowicz, B., Milecki, A. Design and Control of Magnetic Shape Memory Alloy Actuators. Materials, 15, 2022, 4400.

[50] Wayman C.M., Duerig T.W. Engineering Aspects of Shape Memory Alloys. Butterworth-Heinemann ,3-20, 1990.

[51] Ren, X., Otsuka, K. Origin of Rubber-Like Behavior in Metal Alloys. Nature, 6651, 1997, 579.

[52] Chen, L. Crystallography and morphology of martensite in a Cu-11.8 wt% A1-4.0 wt% Ni-4.0 wt% Mn shape memory alloy. Thesis, University of Wollongong, 1991.

[53] Kainuma, R., et al. Phase equilibria and Heusler phase stability in the Cu-rich portion of the Cu–Al–Mn system, J. Alloys Compd., 266(1-2), 1998, 191-200.

[54] Sutou, Y., et al. Ductile Cu–Al–Mn based shape memory alloys: general properties and applications. Mater. Sci. Technol., 24(8), 2008, 896-901.

[55] Al-Humairi, S.N.S. Cu-Based Shape Memory Alloys: Modified Structures and Their Related Properties. Intech, 13, 2019.

[56] Krishna, T.V., Rao, D.S. Effect of aluminum on microstructure and shape memory effect in Cu-Al-Ag-Mn shape memory alloys. Aust. J. Mech. Eng., 1, 2022, 17.

[57] Dasgupta, R. A Look into Cu-based Shape Memory Alloys: Present Scenario and Future Prospects. J. Mater. Res. 29, 16, 2014, 1681–1698.

[58] Tatar, C., Acar, R., Qader, I. N. Investigation of Thermodynamic and Microstructural Characteristics of NiTiCu Shape Memory Alloys Produced by arc-melting Method. Eur. Phys. J. Plus, 135, 3, 2020, 1–11.

[59] Porter, D.A., Easterling, K.E. Diffusionless Transformations, Phase Transformations in Metals and Alloys, Fourth Edition, Oxon: CRC Press, 2022.

[60] Funakubo, H., Kennedy, J.B. Shape memory alloys. Gordon and Breach, New York, 1987.

[61] Nishiyama, Z., et al. Martensitic transformation. Academic Press, New York, 1978.

[62] Christian JW. Deformation by moving interfaces. Metall. Trans. A, 13, 4, 1982, 509–38.

[63] Huang, W.M., Zhang, W.H., Gao, X.Y. Micro mirror based on surface relief phenomenon in shape memory alloys. Materials, devices, and systems for display and lighting, Shanghai, China. SPIE 14–18, 2002, 155–61.

[64] Miyazaki, S., Fu, Y.Q., Huang, W.M. Thin film shape memory alloys: fundamentals and device applications. Cambridge University Press, Cambridge (U.K.), New York, 2009.

[65] Fu, Y.Q., et al. TiNi-based thin films in MEMS applications: a review. Sens. Actuator A Phys. 112, 2–3, 2004, 395–408.

[66] Wu, M.J., et al. Reversible surface morphology in shape-memory alloy thin films. J. Appl. Phys., 105, 3, 2009, 033517.

[67] Huang, W.M., Hu, Y.Y., An, L. A simple approach to determine five thermomechanical properties of thin ductile films on an elastic substrate. Appl. Phys. Lett., 85, 25, 2004, 6173–5.

[68] Huang, W.M., Hu, Y.Y., An, L. Determination of stress versus strain relationship and other thermomechanical properties of thin films. Appl. Phys. Lett., 87, 20, 2005, 201904.

[69] Gao, X.Y., Huang, W.M. Thermomechanical behavior of shape memory alloys under non-proportional load. Proceedings of SPIE on transducing materials and devices, 2002, 183–91.

[70] Sun, L., Huang, W.M. Nature of the multistage transformation in shape memory alloys upon heating. Met. Sci. Heat. Treat., 51, 11–12, 2009, 573–8.

[71] Shield, T.W. Orientation dependence of the pseudoelastic behavior of singlecrystals of Cu–Al–Ni in tension. J. Mech. Phys. Solids, 43, 6, 1995, 869–95.

[72] Ng, S.B., Huang, W.M., Shu, D.W. Plastic energy and tearing energy of a NiTi shape memory alloy wire. Mater. Des., 29, 5, 2008, 1066–9.

[73] Huang, X., Ackland, G.J., Rabe, K.M. Crystal structures and shape-memory behavior of NiTi. Nat. Mater., 2, 5, 2003, 307-11.

[74] Mizar, S.P. Thermomechanical characterization of NiTiNOL and NiTiNOL based structures using ACES methodology. Doctoral thesis, Worcester Polytechnic Institute, Waltham, MA, 2005.

[75] Cohen M., Machlin, E.S., Paranjpe, V.G. Thermodynamics in Physical Metallurgy, American Society for Metals, 242, 1949.

[76] Saadat, S., et al. An overview of vibration and seismic applications of NiTi shape memory alloy. Smart Mater. Struc., 11, 2002, 218-229.

[77] Yu, Y.L., Nakano, M., Ikeda, T. Directed bending of a polymer film by light – miniaturizing a simple photomechanical system could expand its range of applications. Nature, 425, 6954, 2003, 145.

[78] Naciri, J., et al. Inventors; Nematic elastomer fiber with mechanical properties of a muscle. United States patent, US, 7794834, 2010.

[79] Huang, W.M., et al. Shape memory materials. Mater. Today, 13, 7–8, 2010, 54–61.

[80] Cladera, A., et al. Iron based shape memory alloys for civil engineering structures: an overview. Constr. Build. Mater., 63, 2014, 281–293.

[81] Davis, J. R. Materials: ASM Specialty Handbook. ASM International, Ohio, 1998.

[82] Shaw, J.A. A thermomechanical model for a 1-D shape memory alloy wire with propagating instabilities. Int. J. Solids Struct., 39, 5, 2002, 1275-1305.

[83] Sehitoglu, H., et al. Compressive response of NiTi single crystals. Acta Mater., 48, 13, 2000, 3311-3326.

[84] Turner T.L. Thermomechanical Response of Shape Memory Alloy Hybrid Composites. Doctoral thesis, Virginia Polytechnic Institute and State University, Hampton, Virginia, 2001.

[85] Lexcellent, C., et al. The two-way shape memory effect of shape memory alloys: an experimental study and a phenomenological model. Int. J. Plast., 16, 10-11, 2000, 1155-1168.

[86] Meng, X.L., et al. Two-Way Shape Memory Effect Induced by Martensite Deformation and Stabilization of Martensite in TI36NI49HF15 High Temperature Shape Memory Alloy. Mater. Lett., 57, 26-27, 2003, 4206–4211.

[87] Wang, Z.G., et al. Effect of thermomechanical training temperature on the two-way shape memory effect of TiNi and TiNiCu shape memory alloys springs. Mater. Lett., 57, 9-10, 2003, 1501-1507.

[88] Guerioune, M., et al. SHS of shape memory CuZnAl alloys, Int. J. Self Propag. High Temp. Synth., 17, 1, 2008, 41–48.

[89] Biesiekierski A., et al. A new look at biomedical Ti-based shape memory alloys. Acta Biomater., 8, 2012, 1661–1669.

[90] Vajpai, S.K., Dube, R.K., Sangal, S. Application of rapid solidification powder metallurgy processing to prepare Cu–Al–Ni high temperature shape memory alloy strips with high strength and high ductility. Mater. Sci. Eng. A, 570, 2013, 32–42.

[91] Lelatko, J., Morawiec, H. The modeling of the deformation behavior of Cu–Al–Nb–X shape memory alloys containing primary particles. Mater. Sci. Eng. A, 481–482, 2008, 684–687.

[92] Ueland, S.M., Schuh, C.A. Transition from many domains to single domain martensite morphology in small-scale shape memory alloys. Acta Mater., 61, 2013, 5618–5625.

[93] Gotthardt, R., Scherrer, P., Stalmans, R. Smart materials based on shape memory alloys: examples from Europe. Mater. Sci. Forum, 327, 2000, 83-90.

[94] Gil, F.J., Planell, J.A. Effect of copper addition on the superelastic behavior of Ni-Ti shape memory alloys for orthodontic applications. J. Biomed. Mater. Res., 48, 1999, 682-688.

[95] Segui, C., Cesari, E., Van Humbeeck, J. Irreversibility in Two-Stage Martensitic Transformations of Cu–Al–Ni and Cu–Zn–Al–Mn Alloys. J. Mater. Trans. JIM, 31, 1990, 375.

[96] Husain, S.W., Clapp, P.C. Intermediate temperature embrittlement of copper alloys. J. Mater. Sci., 22, 1987, 2351.

[97] Sakamoto, H., Shimizu, K., Analytical investigation on cyclic deformation and fatigue behavior of polycrystalline Cu–Al–Ni shape memory alloys above Ms. Trans. Jpn. Inst. Metals., 27, 1986, 601.

[98] Mazzer, E.M., et al. On the valence electron theory to estimate the transformation temperatures of Cu–Al-based shape memory alloys. J. Mater. Res., 32, 2017, 3165–3174.

[99] Hussain, S., et al. R. Effects of Different Quaternary Additions in the Properties of a Cu-Al-Mn Shape Memory Alloy. Mater. Perform. Charact. 4, 1, 2015.

[100] Sutou, Y., et al. Grain size dependence of pseudoelasticity in polycrystalline Cu–Al–Mn-based shape memory sheets. Acta Mater., 61, 10, 2013, 3842–3850.

[101] Ma, J., Karaman, I., Noebe, R.D. High temperature shape memory alloys. Int. Mater. Rev., 55, 2013, 257–315.

[102] López-Ferreño, I., et al. High-temperature shape memory alloys based on the Cu-Al-Ni system: design and thermomechanical characterization. J. Mater. Res. Technol., 9, 2020, 9972–9984.

[103] Zhao, X.P., et al. Accelerating the development of multi-component Cu-Al-based shape memory alloys with high elastocaloric property by machine learning. Comput. Mater. Sci., 176, 2020, 109521.

[104] Tan, J., et al. Thermodynamic cycle analysis of heat driven elastocaloric cooling system. Energy, 197, 2020, 117261.

[105] Imran, M., Zhang, X. Recent developments on the cyclic stability in elastocaloric materials. Mater. Des., 195, 2020, 109030.

[106] Kainuma, R., Takahashi, S., Ishida, K. Thermoelastic martensite and shape memory effect in ductile Cu–Al–Mn alloys. Metall. Mater. Trans. A: Phys., 27, 1996, 2187.

[107] Oliveira, J.P., et al. Laser welded superelastic Cu–Al–Mn shape memory alloy wires. Mater. Des., 90, 2016, 122-128.

[108] Araki, Y., et al. Potential of superelastic Cu–Al–Mn alloy bars for seismic applications. Earthq. Eng. Struct. Dyn., 40, 1, 2010, 107–115.

[109] Dolce, M., Cardone, D., Mechanical behavior of shape memory alloys for seismic applications 2. Austenite NiTi wires subjected to tension. Int. J. Mech. Sci., 43, 2001, 2657–2677.

[110] Canbay, C.A., Ozgen, S., Genc, Z.K. Thermal and microstructural investigation of Cu–Al–Mn–Mg shape memory alloys. Appl. Phys. A, 117, 2014, 767–771.

[111] Kise, S., et al. Orientation dependence of plasticity and fracture in single-crystal superelastic Cu-Al-Mn SMA bars. J. Mater. Civ. Eng., 33, 4, 2021, 04021027.

[112] Sutou, Y., et al. Enhancement of superelasticity in Cu-Al-Mn-Ni shape-memory alloys by texture control, Metall. Mater. Trans. A, 33, 9, 2002, 2817–2824.

[113] Sutou, Y., et al. Effect of grain size and texture on pseudoelasticity of Cu-Al-Mn-based shape memory wire. Acta Mater., 53, 15, 2005, 4121–4133.

[114] Kusama, T., et al. Ultra-large single crystals by abnormal grain growth. Nat. Commun., 8, 1, 2017, 354.

[115] Omori, T., et al. Abnormal grain growth induced by cyclic heat treatment. Science., 27, 341, 6153, 2013, 1500-2.

[116] Omori, T., et al. Two-way shape memory effect induced by bending deformation in ductile Cu-Al-Mn alloys. Mater. Trans., 43, 2002, 1676–1683.

[117] Liu, J.L., Huang, H.Y., Xie, J.X. Superelastic anisotropy characteristics of columnar-grained Cu-Al-Mn shape memory alloys and its potential applications. Mater. Des., 85, 2015, 211–220.

[118] Liu, J.L., Huang, H.Y., Xie, J.X., The roles of grain orientation and grain boundary characteristics in the enhanced superelasticity of Cu71.8Al17.8Mn10.4 shape memory alloys. Mater. Des., 64, 2014, 427–433.

[119] Yao, P.S., et al. Two-way shape memory effect induced by tensile deformation in columnar-grained $Cu_{71.7}$ $Al_{18.1}$ $Mn_{10.2}$ alloy. Materials, 11, 11, 2018, 2109.

[120] Yang, S., et al. Microstructure characterization, stress–strain behavior, superelasticity and shape memory effect of Cu–Al–Mn–Cr shape memory alloys. J. Mater. Sci., 52, 2017, 5917–5927.

[121] Sutou Y, et al. Effect of grain refinement on the mechanical and shape memory properties of Cu–Al–Mn base alloys. J. Phys. IV France, 11, 2001, 185 190

[122] Sutou Y, et al. Effects of aging on bainitic and thermally induced martensitic transformation in ductile Cu–Al–Mn-based shape memory alloys. Acta Mater., 57, 2009, 5748–5758.

[123] Obradó, E., et al. Order-disorder transitions of Cu-Al-Mn shape-memory alloys. Phys. Rev. B, 58, 21, 1998, 14245.

[124] Silva, R., et al. Thermal behavior of the Cu–22.55 at.%Al alloy with small Ag additions. J. Therm. Anal. Calorim., 103. 2011, 459-463.

[125] Chen, X., et al. Microstructure, superelasticity and shape memory effect by stress-induced martensite stabilization in Cu–Al–Mn–Ti shape memory alloys. Mater. Sci. Eng.: B, 236, 2018, 10-17.

[126] Liu, J.L., et al. Microstructure and superelasticity control by rolling and heat treatment in columnar-grained Cu-Al-Mn shape memory alloy. Mater. Sci. Eng.: A, 696, 2017, 315-322.

[127] Xu, S., et al. Giant elastocaloric effect covering wide temperature range in columnar-grained Cu71.5Al17.5Mn11 shape memory alloy. Appl. Mater., 4, 10, 2016, 439.

[128] Zhao, X.P., et al. Accelerating the development of multi-component Cu-Al-based shape memory alloys with high elastocaloric property by machine learning. Comp. Mater. Sci., 176, 2020, 109521.

[129] Yang, Q., et al. A Novel Constraint Method During Solution Treatment to Suppress Heating Rate-Dependent Martensitic Stabilization in Cu–17.0 Al–10.5 Mn Alloy. Adv. Eng. Mater., 20, 7, 2018, 1701082.

[130] Yang, Q., et al. Suppressing heating rate-dependent martensitic stabilization in ductile Cu-Al-Mn shape memory alloys by Ni addition: An experimental and first-principles study. Mater. Charact., 145, 2018, 381-388.

[131] Leu, S.S., Hu, C.T. Up-quenching effect on the stabilization process of a Cu Zn Al martensite. Mater. Sci. Eng.: A, 117, 1989, 247-254.

[132] Aydogdu A., Aydogdu, Y., Adiguzel, O. The influence of ageing on martensite ordering and stabilization in shape memory Cu-Al-Ni alloys. Mater. Res. Bull., 32, 5, 1997, 507-513.

[133] Ahlers, M., Pelegrina, J.L. Ageing of martensite: Stabilisation and ferroelasticity in Cu-based shape memory alloys. Mater. Sci. Eng.: A., 356, 2003, 298-315.

[134] Otsuka, K., Ren, X. Mechanism of martensite aging effects and new aspects. Mater. Sci. Eng.: A, 312, 2001, 207-218.

[135] Kustov, S., et al. Pinning-induced stabilization of martensite: Part I. Stabilization due to static pinning of interfaces. Acta Mater., 52, 2004, 3075-3081.

[136] Kustov, S., et al. Pinning-induced stabilization of martensite: Part II. Stabilization due to static pinning of interfaces. Acta Mater., 52, 2004, 3083–3096.

[137] Lam, C.W.H., et al. Removal of martensite stabilisation in CANTiM shape memory alloy by post-quench ageing. J. Mater. Process. Tech., 63, 1–3, 1997, 600-603.

[138] Dagdelen, T., et al. Effects of thermal treatments on transformation behaviour in shape memory Cu–Al–Ni alloys. Mater. Lett., 57, 5–6, 2003, 1079-1085.

[139] Yang, Q., et al. Strong heating rate-dependent deterioration of shape memory effect in up/step quenched Cu-based alloys: A ductile CuAlMn alloy as an example. Acta Mater., 111, 2016, 348-356.

[140] Gottstein, G. Physical Foundation of Materials Science. Springer Berlin, Berlin, Germany 3, 2004, 65.

[141] Cao, L.X., Wang, C.Y., Phonon spectrum and related thermodynamic properties of microcrack in bcc-Fe. Chin. Phys., 15, 2006, 2092.

[142] Sueoka, K., Kamiyama, E., Kariyazaki, H. A study on density functional theory of the effect of pressure on the formation and migration enthalpies of intrinsic point defects in growing single crystal Si, J. App. Phys., 111, 2012, 093529.

[143] Vanhellemont, J., Kamiyama, E. Experimental Study of the Impact of Stress on the Point Defect Incorporation during Silicon Growth. ECS Solid State Lett., 3, N5, 2014, X3-X4.

[144] Ishibashi, H., et al. Vacancy migration and long-range ordering due to ageing in AuCd shape memory alloys. Mater. Sci. Eng.: A, 329–331, 2002, 568-572.

[145] Li, M., et al. Effect of aging treatment on damping capacity in Cu–Al–Mn shape memory alloy. J. Alloys Compd., 821, 2020, 153213.

[146] Lu, X., et al. Effect of Ce addition on the microstructure and damping properties of Cu–Al–Mn shape memory alloys, J. Alloys. Compd., 480, 2009, 608-611.

[147] Li, H., Yuan, B., Gao, Y. Achieving high oligocrystalline degree via strut architecture tailoring to increase the damping and mechanical properties of spherical porous CuAlMn SMAs. J. Alloys Compd., 767(2018) 690-702.

[148] Mielczarek, A., Woeckel, Y., Riehemann, W. Effect of cold rolling on the damping of as cast Cu-Al-Mn shape memory alloys. Solid State Phenom., 137, 2008, 155-162.

[149] Oliveira, J.P., et al. Improvement of damping properties in laser processed superelastic Cu-Al-Mn shape memory alloys. Mater. Design., 98, 2016, 280-284.

[150] Koeda, N., et al. Damping properties of ductile Cu-Al-Mn-based shape memory alloys. Mater. Trans., 46, 2005, 118-122.

[151] Sutou, Y., et al. Effects of grain size and texture on damping properties of Cu–Al–Mn-based shape memory alloys. Mat. Sci. Eng. A-Struct., 438-440, 2006, 743-746.

[152] Yang, J., et al. Effects of grain refinement on the structure and properties of a CuAlMn shape memory alloy. Mat. Sci. Eng. A-Struct., 664, 2016, 215-220.

[153] Mallik, U.S., Sampath, V. Effect of composition and ageing on damping characteristics of Cu–Al–Mn shape memory alloys. Mat. Sci. Eng. A-Struct., 478, 2008, 48-55.

[154] Jiao, Y.Q., et al. Effect of solution treatment on damping capacity and shape memory effect of a CuAlMn alloy. J. Alloys Compd., 491, 2010, 627-630.

[155] Wang, Q.Z., et al. Effects of aging on the structure and damping behaviors of a novel porous CuAlMn shape memory alloy fabricated by sintering–dissolution method. Mat. Sci. Eng. A-Struct., 615, 2014, 278-282.

[156] Živković, D., et al. Calculation of thermodynamic properties of Cu–Al–(Ag, Au) shape memory alloy systems. Trans. Indian Inst. Met., 67, 2, 2014, 285-289.

[157] Guilemany, J.M., Fernandez, J., Zhang, X.M. TEM study on the microstructure of Cu–Al–Ag shape memory alloys. Mater. Sci. Eng.: A, 438, 2006, 726-729.

[158] Saud, S.N., et al. Influence of Silver nanoparticles addition on the phase transformation, mechanical properties and corrosion behaviour of Cu–Al–Ni shape memory alloys. J. Alloys Compd., 612, 2014, 471-478.

[159] Guilemany, J.M., et al. A new Cu-based SMA with extremely high martensitic transformation temperatures. J. phys. IV, 5, C2, 1995, C2-361.

[160] Saud, S. N., et al. Microstructure and corrosion behaviour of Cu–Al–Ni shape memory alloys with Ag nanoparticles. Corros. Mater., 66, 6, 2015, 527-534.

[161] Silva, R.A.G., et al. Completeness of β-phase decomposition reaction in Cu–Al–Ag alloys. J. Therm. Anal. Calorim., 109, 2, 2012, 927-931.

[162] Sutou, Y., Kainuma, R., Ishida, K. Effect of alloying elements on the shape memory properties of ductile Cu–Al–Mn alloys. Mat. Sci. Eng. A Struct., 273, 1999, 375–379.

[163] Yang, S., et al. Superelasticity and shape memory effect in Cu–Al–Mn–V shape memory alloys. Mater. Des., 115, 2017, 17-25.

[164] Silva, R.A.G., et al. Effect of Ag addition on phase transitions of the Cu–22.26at.%Al–9.93at.%Mn alloy. Thermochim. Acta, 554, 2013, 71-75.

[165] Canbay, C.A., Gudeloglu, S., Genc, Z.K. Investigation of the Enthalpy/Entropy Variation and Structure of Cu–Al–Mn–Fe Shape Memory Alloys. Int. J. Thermophys., 36, 2015, 783–794.

[166] Sedmak, P. Instability of cyclic superelastic deformation of NiTi investigated by synchrotron X-ray diffraction. Acta Mater., 94, 2015, 257–270.

[167] Santos, C.M.A., et al. Effects of Ag Presence on Phases Separation and order-disorder Transitions in Cu-xAl-Mn Alloys. Mater. Chem. Phys., 227, 2019, 184–190.

[168] Silva, R.A.G., et al. Precipitation hardening in the Cu-11wt.%Al-10wt.%Mn alloy with Ag addition. J. Alloys Compd., 643, 2015, S178–S181.

[169] Silva, R.A.G., et al. Ag-rich precipitates formation in the Cu-11%Al-10%Mn-3%Ag alloy. J. Alloys Compd., 615, 2014, S160–S162.

[170] Salgado, R.S., et al. Non-isothermal kinetics and the effects of alloying elements on bainite precipitation in the Cu74. 5Al15. 0Mn10. 5 alloy. Thermochim. Acta, 711, 2022, 179214.

[171] Manasijević, D., et al. Effect of Mn content on the microstructure and phase transformation temperatures of the Cu-Al-Mn-Ag shape memory alloys. Met. Mater., 58, 4, 2020, 293-299.

[172] Fernández, J., Isalgue, A., Franch, R. Effect of Thermal Cycling on CuAlAg Shape Memory Alloys. Mater. Today: Proc., 2, 2015, S805-S808.

[173] Wang, H., Huang, H., Su, Y. Tuning the operation temperature window of the elastocaloric effect in Cu–Al–Mn shape memory alloys by composition design. J. Alloys Compd., 828, 2020, 154265.

[174] Almdal, K. Shape memory polymers and their composites. Polym. Eng. Sci., 40, 2000, 1754–1767.

[175] Adriany H., Lee B.H., Barlam J.W. Shape memory polymers. Mater. Sci. Eng. R Rep., 69, 2010, 1–51.

[176] Stauber T., Plank L.K., Park K.H., et al. Biodegradable shape memory polymers. Macromol. Biosci., 5, 2005, 505–514.

[177] Zou Z., Li Y., Lu Y. Three-shape memory polymers based on polycaprolactone and poly (vinyl alcohol). J. Mater. Chem., 22, 2012, 10530–10534.

[178] Deng J.D., Fan Z.M., Gu Z.Y. Shape memory polymers and their composites. Prog. Mater. Sci., 57, 2012, 1–119.

[179] Kangning, L., et al. Study on Application of Magnetic Shape Memory Alloys to Vibration Control of Structures. Proceedings of the 7th International Conference on Education, Management, Information and Computer Science (ICEMC 2017), 2017.

[180] Wang, T., et al. Elastic Shape Memory Hybrids Programmable at around Body-Temperature for Comfort Fitting. Polymers, 9, 12, 2017, 674.

[181] Wang, C.C., et al. Rubber-like Shape Memory Polymeric Materials with Repeatable Thermal-Assisted Healing Function. Smart Materials and Structures, 21, 11, 2012, 115010.

[182] Kabir Hasnat M., et al. Characterization of shape memory gels using scanning microscopic light scattering. Nanosensors, Biosensors, and Info-Tech Sensors and Systems 2013, 2013, 8691.

[183] Kabir Hasnat M., et al. The Applications of Shape Memory Gel as a Smart Material. Proceedings of the 12th Asia Pacific Physics Conference (APPC12), 2014.

[184] Sabahi, N., et al. A Review on Additive Manufacturing of Shape-Memory Materials for Biomedical Applications. JOM, 72, 3, 2020, 1229–1253.

[185] Zanaboni, E. One way and two way–shape memory effect: Thermo–mechanical characterization of Ni–Ti wires. Doctoral thesis, University of Pavia, Italy, 2008.

[186] Darjan, C., Dolinsek, J. Shape memory alloys. University of Ljubljana, Faculty of Mathematics and Physics, Department of Physics, 2007.

[187] Duerig, T.W. Applications of shape memory martensitic transformations. B.C. Muddle, Mater. Sci. Forum, 56–58, 1990, 679–692.

[188] Wu, M.H., Schetky, L.M. Industrial applications for shape memory alloys. Proceedings of the International Conference on Shape Memory and Superelastic Technologies, Pacific Grove, California, 2000, 171–182.

[189] Crossley, S., Mathur, N.D., Moya, X. New developments in caloric materials for cooling applications. Aip Adv., 5, 2015, 067153.

[190] Chen, Y., Schuh, C.A. Size effects in shape memory alloy microwires. Acta Mater., 59, 2011, 537–553.

[191] Gómez-Cortés, J.F., et al. Size effect and scaling power-law for superelasticity in shape-memory alloys at the nanoscale. Nature Nano. 12, 2017, 790–796.

[192] Lai, A., et al. Shape memory and superelastic ceramics at small scales. Science 341, 2013, 1505–1508.

[193] Sarkar, S., Ren, X., Otsuka, K. Evidence for Strain Glass in the Ferroelastic-Martensitic System $Ti_{50-x}Ni_{50+X}$. Phys. Rev. Lett., 95, 2005, 205702.

[194] Inamura, T., et al. Self-accommodation of B19′ martensite in Ti–Ni shape memory alloys. Part III. Analysis of habit plane variant clusters by the geometrically nonlinear theory. Philos. Mag., 92, 2012, 2247–2263.

[195] Xiao, F., Fukuda, T., Kakeshita, T. On the physical nature of high reversible strain in Fe–Pd single crystals exhibiting lattice softening. Acta Mater., 61, 2013, 4044–4052.

[196] Sawaguchi, T., et al. Design concept and applications of Fe–Mn–Si-based alloys from shape-memory to seismic response control. Mater. Trans., 57, 2016, 283–293.

[197] Mañosa, L., Planes, A.M. Advanced materials for solid-state refrigeration. Acet, J. Mater. Chem. A, 1, 2013, 4925.

[198] Schmidt, M., Schütze, A., Seelecke, S. Elastocaloric cooling processes: The influence of material strain and strain rate on efficiency and temperature span. Apl Mater., 4, 2016, 064107.

[199] Frenzel, J., et al. High-performance elastocaloric materials for the engineering of bulk- and micro-cooling devices. MRS Bull., 43, 2018, 280–284.

[200] Ossmer, H., Kohl, M. Elastocaloric cooling: Stretch to actively cool. Nat. Energy, 1, 10, 2016, 1–2.

[201] Tušek, J., et al. The elastocaloric effect: a way to cool efficiently. Adv. Energy Mater., 5, 2015, 1500361.

[202] Moya, X., Kar-Narayan, S., Mathur, N.D. Caloric materials near ferroic phase transitions. Nat. Mater., 13, 2014, 439–450.

[203] Engelbrecht, K. Future prospects for elastocaloric devices. J. Phys., 1, 2019, 021001.

[204] Qian, S., et al. A heat driven elastocaloric cooling system. Energy, 182, 2019, 881–899.

[205] Cong, D., et al. Colossal elastocaloric effect in ferroelastic Ni-Mn-Ti alloys. Phys. Rev. Lett., 122, 2019, 255703.

[206] Qian, S., et al. Numerical modeling of an active elastocaloric regenerator refrigerator with phase transformation kinetics and the matching principle for materials selection. Energy, 141, 2017, 744–756.

[207] Wu, Y., Ertekin, E., Sehitoglu, H. Elastocaloric cooling capacity of shape memory alloys–Role of deformation temperatures, mechanical cycling, stress hysteresis and inhomogeneity of transformation. Acta Mater., 135, 2017, 158–176.

[208] Sehitoglu, H., Wu, Y., Ertekin, E. Elastocaloric effects in the extreme. Scr. Mater., 148, 2018, 122–126.

[209] Bonnot, E., et al. Elastocaloric effect associated with the martensitic transition in shape-memory alloys. Phys. Rev. Lett., 100, 2008, 125901.

[210] Tušek, J., et al. Understanding the Thermodynamic Properties of the Elastocaloric Effect Through Experimentation and Modelling. Shape. Mem. Superelasticity, 2, 2016, 317–329.

[211] Ziółkowski, A. Family of thermodynamic RL models of pseudoelasticity, Pseudoelasticity of Shape Memory Alloys. Butterworth-Heinemann, 2015, 55-93.

[212] Kattner, U.R. The thermodynamic modeling of multicomponent phase equilibria. JOM, 49, 1997, 14-19.

[213] Miettinen, J. Thermodynamic description of the Cu-Al-Mn system in the copper-rich corner. Calphad, 27, 1, 2003, 103-114.

[214] Sarı, U., Aksoy, I. Electron microscopy study of 2H and 18R martensites in Cu–11.92 wt%Al–3.78 wt% Ni shape memory alloy. J. Alloys Compd., 417, 2006, 138.

[215] Jain, A.K., et al. Effect of Varying Al/Mn Ratio on Phase Transformation in Cu–Al–Mn Shape Memory Alloys. Trans. Indian Inst. Met., 69, 2016, 1289–1295.

[216] Liverić, L., Holjevac Grgurić, T., Mandić, V., Chulist, R. Influence of Manganese Content on Martensitic Transformation of Cu-Al-Mn-Ag Alloy. Materials, 16, 17, 2023, 5782.

LIST OF FIGURES

LIST OF TABLES

LIST OF ABBREVIATIONS

List of abbreviations and symbols:

SMA - shape memory alloy

OM - optical microscope

SEM - scanning electron microscope

EDS - energy dispersive X-ray spectroscopy

DSC - differential scanning calorimetry

XRD - X-ray diffraction

SADP - selected electron diffraction patterns

M_s - temperature at which the transformation of martensite begins (starts)

M_f - temperature at which the transformation of martensite is completed (finished)

A_s - temperature at which the transformation of austenite begins (starts)

A_f - temperature at which the transformation of austenite is completed (finished)

BF - bright field

POL - polarized light

BIOGRAPHY

Lovro Liverić, born on 3 September 1990 in Rijeka, Croatia, began his academic journey at the University of Rijeka, Faculty of Engineering, in 2009, graduating with a Bachelor of Science (B.Sc.) degree in Mechanical Engineering in 2013. He then pursued postgraduate studies in mechanical engineering at the same institution, graduating with a Master of Science (M.Sc.) in 2016.

After graduation, he participated in a state training program and took a job as a measurement engineer at Gradska plinara Zagreb d.o.o. in 2017, he moved to P.P.C. BUZET d.o.o.-CIMOS d.o.o. as a casting engineer. At the end of the same year, he joined the Faculty of Engineering to pursue a university doctorate in mechanical engineering and started working as a teaching assistant at the Department of Materials Engineering at the University of Rijeka, Faculty of Engineering. As a teaching assistant and junior scientist, he played an active role in the field of materials science. His areas of interest include heat treatment, metallography, crystallography, thermal analysis, and both optical and electron microscopy.

LIST OF PUBLICATIONS

Scientific articles in peer-reviewed journals indexed in Current Contents (CC) database:

[1] Liverić, L., Holjevac Grgurić, T., Mandić, V., Chulist, R. Influence of Manganese Content on Martensitic Transformation of Cu-Al-Mn-Ag Alloy. Materials, 16, 17, 2023, 5782.

[2] Liveric, L., Iljkić, D., Jurković, Z., Čatipović, N., Nuckowski, P., Bialas, O. Corrosion behaviour of annealed 42CrMo4 steel. Mater. Tehnol., 57, 2, 2023, 111-117.

[3] Smokvina Hanza, S., Vrsalović, L., Štic, L., Liverić, L. Corrosion investigations of Al-Si casting alloys in 0.6 M NaCl solution. Eng. Rev., 41, 3, 2021, 115-123.

[4] Batelić, J., Špada, V., Liverić, L., Martinez, S. Investigation of pipeline failure in a thermal power plant's process wastewater. Mater. Tehnol., 55, 1, 2021, 135-140.

[5] Smokvina Hanza, S., Štic, L., Liverić, L., Špada, V. Corrosion behaviour of tempered 42CrMo4 steel. Mater. Tehnol., 55, 3, 2021, 427-433.